Title
High Throughput Ab initio Modeling of Charge Transport for Bio-Molecular-Electronics

Author
Bruque, Nicolas A.

Publication Date
2009

UNIVERSITY OF CALIFORNIA
RIVERSIDE

High Throughput *Ab initio* Modeling of Charge Transport for Bio-Molecular-Electronics

A Dissertation submitted in partial satisfaction
of the requirements for the degree of

Doctor of Philosophy

in

Electrical Engineering

by

Nicolas Alexander Bruque

June 2009

Dissertation Committee:
Dr. Roger Lake, Chairperson
Dr. Alexander Balandin
Dr. Alexander Korotkov

The Dissertation of Nicolas Alexander Bruque is approved:

Committee Chairperson

University of California, Riverside

Acknowledgement

I would like to first thank my graduate advisor Professor Roger Lake, Department of Electrical Engineering, UC Riverside for his support, suggestions and guidance during the past six years as his student. Developing the hardware systems and software model to calculate state-of-the-art electron transport using the non-equilibrium Green function formalism has challenged me far beyond the required EE course work. Many thanks to Roger's wife Rebecca and daughters Madison and Lindsay for inviting me to dinner on multiple occasions. I thank my former lab mates Dr. Khairul Alam and Dr. Rajeev Pandey for their collaboration and support during my first years at UCR. I would like to thank M. K. Ashraf for all his work building, optimizing, and analyzing all the structures we studied throughout these projects. Many thanks to Thomas Helander for his efforts developing, optimizing and supporting parallel enhancements of the code. I thank V. Lordi for the support and training I received at Lawrence Livermore National Laboratory as a 2007 summer intern.

To my family: I thank my parents, Enrique and Sandra Bruque and brother Dr. George Bruque for their support throughout graduate school. And lastly, to my beautiful and loving wife Dr. Mary A. Sorensen, who has dealt with ups and downs of graduate school while supporting me unconditionally.

The text of this dissertation, in part or in full, is a reprint of the material as it appears in the following journals:

- Molecular Simulation [1]

- Physica Status Solidi (a) [2], copyright Wiley-VCH Verlag GmbH and Co. KGaA, reproduced with permission

- Small [3], copyright Wiley-VCH Verlag GmbH and Co. KGaA, reproduced with permission

- Journal of Computational Electronics [4], original publication is available at www.springerlink.com

- Journal of Nanoelectronics and Optoelectronics [5]

- Physical Review B [6, 7], copyright APS 2007 and copyright APS 2009

The co-author, R. K. Lake, listed in the above publications directed and supervised the research which forms the basis for this dissertation. The remaining co-authors listed provided technical expertise and support as collaborators. This work was supported by the NSF (ECS-0524501), the Microelectronics Advanced Research Corporation Focus Center on Nano Materials (FENA), and DARPA/DMEA-CNID (H94003-04-2-0404).

ABSTRACT OF THE DISSERTATION

High Throughput *Ab initio* Modeling of Charge Transport for Bio-Molecular-Electronics

by

Nicolas Alexander Bruque

Doctor of Philosophy, Graduate Program in Electrical Engineering
University of California, Riverside, June 2009
Dr. Roger K. Lake, Chairperson

Self-assembled nanostructures, composed of inorganic and organic materials, have multiple applications in the fields of engineering and nanotechnology. Experimental research using nanoscaled materials, such as semiconductor/metallic nanocrystals, nanowires (NW), and carbon nanotube (CNT)-molecular systems have potential applications in next generation nano electronic devices. Many of these molecular systems exhibit electronic device functionality. However, experimental analytical techniques to determine how the chemistry and geometry affects electron transport through these devices does not yet exist.

Using theory and modeling, one can approximate the chemistry and geometry at the atomic level and also determine how the chemistry and geometry governs electron current. Nanoelectronic devices however, contain several thousand atoms which makes quantum modeling difficult. Popular atomistic modeling approaches are capable of handling small molecular systems, which are of scientific interest, but have little engineering value. The lack of large scale modeling tools has left the scientific and engineering community with a limited ability to understand, explore, and design complex systems of engineering interest.

To address these issues, I have developed a high performance general quantum charge transport model based on the non-equilibrium Green function (NEGF) formalism using density functional theory (DFT) as implemented in the FIREBALL software. FIREBALL is a quantum molecular dynamics code which has demonstrated the ability to model large molecular systems. This dissertation project of integrating NEGF into FIREBALL provides researchers with a modeling tool capable of simulating charge current in large inorganic / organic systems.

To provide theoretical support for experimental efforts, this project focused on CNT-molecular systems, which includes the discovery of a CNT-molecular resonant tunneling diode (RTD) for electronic circuit applications. This research also answers basic scientific questions regarding how the geometry and chemistry of CNT-molecular systems affects electron transport.

Contents

List of Figures

List of Tables

Chapter 1

Rationale

1.1 Introduction

Hybrid inorganic-organic, biologically inspired, molecular self-assembled nanostructures have a wide range of applications in the fields of engineering and nanotechnology. These complex systems bring together disparate materials such as metals, semiconductor nanocrystals/wires, DNA, proteins, peptides, carbon nanotubes (CNT) and individual molecules to form functional nanoelectronic devices. These materials have the ability to direct self-assembly of electronic circuits [11–15], operate as senors [16, 17] and link single molecule junctions [18–21]. Many of these systems exhibit electronic device functionality depending on chemical and structural configuration of the molecules. Experimental efforts using these hybrid self-assembled molecular-based systems are one of the transformative technologies being researched by the semiconductor industry for post-Si electronics.

The progress associated with fabricating and operating these hybrid structures has been accompanied with several challenges, namely understanding the exact properties which dictate the current response through individual molecules connected via nanoscale contacts. Understanding charge transport through these hybrid materials and developing the ability to control the contact chemistry to individual nanomaterials continues to be long and complicated process. These systems, in general, are difficult to characterize since there are no known analytical experimental techniques to verify the chemistry and atomic structure. Furthermore, the current response of individual molecules can be largely determined by the contact chemistry and atomic structure.

Using theory and modeling, one can approximate the chemistry/geometry at the atomic level and identify promising configurations for functional electronic applications. Full scale nanoelectronic devices are theoretically difficult to model using standard semi-empirical methods due to the complex interactions that occur between organic and inorganic systems. Over the last decade, first-principle Density Functional Theory (DFT) approaches have been used as an alternative to study charge transport through these hybrid systems. DFT is a mean field theory approach [22,23] used to predict the ground state electron structure of molecules/clusters and more recently transport across complex heterojunctions [24–27].

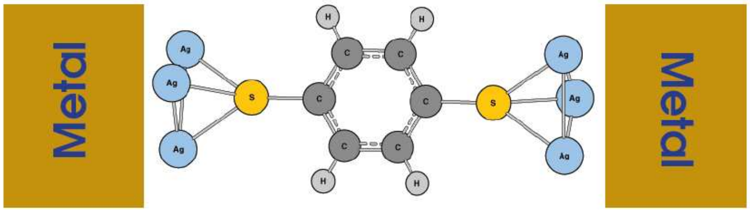

Figure 1.1: Schematic view of a Benezene dithiol molecule coupled to gold contacts.

Modeling such systems with the existing density functional theory (DFT) - non-equilibrium Green function (NEGF) software is difficult at best. The BDT systems were first studied using Gaussian98 [28–31], a density functional theory (DFT) software, combined with NEGF [20, 32–36]. Figure (1.1) shows an example of the type of system modeled. The studies performed by Datta and Ratner revealed interesting device characteristics but the computational model is limited to small molecular systems. Another proprietary computation materials code titled TranSIESTA carries a NEGF package which again has only been used to model small molecules due to heavy strain on the core processing algorithm [25, 27].

Other DFT software packages have emerged in recent years however many of these models are again computationally restricted to smaller subset models of experimental molecular nanoscale systems. Furthermore, software implementations are limited for further development since these codes have been implemented within proprietary software licenses such as GAUSSIAN98 [32] or TranSIESTA [27]. Ultimately this has left the scientific and engineering community with many open questions and limited tools to theoretically understand, explore, and design large nanoscale systems of engineering interest.

To address these issues, this dissertation project involved developing a general purpose quantum charge transport model based on the non-equilibrium Green function (NEGF) approach coupled to the *ab initio* DFT software FIREBALL [23, 37–42]. FIREBALL has demonstrated the ability to model the electronic structure of large complex atomic systems without supercomputer level facilities. The integration of FIREBALL with NEGF provides researchers the ability to model charge transport of realistic structures. The high-speed and linear scaling features already incorporated into FIREBALL also complement the NEGF recursive formalism for 1000+ atoms. The FIREBALL/NEGF package has answered and supported experimental efforts studying transport through CNT-molecule-CNT hybrid systems. This project lays the foundation to model and understand charge transport through bio-molecule electronic systems and provides theoretical guidance to experimental efforts for applications in nanotechnology.

1.2 Background and Motivation

1.2.1 CNT/Molecular Nanoelectronics

Over the past decade, there has been an intensive debate concerning the future of nanoscale electronic devices. Performance, power density and fabrication costs continue to challenge the progress of continued scaling of silicon based nanoscale FETs. According to the Interntional Tehcnology Roadmap for Semiconductors (ITRS) [43], the cell size (spatial pitch) for a silicon metal-oxide field effect transistor (MOSFET) will reach an ultimate scaling limit around 100 nm. Furthermore, the costs of 'top-down' lithographic fabrication techniques continues to increase exponentially with each newly released generation of mircoprocessor.

To address the aforementioned issues, research efforts have turned to alternative materials and structures such as silicon/germanium nanowires, carbon nanotubes, biological linkers and individual molecules for possible circuit applications [44–52]. These materials, provided that a well-ordered process for assembly emerges, are projected to have device densities at least twice that of silicon. Experimentally fabricated electrochemical, optical and photochemcial biosenors have already shown the merging of molecular based organic/inorganic systems for electronic sensor applications. Examples of these bio-senors include metallic-semiconductor nanoparticles with enzymes [16, 17], nucleic acids, [53–55] and antigens/antibodes [56]. Molecular biomaterials also have the features of specificity and recognition in their binding that make them promising for directed assembly of nanoscale hybrid materials. Examples include the complementary base pairing of DNA [48–50], antigen-antibody binding [50], and the material specific binding of virus bound peptides [57].

To complement the development of the FIREBALL/NEGF model, much of the nano device studies presented here will focus on supporting experimental CNT - molecule systems. The following chapters cover transport studies of CNTs functionalized with peptides, DNA, and peptide nucleic acid (PNA) for self-assembly applications [50,58–66], conductance trends due to changes in the CNT-molecule interface geometry [6], and conductance calculations of a well characterized experimentally fabricated CNT-molecule-CNT system [7,67].

1.2.2 Bio-Assembled CNT Field Effect Transistors

The progress associated with CNTFET experimental research has been accompanied by the challenge of integration or the process of linking together CNT field effect transistors (FET) for practical applications in digital logic circuits and memory. The state-of-the-art is similar to that of silicon prior to the invention of the monolithic integrated circuit. In order for CNTs to be used in nanocircuit applications, a well-defined placement process is required. However the construction of complex architectures, using high density nanoscale CNTs, requires a largely parallel bottom-up approach [5].

Methods to control the placement of CNTs use microfluidics [68, 69], electric fields [70,71], direct patterning using side edges of multilayered films [72,73], gas-flow directed growth [74], and the self-alignment of CNTs on the a-planes and r-planes of sapphire substrates [75,76]. An alternative integration scheme uses biological mechanisms for directed self-assembly of a CNT field-effect transistor (CNTFET) [50,58]. Architectures built using bio-assembly have been discussed [59,60].

One bottom-up approach involves the use of bio-molecular linkers, such as DNA or PNA, which provide specificity allowing unique labeling of CNTs. An example of a functionalized CNT can be seen in Fig. 1.2 where a single-strand PNA is connected to a zigzag (10,0) CNT with a Glutamate (Glu) linker. The covalent or the self-

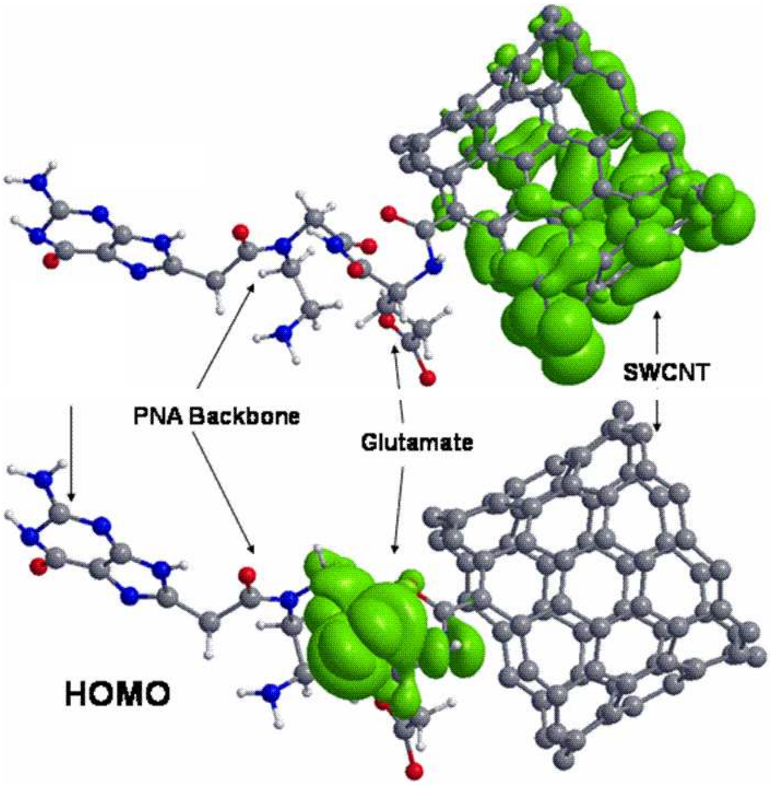

Figure 1.2: Highest occupied molecular orbital (HOMO) and lowest unoccupied molecular orbital (LUMO) for a model PNA-Glutamate-CNT assembly

assembled functionalization of single walled carbon nanotubes with the molecular material of interest is done by oxidizing the CNTs with nitric acid which removes the caps and terminates the CNT with the carboxylic group (-COOH). The end functionalization is then completed by the EDC coupling reaction which results in linking the CNT with the material of interest via a functionalized linker. Most of the CNT-molecule systems studied here will involve the use of amide linkers (-CONH-) [61, 62, 77]. The amide linker will serve as the interface between the CNT and the molecule of interest in functionalization.

There are several possible types of electronic applications for bio-inspired CNT integration. In the first type, the high-level digital architecture is retained, but silicon is replaced by bio-assembled CNTFETs. A conceptual hybrid self-assembled CNTFET

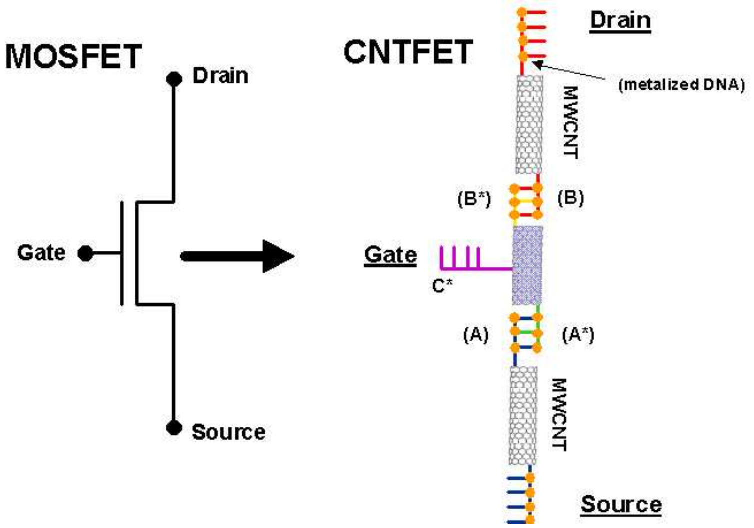

Figure 1.3: Conceptual overview of a self-assembled organic/inorganic electronic device of CNTs functionalized using conjugate DNA base pairs.

structure is shown in Fig. 1.3 where the traditional metal-oxide field effect transistor (MOSFET) is represented with functionalized CNT parts.

One could combine the CNTFETs into a simple self-assembled inverter as shown in Fig. 1.4 [5, 8]. Functionalization of the sidewalls of the CNTFET channels could be achieved with nanofluidic techniques. Other assembly schemes, on a 2D contact grid, could be used to construct a wide range of logic gate devices by pre-engineering the number of DNA/PNA base pairs linked to the ends of the CNTs. From an engineering point of view, the DNA and PNA bio-molecular linkers should be considered as insulators. To create conducting interconnects, the organic linkers are metallized [64, 65, 78, 79]. This is synergistic with the discovery and advancement of zero-Schottky-barrier contact technology for CNTFETs [80–85] since Pd metallization of DNA has been demonstrated.

Clearly, one would want to make the CNT network as large a possible before taking its output out to a metal pad. The metal pad would likely provide a large capacitive output load to a CNTFET composed of a single CNT. Without the ability to cross

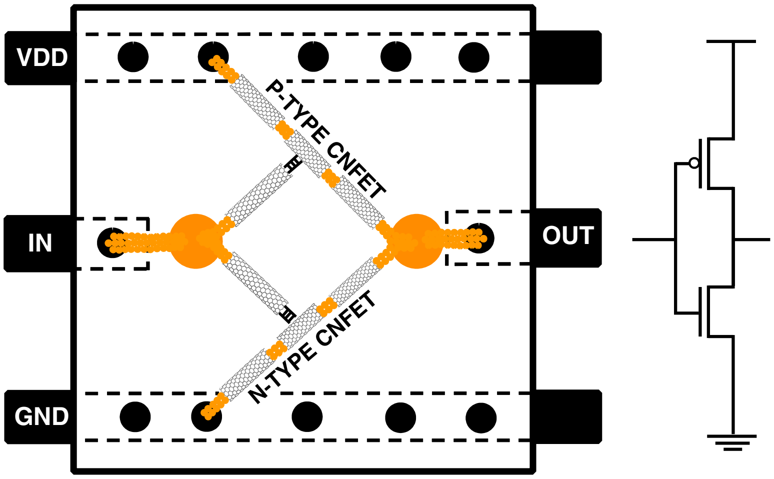

© American Scientific Publishers

Figure 1.4: Layout of a bio-assembled CNTFET inverter. CNTs with dark boarders represent active devices. Remaining nanotubes represent ohmic metallic multiwall CNT connections. Small gold circle clusters at interfaces represent metallized DNA/PNA. Three-way metal junctions are formed using a functionalized metal cluster [5, 8].

CNT interconnects, the size of the network is strongly limited by its 2 dimensional nature. A Si analogue would be a process with only one metal level.

Another method to implement digital architecture is to use DNA-based arrays as templates for organizing heteromaterials [86–88]. Fully addressable DNA arrays have recently been reported [88]. The demonstrated self-assembly techniques described in Refs. [50, 58, 79, 88], give rise to the possibility of building a bio-assembled, cross-bar, logic circuit [89, 90]. An illustration of a NOR gate synthesized on a DNA array is shown in Fig. 1.5.

The underlying gray grid represents the DNA array. The horizontal gold lines represent metallized DNA. The metal lines would optimally be made from different metals to facilitate n-type and p-type ohmic contacts. To reduce unwanted gating, certain cross-points would be built up to lift the CNT away from the metal. The CNTs, possibly chemically treated to be n-type, p-type, or coated with a thin dielectric, would be attached to the columns of the DNA array. Voltage annealing would be used to fuse ohmic contacts at cross-points. The issue of interfacing to the lithographic scale environment, which has recently been demonstrated in semiconductor cross-bar arrays [91], would have to be solved. One can envision a metal-patterned substrate with DNA functionalized anchor pads to anchor and orient the DNA arrays to the substrate. The ability to uniquely address rows, columns, and segments thereof of the DNA array is primary assumption underlying this proposed bio-assembled, cross-bar, logic gate.

1.2.3 Molecular Electronic Devices Using CNT Contacts

In addition to providing a means to chemically integrate CNTs, molecules can also serve as the channel of a FET. For FET applications, individual molecules are regarded as the ultimately scaled electronic device in future electronics [18–20, 92–94]. Their size is truly at the nanometer scale, and they have a natural uniformity. Well known examples of molecules providing electrical functionality are 2'-amino-4-ethynylphenyl-4'-ethyny-lphenyl-5'-nitro-1-benzenethiolate (BDT) [95] and rotaxane [14]. Applying a voltage bias across these molecules causes a conformational change which results in bistability of the molecular conductance. Fabricating and understanding electron/hole transport from contact to molecule however continues to be troublesome.

The current response of an individual molecule can be largely determined by the contacts. As an extreme example, at one point, there was widespread concern that interesting switching effects observed in current-voltage measurements of molecules in a cross-bar architecture were solely contact effects, completely independent of the molecules sandwiched between the contacts [96]. Understanding and developing the ability to control nanoscale contacts to individual molecules has been a long and difficult process.

Metal contacts to molecules using a thiol linker to gold were the first ones to be used by experimentalists and have, therefore, been studied the longest and been given the most attention, both experimentally and theoretically [18–21, 24, 92–94, 97–100]. For many years, there was little correspondence between the experimentally measured currents in such systems and the theoretically predicted currents, although the correspondence has become much closer. Several good reviews describe and document the history and present state of affairs [52, 101, 102]. Uniformity of measurements was greatly improved with the introduction of amine linkers to gold contacts [103–107]. This demonstrated sensitivity of molecular conductance to the linker molecule is one of the motivations for this dissertation.

Semiconductor materials, in particular silicon, contacts to molecules are a more recent development in the molecular electronics world [33, 108–114]. Molecular contacts to Si can be formed by strong covalent bonds eliminating some of the variation observed with metal - molecule contacts. Furthermore, in Si-molecule systems, the semiconducting band structure of the Si contact can give rise to enhanced electronic functionality such as that of a resonant tunneling diode exhibiting negative differential resistance, although the standard explanation of this effect [33, 111] has recently been questioned [115].

The most recent system to be considered both experimentally and theoretically is a carbon nanotube (CNT)-molecule-CNT system [1–3, 5, 6, 66, 67, 67, 116, 117]. The CNT-molecule-CNT structure has been shown to be superior to gold metal contacts both theoretically [118, 119] and experimentally [120]. The use of CNTs as molecular contacts also avoids the problems associated with metal electrodes and the problems found using thiol chemistry. The CNT - molecule attachment chemistry is a covalent bond [67]. The CNT electrodes are of the same physical size scale as the molecules that they contact. Depending on the chirality of CNTs, the contacts could be a physical implementation of a (i) metal-molecule-metal system or a (ii) semiconductor-molecule-semiconductor system. This dual nature offers molecular functionality and is a candidate for molecular scale electronics [121, 122]. Of interest for electronic device applications, negative differential resistance (NDR) has also been theoretically predicted for such a system [2, 5] and is discussed in Chapter 3.

1.3 Objective

Much of the CNT-molecule-CNT structures mentioned have a limited theoretical foundation for understanding charge transport. It is widely recognized that the interface chemistry and atomic configuration plays a crucial role in metal - molecule -metal junctions [21, 52, 101, 123]. however, modeling capability has not kept up with the experimental work.

The objective of this dissertation is to model and answer several open questions, namely how the chemistry and geometry of the CNT - molecule interface affects the electron transport and conductance by developing a general all-purpose transport model. This work lays the foundation to fill a technical need for all nano device research. This project will ultimately place the FIREBALL/NEGF software into the hands of the international community so that the scientific discovery process can proceed world-wide with the software developed.

For computational facilities, two Linux Beowulf clusters were built and configured for Dr. Lake's research group, the LAboratory for Terascale and Terahertz Electronics (LATTE). This modeling effort was in direct collaboration with the experimental chemical and biological research associated with the Semiconductor Research Corporation Focus Center FENA at UCLA and Phillip Collins Group at UC Irvine.

1.4 Layout

This dissertation consists of eight chapters. Chapter one provides an introduction and background literature for the research. Chapter two will covers the theoretical foundation of NEGF and FIREBALL. Chapter three covers the verification of the FIREBALL/NEGF model. Chapter four covers the charge transport properties of a semiconducing CNT-peptide-CNT and CNT-DNA-CNT structure. Chapter five covers how the CNT-molecule contact geometry influences transport across π-conjugated systems. Chapter six calculates the conductance of a well characterized CNT-molecule-CNT experimental system. Chapter seven summarizes recent developments and transport calculations through a nanometer length (1000+ atom) system using the FIREBALL-NEGF RGF approach. Closing remarks and summary end in chapter eight. The appendix will cover details regarding NEGF input files and LATTE's Beowulf clusters.

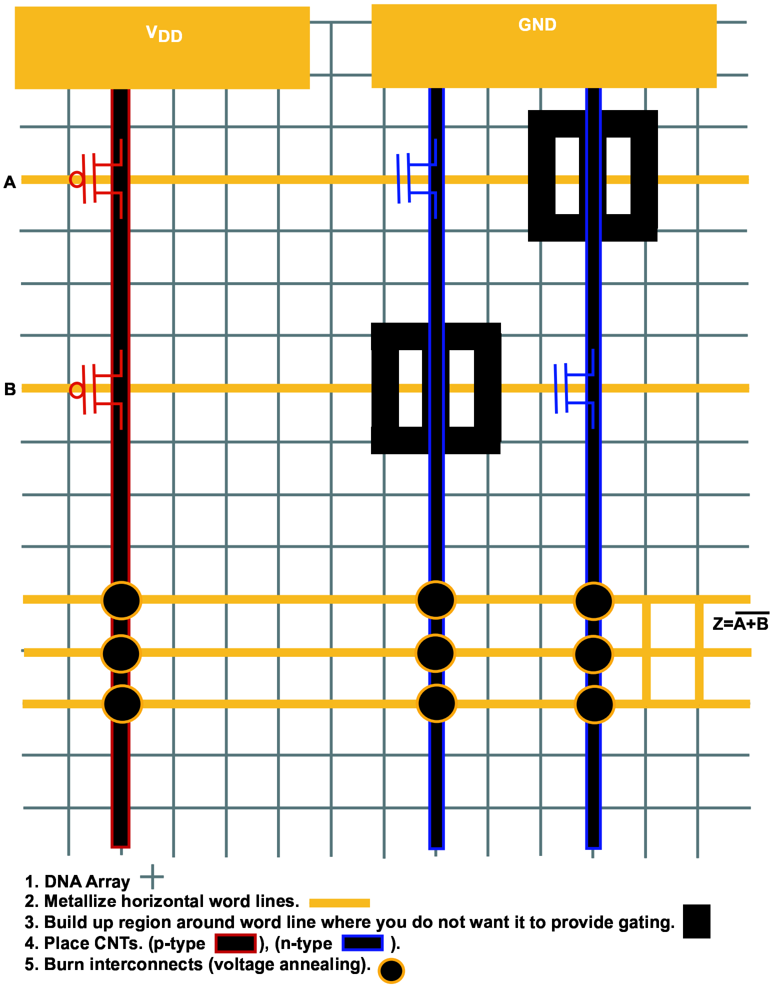

1. DNA Array +
2. Metallize horizontal word lines.
3. Build up region around word line where you do not want it to provide gating. ■
4. Place CNTs. (p-type 🟥), (n-type 🟦).
5. Burn interconnects (voltage annealing). ●

© American Scientific Publishers

Figure 1.5: Layout of a bio-assembled, cross-bar NOR gate. The gray grid is the underlying DNA array. Gold colored horizontal lines are metal (not necessarily identical). Vertical black lines are CNTs (red outline indicates p-type and blue outline indicates n-type). Black rectangles represent regions built up to lift the CNT away from the metal line. Circles represent ohmic contacts formed by a voltage anneal.

Chapter 2

Theoretical Background

2.1 Overview

This chapter first covers an overview of the basic theory being the FIREBALL approach. The bulk of the chapter covers the development, integration and evaluation of the non-equilibrium Green function approach within the FIREBALL package. The sections covered in this chapter are summarized here:

(1) Molecular Dynamics/Structure Optimization: All CNT-molecule-CNT structures are relaxed using an assortment of DFT packages. Gaussian03 [124] and FIREBALL [23, 37–39, 42] are both routinely employed using periodic and non-periodic conditions to optimize structures throughout this dissertation. Typically all structures are relaxed until all Cartesian forces on the atoms are < 0.05 eV Å^{-1}. A Fermi smearing temperature of 50 K and a self-consistent convergence factor of 10^{-5} are routinely used. The 1-D Brillouin zone for periodic CNT-molecule-CNT systems, is normally sampled with 32 k-points during optimization. Each chapter will note the optimization process used.

(2) Non Self-Consistent Transport: Once the structure is relaxed with a converged

charge density, the Hamiltonian and overlap matrix elements are taken from FIREBALL. The matrices are used in a post-process Green function algorithm to calculate equilibrium transmission and conductance [6].

(3) Self-consistent Transport: This section completes the development of the NEGF transport model. The FIREBALL package is coupled directly to NEGF in a self-consistent loop where the charge density is calculated using NEGF. This approach is used to determine the image potential between the two CNTs self-consistently in Chapter 6.

2.2 FIREBALL

2.2.1 FIREBALL Software Package

The FIREBALL software suite [23,39] is developed and distributed primarily at West Virginia University under James P. Lewis' group. The foundation of the FIREBALL method is a self-consistent generalization of the Harris-Foulkes energy functional [125, 126] known as DOGS named after the original authors [37,38,42]. The FIREBALL suite consists of three sub-programs, PP, BEGIN and CREATE which are used to calculate and store the precomputed wavfunctions for the main FIREBALL application.

The PP (pseudopotential) program uses generalized norm-conserving separable pseudopotentials as reported by D. R. Hamann [127] or Troullier-Martins [128] to approximate the core electronic structure for each atomic species. The BEGIN package next generates the cutoffs for the slightly excited pseudo-atomic valence shell wavefunctions for the free atom which have a pre-defined cutoff r_c. CREATE next calculates and stores the one, two, and three-center integrals for all possible wavefunction interactions within a non-orthogonal basis set. Lastly, the wavefunction database is read by FIREBALL application to run molecular-dynamics simulations and calculate the quasi eigen-energies (electronic structure) for non-periodic (clustered) or periodic systems. The NEGF package is integrated directly in the FIREBALL SCF calculation.

2.2.2 Energy Functional

The FIREBALL method incorporates either the Local Density Approximation (LDA) or Generalized Gradient Approximation (GGA) exchange correlation energies within the Harris-Foulkes energy functional. [23, 39].

$$E_{tot}^{Harris} = E^{BS} + (U^{ion-ion} - U^{ee}[\rho_{in}(\mathbf{r})]) + (U^{xc}[\rho_{in}(\mathbf{r})] - V^{xc}[\rho_{in}(\mathbf{r})]) \tag{2.1}$$

E^{BS} is the band structure energy or ($2\sum_i \epsilon_i$) is obtained by summing the eigenvalues over occupied states, ϵ_i, of the one-electron Schrödinger equation. The second term describes the the difference between the repulsive "short-range" interactions of the ion pseudocores offset by the electron-electron repulsion interactions. The last term is the exchange correlation method (LDA or GGA) defined in Eq. (2.2).

$$U^{xc}[\rho_{in}(\mathbf{r})] - V^{xc}[\rho_{in}(\mathbf{r})] = \int \rho_{in}(\mathbf{r})(\epsilon_{xc}[\rho_{in}(\mathbf{r})] - \mu_{xc}[\rho_{in}(\mathbf{r})])d^3r. \tag{2.2}$$

The eigenvalues of the one-electron Schrödinger equation contain the potential $\mu_{xc}[\rho_{in}]$ and the correct exchange-correlation interaction energy is $\int \rho_{in}(\mathbf{r})\epsilon_{xc}[\rho_{in}(\mathbf{r})]d^3r$. When evaluating the total energy of the system the input charge density, defined in Eq. (2.3), is the sum of all the confined atomic-like densities.

$$\rho_{in}(\mathbf{r}) = \sum_i n_i \mid \phi_i(\mathbf{r} - \mathbf{R}_i) \mid^2 \tag{2.3}$$

. The orbital basis states $\{\phi_i(\mathbf{r}-\mathbf{R}_i)\}$ are pseudoatomic wavefunctions for solving the one-electron Schrödinger equation. The n_i term represents the electron occupation number in each spherical orbital around an atom at position $\mathbf{R}_i$. The orbitals $\{\phi_i(\mathbf{r}-\mathbf{R}_i)\}$ are slightly excited pseudopotential orbitals where the wavefunction cutoffs determine the excitation energy. During the BEGIN calculation the wavefunction cutoffs, r_c, for each atomic species are chosen such that the ionization energies are preserved. Typically an excitation energy of $\sim 2.0eV$ above the ground state energy is used for determining the cutoffs. For hydrogen bonded systems, an excitation energy of $\sim 1.4eV$ is recommended to extend the wavefunctions about 10%. The theoretical basis for choosing the cutoffs is discussed in Ref. [38].

With the boundary conditions of each atomic species defined, a fixed grid of localized orbitals is established. This gives a preprescribed interaction range for the orbitals where the integrals only need to be calculated once and saved. After the integrals have been evaluated numerically, an interpolation of the saved data can construct a nearest neighbor (sparsely filled) Hamiltonian and overlap matrix for any nanostructure.

The Harris-Foulkes equation by itself is not a self-consistent system however a self-consistent generalization has been implemented and developed by A. A. Demkov, J. Ortega, M. P. Grumbach and O. F. Sankey (DOGS) [37,38]. A reference "atomic" density ($n_i = n_i^0$) is used for determining the initial input density. For systems that exhibit a significant transfer of charge between atoms, a self-consistent determination of the occupation number n_i is replaced with ($n_i = n_i^0 + \delta n_i$). This modifies the total energy functional as dependent on the electron occupation numbers where $E_{tot}[\rho_{in}(\mathbf{r})] = E_{tot}[n_i](n_i \neq n_i^0)$. Details regarding how the exchange-correlation are affected by this functional can be found in Ref. [129].

FIREBALL calculations are typically performed using the BLYP exchange-correlation functional (GGA) for inorganic/organic hybrid materials [130]. For calculating the exchange-correlation interactions, a multicenter exchange-correlation method (McWEDA) is used that combines the best features of the Sankey-Niklewski (SN) and Horsefield exchange-correlation (HXC) approaches [42] while still maintaining computational efficiency. McWEDA uses weighted density functions to calculate on-site (off-site) exchange-correlation matrix elements using localized (*d* orbitals) and free-electron-like (*sp* orbitals) states. The McWEDA approach corrects the main deficiencies of the SN and HXC approximations, such that structures composed of semi-conducting materials and transition metals are in closer agreement with experimental band structures.

2.2.3 Wavefunction Cutoffs

In this dissertation, we use the following s-orbital and $p_{x,y,z}$-orbital cutoff values: r_c^{1s} = 4.10 Å for hydrogen; r_c^{2s} = 4.4 Å and r_c^{2p} = 4.8 Å for carbon; r_c^{2s} = 4.0 Å and r_c^{2p} = 4.4 Å for nitrogen; r_c^{2s} = 3.7 Å and r_c^{2p} = 4.1 Å for oxygen.

The finite cutoffs for the orbitals combined with an interpolation method of integrals provides an efficient technique for studying complex electronic structures. This approach provides a faster means for molecular dynamic simulations within the *ab initio* DFT framework.

2.3 Non Self-Consistent Transport

The NEGF calculation in this section operates as a post-processor to the FIREBALL calculation as shown in fig. 2.1. The transmission calculation is a three step process which uses FIREBALL's built-in eigen value solver to calculate a converged charge density and generate the standard Green function for equilibrium transmission and

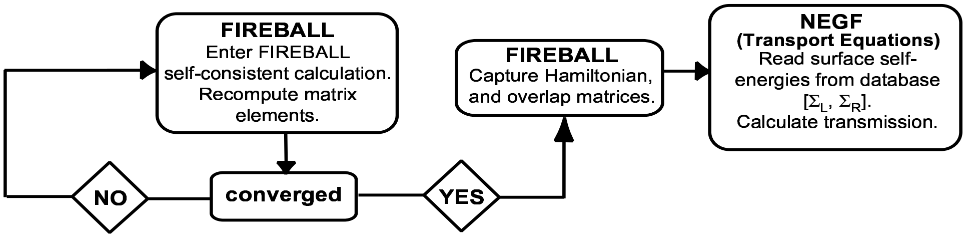

Figure 2.1: Flowchart diagram of Post Processing NEGF/FIREBALL model

conductance. The first step is to run a self-consistent DFT FIREBALL calculation of an ideal periodic bulk material directly corresponding to the source and drain contacts. The contact Hamiltonian and overlap matrix elements are stored for calculating the surface self-energies. The second step is to run a self-consistent DFT calculation of an extended finite (clustered) or periodic metal-molecule-metal structure. After the self-consistent calculation, we remove several atomic bulk contact layers from the end of the leads (finite system only) and store the Hamiltonian and overlap matrix elements of the reduced device structure. For the third step, the saved matrix elements are used to calculate the surface self-energies, the Green function of the device, and the resulting transmission. For reference, the following sections will use CNTs as an example contact material.

2.3.1 Self-Energies

The surface self-energies are first calculated using a decimation technique [131, 132] from a *periodic* CNT, consisting of a four-atomic-layer unit cell along the growth direction. Each CNT type (armchair/zigzag) pictured Fig. 2.2, is divided by four atomic layers. Non-zero matrix elements of a given atomic layer extend to the left and right 4 atomic layers, or one unit cell of the zigzag/armchair CNT. In terms of the 4-atomic layer unit cells, there is only nearest neighbor unit-cell coupling.

The CNT Hamiltonian matrix elements are grouped into inter-cell subblocks $t_{i,i\pm1}$

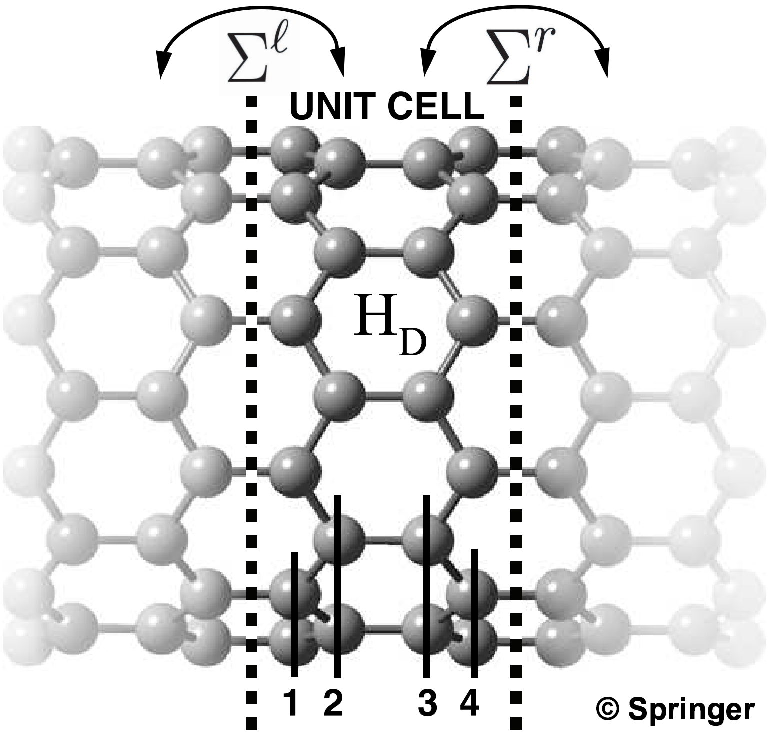

Figure 2.2: One unit cell (10,0) zigzag CNT with 4 atomic layers. Self-energies take into account the semi-infinite leads for transmission calculations.

and intra-cell subblocks $D_{i,i}$. We define inter-cell matrix elements $\tilde{t}$ as

$$\tilde{t}_{i,j} = t_{i,j} - (E + i\eta)S_{i,j} + U_{i,j} \tag{2.4}$$

where $S_{i,j}$ is the overlap matrix between non-orthogonal orbitals in cells i and j, E is the energy, $U_{i,j}$ is the potential, and η is a convergence factor that is non-zero only in the contacts. The potential energy matrix U represents the electrostatic Laplacian solution $\nabla^2\Phi = 0$ which has both a diagonal block component and an off-diagonal block component calculated using a standard Huckel approach where [2, 24]. $U_{i,j}$ is initially calculated using a standard real-space (vacuum dielectric) mesh grid approach part of the GNU software package MUDPACK, version 5.0.1 [133].

$$\mathbf{U}_{i,j} = -e\frac{\mathbf{V}_i + \mathbf{V}_j}{2}\mathbf{S}_{i,j}. \tag{2.5}$$

The matrices V_i that occur in Eq. (2.5) are diagonal with the value of the macroscopic electrostatic potential at each atom on the diagonal. The off-diagonal blocks, $U_{i,j}\pm 1$, are incorporated into the $\tilde{\mathbf{t}}$ matrices in Eqs. (2.23) - (2.24), and the diagonal blocks, $\mathbf{U}_{i,j}$, are shown explicitly.

For calculations presented below, $\eta = 10$ meV is typically used. The equations that we solve for the surface green function are

$$\begin{aligned}
\tilde{t}_i &= \tilde{t}_{i-1}\left[(E + i\eta)S_{N+1,N+1} - D_{i-1}\right]^{-1}\tilde{t}_{i-1} \qquad (2.6)\\
\tilde{t}_i^{\dagger} &= \tilde{t}_{i-1}^{\dagger}\left[(E + i\eta)S_{N+1,N+1} - D_{i-1}\right]^{-1}\tilde{t}_{i-1}^{\dagger}\\
D_i &= D_{i-1} + \tilde{t}_{i-1}\left[(E + i\eta)S_{N+1,N+1} - D_{i-1}\right]^{-1}\tilde{t}_{i-1}^{\dagger}\\
&+ \tilde{t}_{i-1}^{\dagger}\left[(E + i\eta)S_{N+1,N+1} - D_{i-1}\right]^{-1}\tilde{t}_{i-1}\\
D_i^s &= D_{i-1}^s + \tilde{t}_{i-1}\left[(E + i\eta)S_{N+1,N+1} - D_{i-1}\right]^{-1}\tilde{t}_{i-1}^{\dagger}
\end{aligned}$$

Equations (2.6) define an iterative Hamiltonian for a chain of principal layers (unit cells) with lattice constant 2^ia, where a is the zero-order lattice constant and i is the iteration number. $\tilde{t}$ and $\tilde{t}^\dagger$ are the Hamiltonian matrices coupling 4-atomic-layers or one unit cell to ether side of the principal unit cell. A potential is added to the energy in non-equilibrium conditions ($E - \mu^{L,R}$) for a given source/drain chemical potential on the left(L) and right(R) contacts. The D^s's are the zeroth-order Hamiltonian matrix elements of the principal unit cell. For the surface Green function of the left lead, the calculation starts with the initial guess $D_0 = D_0^s = D_{0,0}$, $\tilde{t}_0 = \tilde{t}_{0,-1}$, and $\tilde{t}_0^\dagger = \tilde{t}_{-1,0}$. The surface green function convergence factor, which typically requires approximately 12 self consistent iterations, is met when the maximum value of any element of the $\tilde{t}$ matrix is less than 10^{-10}. After convergence of Eqs. (2.6) at iteration n, the surface Green function on the left lead is

$$g_{0,0} = \left[ES_{0,0} - D_n^s - U_{0,0}\right]^{-1}. \tag{2.7}$$

The self-energy matrices are calculated from the expressions

$$\begin{aligned} \Sigma^\ell &= \tilde{t}_{1,0} g_{0,0} \tilde{t}_{0,1} \qquad (2.8) \\ \Sigma^r &= \tilde{t}_{N,N+1} g_{N+1,N+1} \tilde{t}_{N+1,N}. \end{aligned}$$

where Σ^ℓ and Σ^r are the surface self-energies for the left and right CNT contacts respectively. Further details of this approach can be found in refs. [1, 2, 5].

2.3.2 Full Retarded Green Function

The second step is to run a self-consistent FIREBALL DFT calculation of the extended finite CNT-Mol-CNT structure with a convergence factor of 10^{-4}. After convergence, the NEGF calculation begins by truncating the outside unit cells of each CNT contact for a clustered system and adding the self-energy matrices Σ^ℓ and Σ^r onto the new outer unit cell of the truncated CNTs. For periodic systems this step is skipped. The self-energies are placed on a unit cell where low charge oscillations occur on the CNT contacts. An example finite (clustered) CNT-DNA-CNT structure is shown in Fig. 2.3 which consists of two unit cells (8 atomic layers) of a CNT for each contact. We number the outside unit cell on the left CNT as 1 and the outside unit cell on the right CNT as N At each energy E, the retarded Green function [134] is calculated from

$$G^R(E) = \left[ES_D - H_D - U_D - \Sigma^\ell - \Sigma^r\right]^{-1} \tag{2.9}$$

D represent the 'device' region of structure.

2.3.3 Transmission and Current

The transmission spectrum, $T(E)$, is calculated from the standard Green function expression,

$$T(E) \ = \ \mathrm{tr}\left\{\Gamma^B_{1,1} G^R_{1,N} \Gamma^B_{N,N} G^R_{1,N}\right\} \tag{2.10}$$

where $\Gamma^B_{1,1} = \Gamma^\ell = i\left(\Sigma^\ell - \Sigma^{\ell\dagger}\right)$ and $\Gamma^B_{N,N} = \Gamma^r = i\left(\Sigma^r - \Sigma^{r\dagger}\right)$. H_D and S_D are the Hamiltonian and overlap matrices, respectively, of the CNT-molecule-CNT system. An adaptive energy grid is implemented to resolve sharp resonance peaks in the transmission spectra. Peaks are searched as a percentage difference between each transmission point.

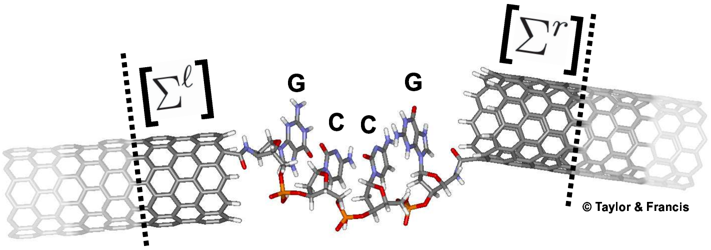

Figure 2.3: Illustration of the truncation of the CNT leads and the addition of the surface self-energy to the matrix elements of the last unit cell. This converts the finite CNT into the surface of a semi-infinite CNT.

The current is obtained from

$$I = \frac{2e}{\hbar} \int \frac{dE}{2\pi} T(E) \left[f(E - \mu_L) \; - \; f(E - \mu_R) \right] \tag{2.11}$$

where $f(E)$ is the Fermi function, and μ_L and μ_R are the electrochemical potentials of the left and right contacts, respectively.

To understand the spatial extent of states for a given energy, we calculate and plot the covariant spectral function [135]

$$A_j(E) \; = \; -2 \, \mathrm{Im} \left[\mathrm{tr}_j \left(S G^R(E) S \right) \right] \; = \; i \; \mathrm{tr}_j \left[S \left(G^R(E) - G^{R^\dagger}(E) \right) S \right] \tag{2.12}$$

where the trace is over the basis states associated with atom j. The second equality in Eq. (2.12) is obtained noting that the S matrices are real and symmetric. The spectral function is visualized using two methods. One method uses 3D layered contours rendered transparently over all the atoms where the highest atomic spectral values calculated from Eq. 2.12 are plotted in darker regions (red) decreasing to lighter gray areas (purple). The second method plots the value of the covariant spectral function $A_n(E)$ associated atoms between contacts. In order to determine decay constants in the molecule, we also calculate the covariant left and right connected spectral functions defined respectively by

$$A_i^{\ell}(E) \;=\; \mathrm{tr}_i \left\{ SG^R(E)\Gamma^{\ell}(E)G^{R^\dagger}(E)S \right\} \tag{2.13}$$

and

$$A_i^{r}(E) \;=\; \mathrm{tr}_i \left\{ SG^R(E)\Gamma^{r}(E)G^{R^\dagger}(E)S \right\}. \tag{2.14}$$

These functions correspond to the magnitude of the wavefunction squared injected from the left or right contact, respectively.

To calculate the conductance, we take the derivative of the current equation with respect to the voltage where

$$G = \frac{\delta I}{\delta V} = \frac{2e^2}{\hbar} \int \frac{dE}{2\pi} T(E)(-\frac{\partial f}{\partial E}). \tag{2.15}$$

In Eqs. (2.11) and (2.15) $f(E)$ is the Fermi function, and the chemical potential μ is fixed at the Fermi energy E_f given by the DFT code FIREBALL.

2.4 Self-consistent Transport

An overview of the self-consistent field (SCF) FIREBALL-NEGF model can be seen in figure (2.4). Here the FIREBALL electron density calculation, which uses a standard eigenvalue solver, is bypassed using the NEGF approach. After FIREBALL has has generated the Hamiltonian and Overlap matrices from the input density, the NEGF self-consistent algorithm calculates a new charge density until the density converges. The transmission and I-V calculations are performed after the density has converged.

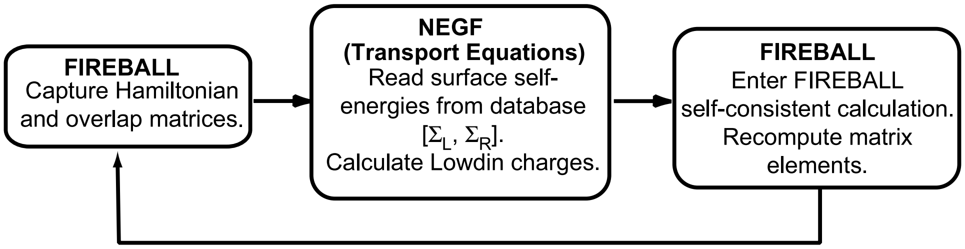

Figure 2.4: Flowchart of NEGF / FIREBALL self-consistent calculation

Electron Density

For non-equilibrium biases conditions, a self-consistent treatment is needed between FIREBALL and NEGF. The self-consistent approach of charge transfer within FIREBALL is described in detail in ref. [37]. As described earlier in section 2.2.1, the self-consistent calculation starts from the occupation numbers of the atomic-like orbitals on each atom ($(n_i = n_i^0)$). The electron occupation data set, otherwise known as the CHARGES, serve as the input to the energy functional. The occupation numbers, n_i, are stored as a sum of each valence shell and the difference δn_i represents the charge transfer between atoms such that the total energy functional is dependent on the electron occupation numbers ($E_{tot}[\rho_{in}(\mathbf{r})] = E_{tot}[n_i](n_i \neq n_i^0)$). For non-equilibrium transport calculations, the general eigenvalue solver is bypassed in the FIREBALL SCF loop and the CHARGES are calculated using the correlation function $\mathbf{G}^{<}_{i,j}(E)$ part of the NEGF approach.

The matrix elements of the short-range components are composed of the kinetic energy, ionic pseudopotential, neutral-atom Hartree and exchange-correlation potentials which are evaluated as described in the original paper of Sankey and Niklewski [23]. The matrix elements of the long-range part due to the non-neutral component of the Hartree potential are evaluated as described by Demkov et al. [37]. To ensure the electrostatic boundary conditions were met for non-equilibrium biases, the subroutines associated with the dipole expansion approach of [37] were examined to determine if the long range component could be modified for non-equilibrium transport.

After several months of study, the integral equation for the Hartree potential, which reduces to the sum of two-center terms summable exactly by Ewald summation techniques, could not be modified. Modifying or replacing this portion of the FIREBALL package with a 3D Poisson solution was also not successful as transport results were erroneous. Convergence of the charge density using a 3D grid was problematic. More details regarding this effort can be found in Chapter 7.

The electrostatic boundary conditions, which normally float in the Demkov approach, were instead pinned by freezing the charge density of the last 4 atomic layers at each contact. The charge density is copied after each self-consistent step to the last left and right atomic layer leads from a precomputed periodic bulk material (i.e. CNTs). The matrix elements of each cell and nearest coupling matrices are also fixed to the last two unit cell layers (8 atomic layers) of each lead to mimic the electrostatic potential of bulk leads. The pinning of the leads fixes the Fermi level which allows the 'device' charge density portions to converge exponentially assuming semi-infinite leads. The calculation of the resulting Hartree and exchange-correlation potentials are effectively left unchanged in the code as described in Ref. [37].

2.4.1 Recursive Green Function

To ensure that the electric field is well screened at the outer boundaries, the left and right leads are each extended to 10 nm. This results in a Hamiltonian matrix which is too large to store and invert directly. Therefore, we obtain the diagonal and first off-diagonal blocks of $\mathbf{G}^R(E) = \left[E\mathbf{S}_D - \mathbf{H}_D - \mathbf{U}_D - \mathbf{\Sigma}^\ell - \mathbf{\Sigma}^r\right]^{-1}$ using the recursive Green function algorithm. In Chapter 6, this method is used to calculate the charge induced on the contacts in response to a point charge placed between them. Below describes how RGF is implemented in the code.

The left, right, and device regions of the structure can be partitioned into a series of non-uniform block-layers each containing several atomic layers. Block layers $\{-\infty, \ldots, 0\}$ lie in the left contact, $\{1, \ldots, N\}$ lie in the "device," and $\{(N+1), \ldots, \infty\}$ lie in the right contact. The localized orbital cutoffs determine the minimum block-layer lengths across the system and are chosen such that the non-zero matrix elements only exist between nearest-neighbor block-layers. We will refer to "block-layers" as simply "layers," and specifically use "atomic-layer" to refer to a single atomic-layer within a block-layer.

We group the matrices into intra-layer subblocks $\mathbf{D}_{i,i}$ and inter-layer subblocks $\mathbf{t}_{i,i\pm1}$ where the bold font represents a matrix. The size of these matrices is equal to the number of orbitals per atom times the number of atoms in a particular layer. The layer that contains the molecule is typically larger than the layers in the CNT leads, since we have not attempted to partition the molecule into block layers. The off-diagonal inter-layer coupling matrices $\mathbf{t}_{i,i\pm1}$ are, in general, rectangular rather than square, since they can couple diagonal blocks of different sizes. Once the matrices are generated, they are saved and recalled as needed within the algorithm.

The number of electrons, n, associated with the orbitals of atom a is

$$n_a = 2 \sum_b \sum_{i,j} \int \frac{dE}{2\pi} \, \mathrm{Im} \left\{ G^<_{i,a;j,b}(E) S_{j,b;i,a} \right\} \tag{2.16}$$

The indices a and b indicate the atom and i and j represent an orbital. For a charge neutral atom, n_a is the integer number of valence electrons (excluding the core electrons). For example, for a neutral C atom, $n = 4$. The quantity n_a in Eq. (2.16) is, in fact, the Mulliken charge [136]. An alternative is the Löwdin charge [137],

$$n_a = 2\sum_{b,b'}\sum_{i,j,j'}\int\frac{dE}{2\pi}\,\mathrm{Im}\left\{S^{1/2}_{i,a;j,b}G^<_{j,b;j',b'}(E)S^{1/2}_{j',b';i,a}\right\} \tag{2.17}$$

The Löwdin charge requires calculating the full matrix $G^<_{j,b;j',b'}$. Banded approximations can be made for $S^{1/2}$, but even if $S^{1/2}$ is approximated as tri-block-diagonal, the second off-diagonal blocks of $G^<$ must be calculated. We will see below, that for the Mulliken charge of Eq. (2.16), only the tri-block-diagonal elements of $G^<$ are required which makes the calculation amenable to the RGF algorithm.

To understand what Eq. (2.16) means in terms of the RGF algorithm, we re-write it using layer indices L,

$$n_{a,L} = 2\sum_{b,L'}\int\frac{dE}{2\pi}\,\mathrm{Im}\ \mathrm{tr}\left\{\mathbf{G}^<_{a,L;b,L'}(E)\mathbf{S}_{b,L';a,L}\right\} \tag{2.18}$$

Again the bold font indicates that $\mathbf{G}^<$ and $\mathbf{S}$ are matrices whose size is determined by the number of orbitals associated with atom a in layer L and with atom b in layer L'. The trace is over all the orbitals of atom a in layer L. Since $\mathbf{S}$ is block tri-diagonal, we are required to calculate the diagonal blocks and first off-diagonal blocks of $\mathbf{G}^<$. In other words, the calculation of $n_{a,L}$ requires the calculation of $\mathbf{G}^<_{L,L}$ and $\mathbf{G}^<_{L,L\pm1}$.

In the absence of incoherent scattering, the expression for the electron number in layer L, Eq. (2.18), can be written as

$$\mathbf{n}_L = 2\int\frac{dE}{2\pi}\mathrm{Re}\left\{\sum_{L'}\underbrace{\left[\left(\mathbf{G}^R_{L,1}\mathbf{\Gamma}_{1,1}\mathbf{G}^{R\dagger}_{L',1}\right)f^L + \left(\mathbf{G}_{L,N}\mathbf{\Gamma}_{N,N}\mathbf{G}^{R\dagger}_{L',N}\right)f^R\right]}_{-iG^<_{L,L'}(E)}\mathbf{S}_{L',L}\right\}. \tag{2.19}$$

To not overload the subscripts in Eq. (2.19), we have kept only the layer indices since those are our main focus. Eq. (2.19) shows that we need the first and last block columns of the retarded Green function for the electron density calculation.

We can write Eq. (2.19) in another form which only requires the left *or* right connected spectral function and the diagonal plus first off-diagonal blocks of the Green function. Defining the left and right connected spectral functions as $\mathbf{A}^{\mathcal{L}}_{L,L'} = \mathbf{G}^{R}_{L,1}\mathbf{\Gamma}_{1,1}\mathbf{G}^{R\dagger}_{L',1}$ and $\mathbf{A}^{\mathcal{R}}_{L,L'} = \mathbf{G}^{R}_{L,N}\mathbf{\Gamma}_{N,N}\mathbf{G}^{R\dagger}_{L',N}$ and using the fact that the full spectral function is the sum of the left and right spectral functions, Eq. (2.19) can be written as

$$\mathbf{n}_L = 2\int \frac{dE}{2\pi}\left\{\sum_{L'}\left[\underbrace{\mathbf{G}^{R}_{L,1}\mathbf{\Gamma}_{1,1}\mathbf{G}^{R\dagger}_{L',1}}_{\mathbf{A}^{\mathcal{L}}_{L,L'}(E)}\left(f^L - f^R\right) + \mathbf{A}_{L,L'}f^R\right]\mathbf{S}_{L',L}\right\} \tag{2.20}$$

where $\mathbf{A} = \mathbf{A}^{\mathcal{L}} + \mathbf{A}^{\mathcal{R}}$. To obtain the electron number for a specific shell on a specific atom, we simply trace $\mathbf{n}_L$ over the orbitals of that shell on that atom.

We can express the left and right terms in Eq. (2.20) as a sum of a non-equilibrium and an equilibrium charge contribution ($n_L = n_L^{neq} + n_L^{eq}$). We separate Eq. (2.20) by expressing the full spectral function as $\mathbf{A}_{L,L'} = -2\mathrm{Im}[\mathbf{G}_{\mathrm{L,L'}}]$ giving us

$$\mathbf{n}^{eq}_L = -2Im\left[\int \frac{dE}{2\pi}\left\{\sum_{L'}\left[\mathbf{G}_{L,L'}f^R\right]\mathbf{S}_{L',L}\right\}\right] \tag{2.21}$$

and

$$\mathbf{n}^{neq}_L = 2\int \frac{dE}{2\pi}\left\{\sum_{L'}\left[\mathbf{A}^{\mathcal{L}}_{L,L'}(E)\left(f^L - f^R\right)\right]\mathbf{S}_{L',L}\right\} \tag{2.22}$$

The equilibrium charge, Eq. (2.21). is calculated in Chapter 6 for the image potential.

The integral of Eq. (2.21) is performed using a well known complex contour integral approach [25, 138, 139]. The integral begins below the energy of the bottom valence band, follows a semi-circular trajectory in the upper half of the complex plane with a maximum imaginary component of the energy of 1 eV, and finishes

$10k_BT$ above the Fermi energy. At the Fermi energy, the contour passes below the lowest Fermi pole with an imaginary component of 10 meV such that there are no poles contained within the contour. The temperature is 300K for this calculation. Denoting the energy points on the complex contour as $E = z = x + iy$, points are chosen such that the points on the left part of the contour with increasing y are aligned with the points on the right part of the contour with decreasing y. This ensures that the sum of the discrete differentials, $\sum_j \Delta z_j$, along the line integral is real. The integral is performed using Simpson's rule. For the image-potential calculations presented here, we used a fixed set of 25 points for the semi-circle and 15 fixed points $\pm 10k_BT$ from the Fermi energy. The energy points are adaptively distributed for optimum load balancing over multiple processors (MPI-based).

The equilibrium charge density requires the exact diagonal, first column, and first off-diagonal blocks of $\mathbf{G}^R$. These elements are calculated with the recursive Green function (RGF) algorithm [134]. First we calculate the left and right connected Green functions using

$$\mathbf{g}^{\lhd}_{L,L} = \left[E\mathbf{S}_{L,L} - \mathbf{H}_{L,L} - \mathbf{U}_{L,L} - \tilde{\mathbf{t}}_{L,L-1}\mathbf{g}^{\lhd}_{L-1,L-1}\tilde{\mathbf{t}}_{L-1,L}\right]^{-1} \tag{2.23}$$

and

$$\mathbf{g}^{\rhd}_{L,L} = \left[E\mathbf{S}_{L,L} - \mathbf{H}_{L,L} - \mathbf{U}_{L,L} - \tilde{\mathbf{t}}_{L,L+1}\mathbf{g}^{\rhd}_{L+1,L+1}\tilde{\mathbf{t}}_{L+1,L}\right]^{-1}. \tag{2.24}$$

The superscript $\lhd$ ($\rhd$) indicates that the Green function takes into account everything to the left (right) with coupling to the right (left) set to zero, i.e. $\mathbf{g}^{\lhd}_{L,L}$ is the surface Green function at layer L for the semi-infinite region consisting of layers $\{-\infty, \cdots, L\}$. All Green functions in Eqs. (2.23) and (2.24) are retarded Green functions. Eqs. (2.23) and (2.24) begin with the surface Green functions of the left and right contacts, respectively. The off-block-diagonal coupling matrices are $\tilde{\mathbf{t}}_{L,L'} \doteq \mathbf{t}_{L,L'} - E\mathbf{S}_{L,L'}$.

Next, the exact diagonal blocks of $\mathbf{G}^R$ are calculated from

$$\mathbf{G}_{L,L} = \left[E\mathbf{S}_{L,L} - \mathbf{H}_{L,L} - \mathbf{U}_{L,L} - \tilde{\mathbf{t}}_{L,L-1}\mathbf{g}^{\triangleleft}_{L-1,L-1}\tilde{\mathbf{t}}_{L-1,L} - \tilde{\mathbf{t}}_{L,L+1}\mathbf{g}^{\triangleright}_{L+1,L+1}\tilde{\mathbf{t}}_{L+1,L}\right]^{-1}. \tag{2.25}$$

After each block $\mathbf{G}_{L,L}$ is calculated, it is stored, and $\mathbf{g}^{\triangleleft}_{L-1,L-1}$ is discarded. The off-diagonal blocks of G^R are calculated next from

$$\begin{aligned} \mathbf{G}_{L,L+1} &= \mathbf{G}_{L,L}\tilde{\mathbf{t}}_{L,L+1}\mathbf{g}^{\triangleright}_{L+1,L+1} \\ \mathbf{G}_{L,L-1} &= \mathbf{g}^{\triangleright}_{L,L}\tilde{\mathbf{t}}_{L,L-1}\mathbf{G}_{L-1,L-1} \end{aligned} \tag{2.26}$$

Finally, the first block column of G^R is calculated using

$$\mathbf{G}_{L,1} = \mathbf{g}^{\triangleright}_{L,L}\tilde{\mathbf{t}}_{L,L-1}\mathbf{G}_{L-1,1}. \tag{2.27}$$

which is initiated with $\mathbf{G}_{1,1}$.

The first block column $\mathbf{G}_{L,1}$ and the diagonal blocks $\mathbf{G}_{L,L}$ are then used in Eq. (2.20) to obtain the electron number. This electron number from Eq. (2.20) replaces Eq. (21) of Ref. [37]. The calculation of the resulting Hartree and exchange-correlation potentials is left unchanged in the code and is described in Ref. [37].

Chapter 3

FIREBALL-NEGF Verification

Verification using the FIREBALL-NEGF program is presented in this chapter. First an evaluation of FIREBALL's band-structure calculations modeling silicon (Si) and germanium (Ge) is presented. Next a comprehensive study is done comparing FIREBALL to a semi-empirical tight-binding approach modeling CNTs [4].

3.1 Silicon and Germanium Verification

Before calculating charge transport for CNT-molecular structures, an evaluation of the modeling capabilities within FIREBALL was done using silicon and germanium as it pertained to nanowires.

FIREBALL band structure calculations of silicon were first compared to a $sp^3d^5s^*$ empirical tight-binding model [9] using the FIREBALL default sp^3 basis and LDA exchange correlation method. The FIREBALL valence bands in figure (3.1) are lower due to the absence of spin. A study of the effective masses was compared and is seen in table (3.1). The empirical tight-binding model gives a conduction band minimum of 1.13 eV while FIREBALL gives a conduction band minimum of 1.55 eV. Using

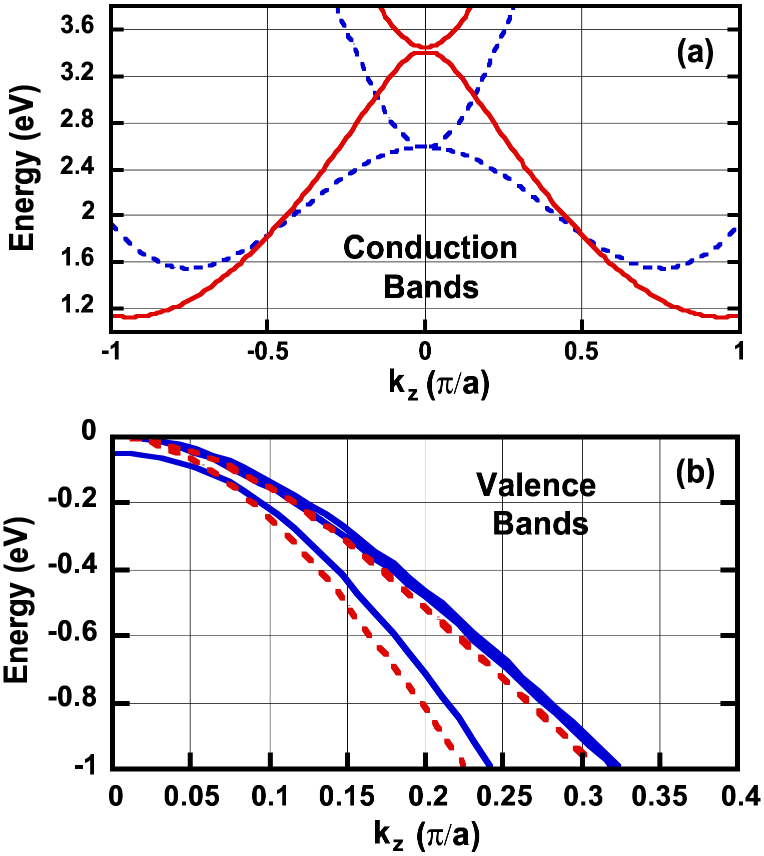

Figure 3.1: Band-structure comparison of bulk silicon using $sp^3d^5s^*$ empirical tight binding model (solid lines) and *ab initio* density functional theory (DFT) with localized density approximation (LDA) exchange correlation method (dashed lines)

the GGA exchange-correlation, FIREBALL gave a lower conduction band minimum at 1.41 eV. The slightly excited wavefunction orbitals used in FIREBALL somewhat offset the overestimation inherent of DFT models. Table (3.2) lists a comparison of the Si band energies found using both models.

The E-k plot for germanium is shown in Fig. (3.2) using the GGA exchange correlation method and same basis set. The GGA exchange correlation was used since LDA approximates a zero band-gap. FIREBALL places the conduction band minimum at 0.73 eV for the L point (111 direction) with a band-gap of 0.31 eV at

Table 3.1: Comparison of Si effective masses using $sp^3d^5s^*$ empirical tight binding model (Boykin, [9]) and *ab initio* density functional theory (DFT) with localized density approximation (LDA) exchange correlation method (FIREBALL).

Effective mass	FIREBALL	Boykin ($sp^3d^5s^*$)
m^*_{el}	0.7363	0.891
m^*_{et}	0.3430	0.201
m^*_{so}	-0.2933	-0.246
$m^*_{hh[100]}$	-0.2348	-0.276
$m^*_{lh[100]}$	-0.1456	-0.214
$m^*_{hh[110]}$	-0.4985	-0.581
$m^*_{lh[110]}$	-0.2908	-0.152
$m^*_{hh[111]}$	-0.5559	-0.734
$m^*_{lh[111]}$	-0.0870	-0.144

Table 3.2: Comparison of Si band energy points using $sp^3d^5s^*$ empirical tight binding model (Boykin, [9]) and *ab initio* density functional theory (DFT) with localized density approximation (LDA) exchange correlation method (FIREBALL).

Effective mass	FIREBALL	Boykin ($sp^3d^5s^*$)
E_{gap}	1.549	1.131
$E(L)_c$	2.266	2.29
$E(L)_v$	-1.01	-1.25
$E(X)_c$	2.5604	1.12
$E(X)_v$	-3.1883	-2.89
$E(\Gamma)_c$	2.5891	3.50
$E(\Gamma)_v$	0.00	0.00
$k(x)_{min}$	65.0%	81.3%
E_{cmin}	1.5523	1.131

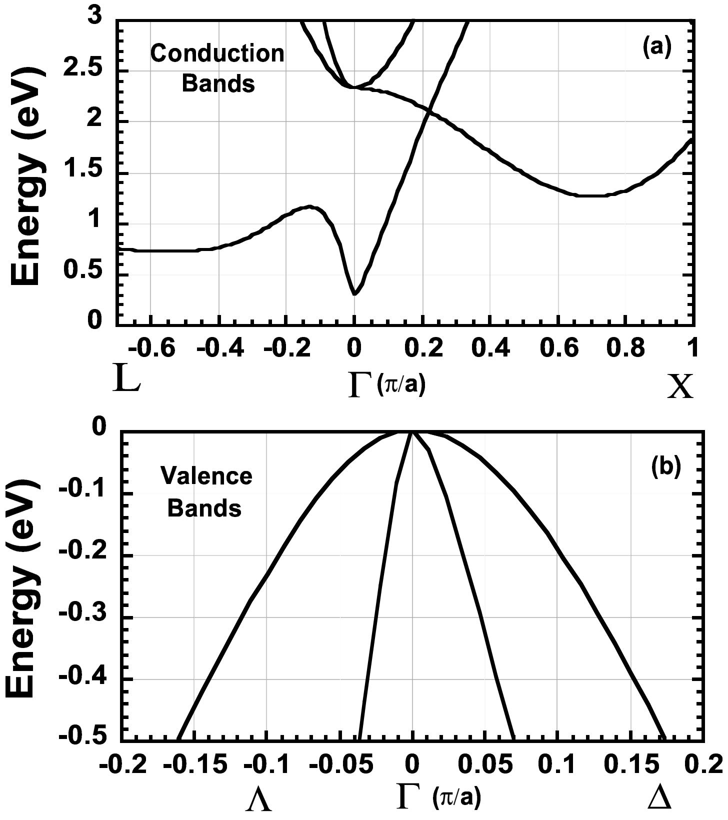

Figure 3.2: Conduction band-structure of bulk germanium using *ab initio* density functional theory (DFT) and generalized gradient approximation exchange correlation method.

the gamma point. The Ge band-structure closely resembles the "GW" band structure approximation found in Ref. [140].

3.2 CNT Verification

In this section, we compare predictions of the properties relevant to electronic device modeling of semiconducting (n,0) CNTs calculated from both DFT theory and an empirical, tight-binding, π-bond model [4]. Two important band-edge properties are the bandgap and the effective masses. For larger diameter CNTs, the empirical, tight-binding model is expected to predict the bandgap and band-edge effective masses with good accuracy since the empirical parameters have been chosen by fitting to those quantities. Therefore, for the larger diameter CNTs, we use the values of the bandgap and effective masses obtained from the π-bond model to assess the values obtained from the DFT model. For smaller diameter CNTs where the curvature becomes significant, the π-bond model breaks down.

Bandedge quantities alone are not sufficient for electronic device modeling. Since electronic devices are operated at biases on the order of a volt, accurate modeling of the higher energy states away from the bandedges is necessary for device modeling. The quantity that best characterizes the higher energy spectra for device simulations is the transmission coefficient. Therefore, we compare transmission coefficients calculated from the DFT and the empirical, tight-binding models.

Here a comparison is done examining the bandgaps, effective masses, and transmission spectra of semiconducting zigzag CNTs, ranging from $(5, 0)$ to $(35, 0)$ corresponding to diameters ranging from 0.39 nm to 2.8 nm. The bandgaps and effective masses are calculated, plotted, and compared for every non-metallic $(n, 0)$ CNT with $5 \leq n \leq 35$. Selected transmission coefficients are plotted and compared for $n = 10$, 20, 31, and 35.

3.2.1 Empirical π-bond model

For the empirical π-bond model, we use a nearest-neighbor model with matrix element $V_{pp\pi} = -2.77$ eV and $\epsilon_p = 0.0$ eV [141]. The NEGF algorithm is the same as that used with the FIREBALL matrix elements. The effective mass for both models is calculated from the 1-D dispersion using $1/m* = \frac{1}{\hbar^2}\partial^2 E/\partial k^2$. The energy band gap is determined from an $E - k$ calculation by reading the difference between the highest occupied band energy and the lowest unoccupied band energy at the Γ point.

3.2.2 CNT Results and Discussion

Figure 3.3(a) compares the calculated band gaps for $(n, 0)$ CNTs with $5 \leq n \leq 35$ leaving out the metallic CNTs with n values that are integer multiples of 3. The n values are shown on the bottom horizontal axis and the corresponding CNT diameters are shown on the top horizontal axis. On the plot itself, the data points indicate the n values for which calculations were performed. All other n values in that range correspond to metallic CNTs. At first glance, the bandgaps that result from the FIREBALL calculations closely track the bandgaps determined by the π-bond model for $n \geq 10$. CNTs in this size range are the ones that are most commonly synthesized, and they are the ones that are most important for electronic devices [84]. Below $n = 10$, the π-bond model breaks down due to the large curvature of the CNT. For the smallest CNT with $n = 5$, the FIREBALL calculations show zero bandgap. Upon closer inspection of Fig. 3.3(a), one notices a sawtooth shape to the plot of bandgap versus n for the DFT calculations. We observe that the bandgap resulting from the DFT calculations corresponds closely to the bandgap resulting from the π-bond model for $(n, 0)$ CNTs when $n = 3p + 1$ where p is an integer ≥ 3.

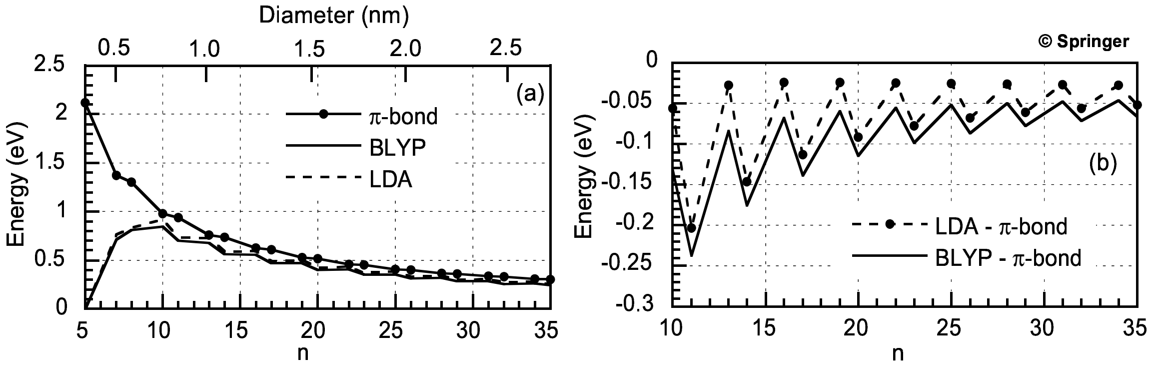

Figure 3.3: (a) $(n, 0)$ CNT band gaps as a function of n and diameter calculated from the π-bond model and DFT with LDA and BLYP functionals. (b) Difference between the band gap calculated from the DFT models and the π-bond model.

This is shown clearly in Fig. 3.3(b). which plot the differences between the bandgaps calculated from the LDA and BLYP functionals and those from the π-bond model for $n \geq 10$. For $n = 3p + 1 \geq 13$, the LDA model underestimates the bandgap by 24 - 28 meV. For these n values, the BLYP model underestimates the bandgap by 46 - 84 meV. For $n = 3p - 1$ with p an integer, the discrepancies between the bandgaps resulting from the DFT models and the π-bond model are larger. For values of $n = 3p - 1 \geq 14$, the LDA model underestimates the bandgap by 52 - 147 meV. For these n values, the BLYP model underestimates the bandgap by 66 - 176 meV.

Figs. 3.4 shows calculations and comparisons of the electron and hole effective masses. The plots of the left column show calculations and comparisons of the electron effective mass, and the plots of the right column show calculations and comparisons of the hole effective mass. In each row consisting of two plots, the scale and range of values is identical to facilitate easy comparisons between the values for electrons and holes. The calculated electron and hole effective masses (normalized to the bare electron mass) are plotted in Figs. 3.4(a) and (d), respectively, versus n for all semiconducting values in the range $7 \leq n \leq 35$. One immediately notices that all models result in very similar values of effective masses for both the electrons and holes. To discern the differences, a plot of the differences in mass values calculated from the DFT models and the pi-bond model is shown in Figs. 3.4(b) and (e) for electrons and holes, respectively. In other words, Figs. 3.4(b) and (e) show the normalized difference values $(m^*_{\mathrm{DFT}} - m^*_{\pi-\mathrm{bond}})/m_0$. Note that on the mass difference plots, (b) and (e), the n values range from 10 - 35 whereas on the mass plots, (a) and (d), the n values range from 7 - 35. The range of n is reduced on the difference plots to keep the plotted range of differences small. The difference plots show that the effective mass determined from the BLYP model tends to be larger than the effective mass

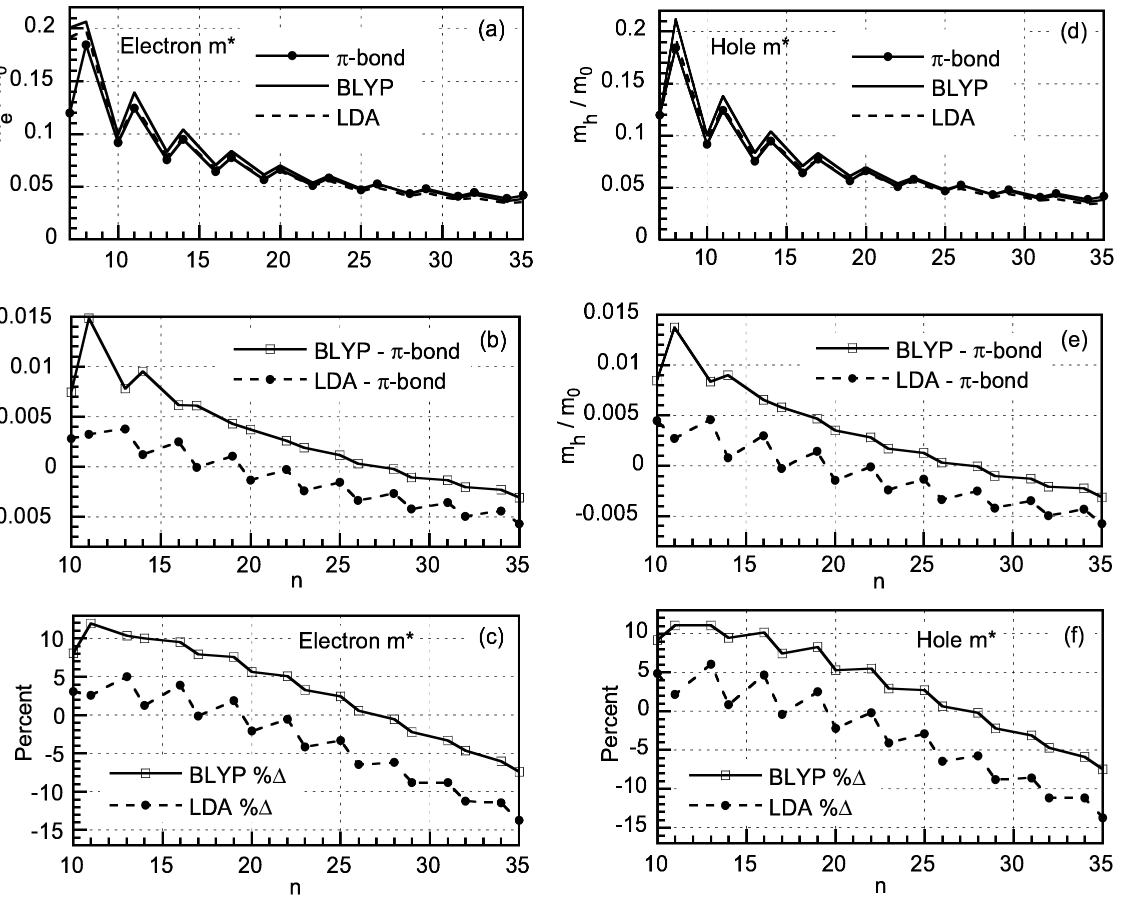

Figure 3.4: Electron, (a) - (c), and hole, (d) - (f), effective mass comparisons. Top: Normalized effective mass (m^*/m_0), calculated from the π-bond and DFT models. Middle: Difference between the effective mass calculated from the DFT models and the π-bond model $(m_{\mathrm{DFT}} - m_{\pi-\mathrm{bond}})/m_0$. Bottom: Percent difference, $100 * (m_{\mathrm{DFT}} - m_{\pi-\mathrm{bond}})/m_{\pi-\mathrm{bond}}$.

determined by the LDA model. Over the range of n values $14 \leq n \leq 35$, the mass determined by the BLYP model has a maximum difference from the mass determined from the LDA model of 0.008 at $n = 14$ and a minimum difference of 0.002 at $n = 34$. Also, the sawtooth peaks in the difference curves are out of phase with the sawtooth peaks in the mass curves above. The maximum differences occur at the minimums of the mass curves. Overall, the differences in the mass values predicted by the DFT models and the π-bond model are relatively small. To quantify the differences, the percent differences, $100 * (m_{\mathrm{DFT}} - m_{\pi-\mathrm{bond}})/m_{\pi-\mathrm{bond}}$, are plotted in (c) and (f). Over a wide range of the most useful n values for device applications, $17 \leq n \leq 29$, the values for the effective masses from the DFT models fall to within +8% to −9% of the values from the π-bond model.

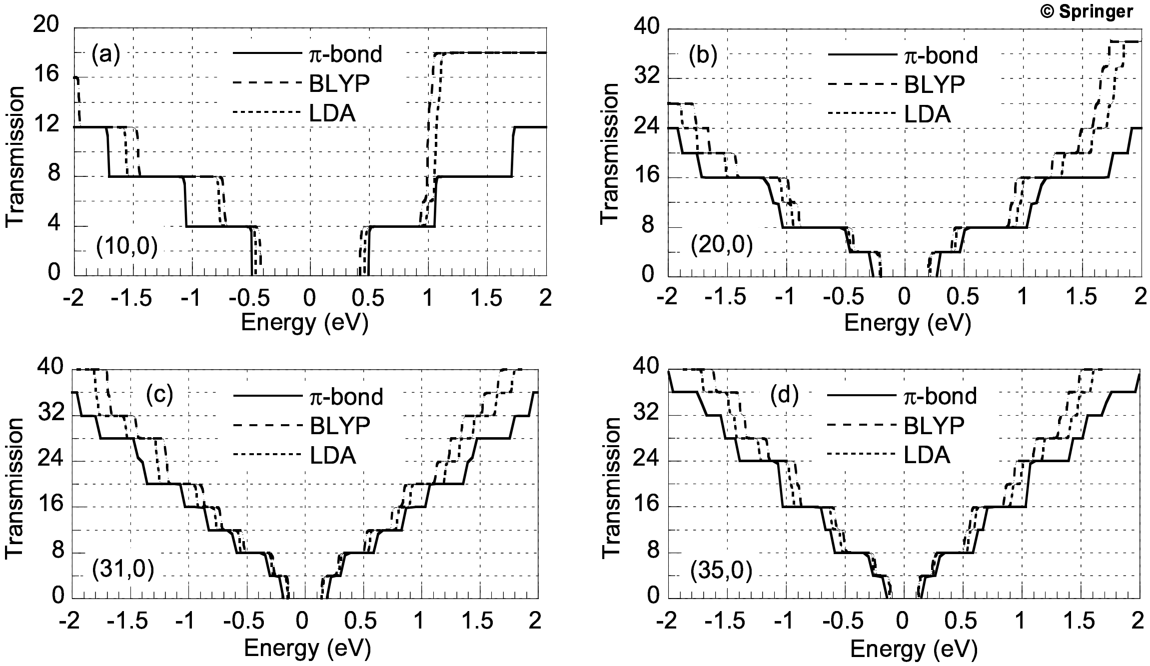

Figure 3.5: Transmission calculated from π-bond and DFT models for $(n, 0)$ CNTs with n values of (a) 10, (b) 20, (c) 31, and (d) 35.

So far, this verification study has considered bandedge properties of bandgaps and effective masses. As noted above, the higher energy electronic spectra is also important for electronic device modeling, and the best way to characterize it is to calculate the transmission coefficients. Figure 3.5 shows the transmission spectra for $(10, 0), (20, 0), (31, 0)$ and $(35, 0)$ CNTs calculated using DFT/BLYP, DFT/LDA, and the empirical, π-bond model. In all cases, the energy axis of the transmission curves has been shifted such that the center of the bandgap lies at 0 eV. The energy region in Fig. 3.5 for which the transmission is zero is the band gap for the CNTs.

For the 2 largest CNTs, $n = 31$ and 35, the transmission resulting from the DFT and π-bond models all have similar, symmetric forms. There is some compression of the energy scale for the transmission coefficients calculated from the DFT models compared to the transmission coefficient calculated from the π-bond model. The energy separation between higher modes is smaller in the DFT models then in the π-bond model.

For the smallest CNT, $n = 10$, there is a noticeable, qualitative difference between the transmission calculated from the DFT models and the π-bond model. The transmission resulting from the π-bond model is always symmetric around the center of the bandgap. For the DFT models, the transmission is noticeably asymmetric. Approximately 0.5 eV above the conduction band edge, the DFT models predict 3 bands closely spaced and 2 bands doubly degenerate. These 7 bands, multiplied by 2 for spin, give rise to the large step of 14 in the transmission coefficient 0.5 eV above the conduction band edge in the transmission coefficient of the $(10, 0)$ CNT. This large increase in the transmission and density of states 0.5 eV in the conduction band is significant for device modeling. A similar large step is also observed in a transmission calculation based on the SIESTA code for a $(7, 0)$ CNT [142]. A similar large increase in the transmission also occurs in the (20,0) CNT at 1.3 eV above the conduction band edge.

The differences in the (10,0) valence band transmission resulting from the DFT and π-bond models, while not as dramatic as those in the conduction band, are still significant from a device modeling perspective. The 0.5 eV gap between the valence band edge and the next lower pair of bands found from the π-bond model is reduced to approximately 0.3 eV in the DFT models. These energies lie within the applied voltage window, (V_{DD}), of any of the most optimistically scaled CNT field effect transistors, and will, thus, affect the physics of the carrier transport. While the main focus is on assessing the validity of the DFT models for device modeling, these results also provide an assessment of the π-bond model and show that the π-bond model should be used with care and scepticism for (10,0) CNTs.

3.3 Summary

The goal of this chapter is to assess the validity of the DFT models implemented by FIREBALL for Si, Ge and CNT electronic device modeling. Our approach is to compare the electronic properties resulting from the DFT models with those resulting from the $sp^3d^5s^*$ empirical tight-binding model and π-bond model since the parameters have been empirically chosen to give a good fit to the bandgap and effective mass for Si, Ge and CNTs. Since this dissertation is primarily interested in CNT-molecular electronic device modeling, we have compared the bandgaps, effective masses, and transmission coefficients of zigzag $(n, 0)$ CNTs calculated from the empirical π-bond model, DFT/LDA, and DFT/BLYP models [4].

For CNT values of $(n, 0)$ in the range $17 \leq n \leq 29$, the calculated effective masses from the DFT models are within ±9% of those calculated from the π-bond model. For $n \geq 10$, the difference between the bandgap calculated from the π-bond model and the bandgaps calculated from the DFT models oscillates as a function of n. The differences are smallest for $n = 3p + 1$ where p is an integer, and the differences are largest for $n = 3p - 1$. For $n = 3p + 1 \geq 13$, the LDA model underestimates the bandgap by 24 - 58 meV and the BLYP model underestimates the bandgap by 46 - 84 meV. For $n = 3p - 1 \geq 14$, the LDA model underestimates the bandgap by 52 - 147 meV and the BLYP model underestimates the bandgap by 66 - 176 meV. Overall, in the important range of n values most relevant for CNT devices, $17 \leq n \leq 29$, the bandgaps, effective masses, and transmission coefficients calculated from the DFT models implemented by FIREBALL are sufficiently accurate for electronic device simulations.

The CNT simulations also quantify what is meant by ‘not too small’ when applying the π-bond model. For $n = 10$, the bandedge properties resulting from the π-bond and DFT models agree to within 10%, however, the π-bond model quickly becomes inaccurate away from the bandedges. The transmission from the higher energy modes resulting from the π-bond model has differences with those resulting from the DFT models which are significant for device modeling. For $n \leq 8$, the π-bond model is completely inaccurate.

Chapter 4

CNT-Molecular Resonant Tunneling Diode

Carbon nanotube (CNT) molecular resonant tunnel diodes (RTDs) are proposed to complement bio-assembled CNT field effect transistors (CNTFETs). Resonant tunneling operation is demonstrated both theoretically and experimentally for CNT-L-R-L-CNT systems in which L is the amide linker and R is either C_2H_4 or single strand DNA. The modeling methology discussed in Chapter 2, section 2.3 is used to calculate transmission through a CNT-Amide-Pseudopeptide-Amide-CNT [1,2] system and a CNT-Amide-DNA-Amide-CNT structure [3,5].

4.1 Introduction

In bio-assembly applications, reviewed in Chapter 1, a popular and heavily researched electronic FET device is proposed using CNTs. CNTs can be connected and assembled by DNA or peptide nucleic acid (PNA) linkers [50,58–62]. The biological linkers are used for their mechanical properties and their binding specificity. From an engineering point of view, the linkers are considered to be insulating. If electron or hole transport between the linked CNTs is required, the linkers are metallized [79].

Molecular linkers can provide more than mechanical and binding functionality. They can also provide electrical functionality. Well known examples of molecules providing electrical functionality are 2'-amino-4-ethynylphenyl-4'-ethyny-lphenyl-5'-nitro-1-benzenethiolate [95] and rotaxane [14]. Applying a voltage bias across these molecules causes a conformational change which results in bistability of the molecular conductance.

Even if there is no bistability in the molecule itself, coupling of the molecule to the leads gives rise to resonant levels [143–145]. With *metal* leads, the crossing of these levels with the metal Fermi level can give rise to steps in the current, and it has been proposed to use this effect to create logic circuits [146]. With one or more *semiconducting* leads, the crossing of these levels with the conduction or valence band edge can give rise to negative differential resistance and the current-voltage (I-V) characteristic of a resonant tunnel diode [33, 110, 111].

As discussed in Chapter 1, the semiconducting/metallic properties of CNT contacts provides the possibility for molecular-based resonant tunneling applications. In a CNT-L-R-L-CNT system, where L is the linker molecule and R is the molecule, no special bistable properties of the molecule are required. Conducting conjugated molecules can be used and should exhibit longer reliability than bistable molecules [147] where greater than 10^{12} logical operations are expected for a digital device. The electrical functionality is provided not by the intrinsic bistable properties of the molecule, but by the crossing of resonant levels with the band edges of the CNT leads.

The semiconducting (n,0) CNT leads considered here are also different from semiconducting nanowire (NW) leads. NWs would be suitable to contact molecules, however the end-specific functionalization process for semiconducting NWs is not yet developed. Furthermore, for semiconducting NWs, the motivation to build RTDs using resonant molecular levels would appear to be less strong since one can grow heterostructure all-semiconductor NW RTDs [148, 149].

This chapter covers transport properties of two semiconductor CNT-molecule-CNT structures and the discovery of a resonant tunneling device compatible with bio-assembled CNTFETs.

4.2 CNT-Pseudopeptide-CNT

4.2.1 Structure

The first system considered is a pseudopeptide molecule bridging two semiconducting CNT leads. The model schematic (A) and non-periodic relaxed structure (B) are shown in Fig. 4.1. The structure is composed of two (10,0) semiconducting CNTs, passivated with H bridged by amide linkers (L) via a -C_2H_4- (R) molecule. The molecular linking structure resembles the peptide backbone of PNA which is of interest in bio-assembly [61,62]. The structure (B) is optimized using the MMX force-field method built-in the PCMODEL software [150]. A section of the optimized structure is shown in Fig. 4.2, with the bond-lengths, bond angles and dihedral angles. The two benzene rings represent the portion of the two CNTs to which the pseudopeptide is attached.

4.2.2 Results

Fig. 4.3 (A) shows a plot of the CNT-Pseudopeptide-CNT transmission (solid line) overlaid on a plot of the bare CNT transmission (dashed line). The band-gap of the bare CNT begins at -6.5 eV and ends close to -5.5 eV. The peak transmission,

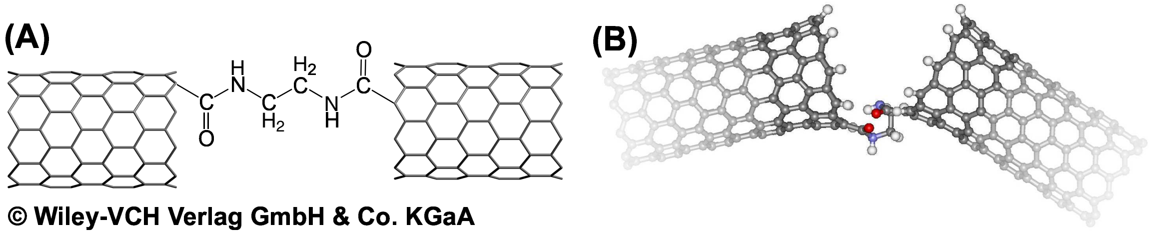

© Wiley-VCH Verlag GmbH & Co. KGaA

Figure 4.1: (A) Schematic of the CNT-pseudopeptide-CNT. (B) Relaxed structure with H passivation of the CNT end. The CNTs are (10,0).

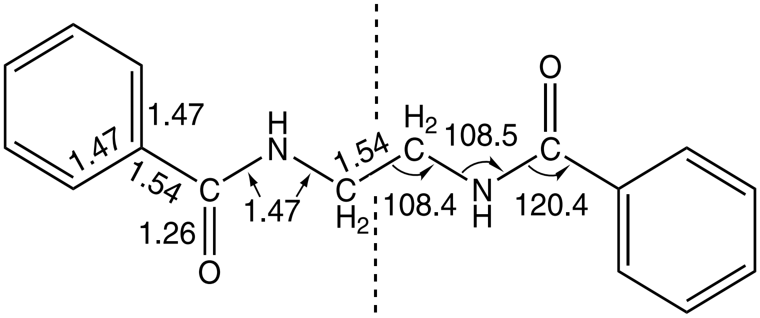

Figure 4.2: Geometrical parameters for a section of the CNT-L-R-L-CNT structure. The benzene rings represent the portion of the two CNTs to which the pseudopeptide is attached. The bond-lengths are represented in angstroms (Å) and the angles in degrees. Taking advantage of the symmetrical structure, the bond lengths are shown on left hand side of the dotted vertical line while the angles are shown on the right hand side to avoid crowding. Dihedral angles: $C_{CNT} - C_{CARBONYL} - N - C_{METHYLENE} = 145.0^o$ and $C_{CARBONYL} - N - C_{METHYLENE} - C_{METHYLENE} = 62.0^o$

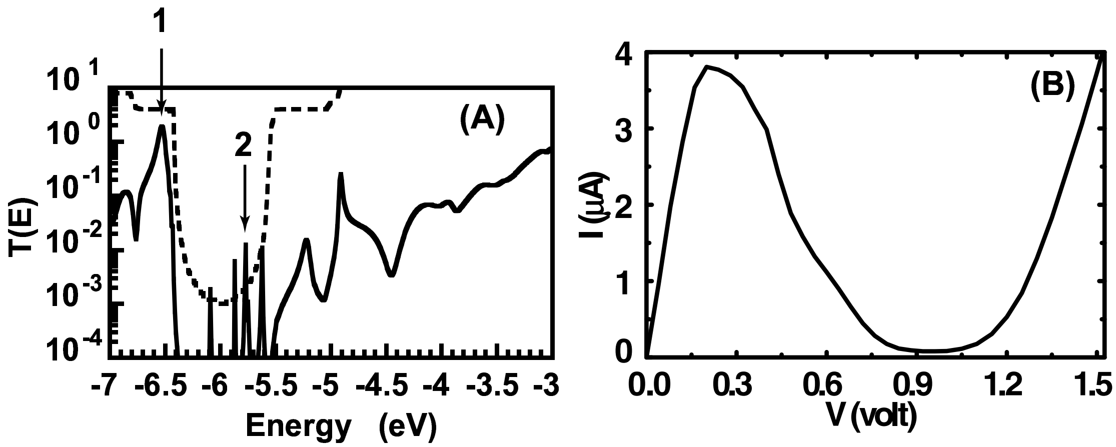

Figure 4.3: (A) Transmission of CNT-pseudopeptide-CNT (solid line) superimposed on the transmission of an ideal (10,0) CNT (dashed line). (B) I-V response of the CNT-pseudopeptide-CNT structure.

seen at the edge of the valence band at approximately -6.56 eV (point 1), indicates good hole transfer through the CNT-Psuedopeptide interfaces and structure. Electron transmission from the conduction bands of the CNTs is strongly suppressed.

A surface contour plot of the spectral function at point 1 of Fig. 4.3 (A) is shown in Fig. 4.4(A). Even though this energy occurs within the valence band of the CNT, the wavefunction is strongly peaked on the O and N atoms of the pseudopeptide. The electron cloud of the CNT valence band can also be seen around the CNT leads indicating good coupling to the leads.

The transmission peaks observed in the CNT band-gap is the result of resonant tunneling from the CNT end through the interface / peptide states. The contour plot of the spectral function at point 2 of Fig. 4.3 (A), shown in Fig. 4.4(B), better illustrates this tunneling behavior. The peak wavefunection contours, marked in red, represent the hyrbidization of (1) weak coupling of the molecular pseudopeptide resonances to each CNT and (2) the C-H truncated surface of the CNTs. The surface states of finite length zigzag CNTs with and without hydrogen passivation have been

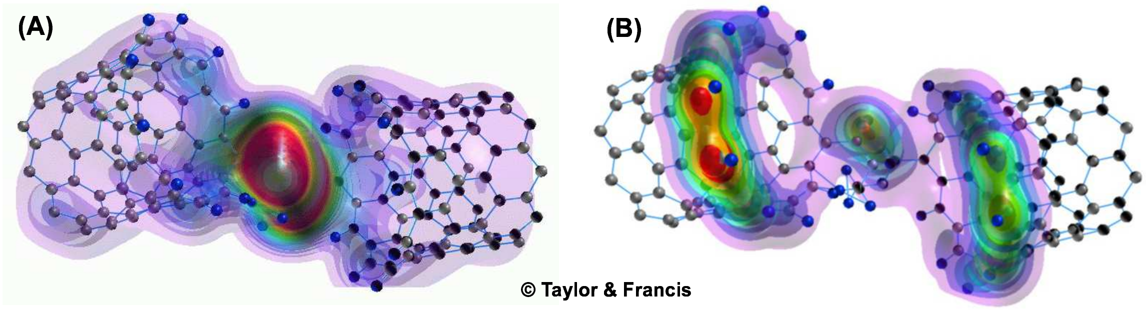

Figure 4.4: (A) Point 1: Contour surface plot of the spectral function at -6.53 eV near the valence band edge. (B) Point 2: Contour surface plot of the spectral function at -5.87 eV inside the CNT bandgap.

observed by others [117, 151]. There is no wavefunction cloud further back in the CNT leads since this energy window lies within the bandgap of the CNTs.

Figure 4.3 (A) and the spectral response of Fig. 4.4(A) illustrates the properties required for a CNT-L-R-L-CNT structure to perform as an RTD. A resonant level lies close to the band edge and outside of the CNT bandgap. The closeness of the bandedge is also good for low voltage operation. The farther the resonant level lies away from a bandedge, the larger the applied voltage must be to pull the resonant level into the bandgap of the source lead. Since the transmission and spectral wavefunction indicate a low voltage NDF response from the CNT-L-R-L-CNT system, a non self-consistent I-V calculation is performed.

To calculate the I-V of Fig. 4.3 (B), the CNT leads are assumed to be p-type with zero-Schottky barrier Pd contacts [80]. The Fermi level of the CNTs is aligned with thee valence band edges. An applied external potential V_a is added to the equilibrium Hamiltonian, and the matrix elements are calculated. The external potential consists of a linear potential drop between the two CNT leads. The value of V_a at the position $\mathbf{r}_i$ of each atom of the pseudopeptide is linearly interpolated according to the atom's distance from the C atom that bonds to the amide at the source and drain CNT.

The matrix elements of V_a are calculated as $\langle i,\alpha|V_a|j,\beta\rangle = S_{\alpha_i,\beta_j}\left[V_a(\mathbf{r}_i)+V_a(\mathbf{r}_j)\right]/2$ where indices i and j label the atoms, indices α and β label the basis orbitals, and S_{α_i,β_j} is the overlap matrix $\langle i,\alpha|j,\beta\rangle$. This approach in which the matrix elements have the same form as in an extended Huckel model has been used by others [24]. The approach captures the Stark effect, but not nonequilibrium self consistency.

The calculated I-V response of the CNT-L-R-L-CNT structure is shown in Fig. 4.3 (B) which displays the classic negative differential characteristics of an RTD. The I-V has a peak magnitude of 4 μA which is well matched to the current magnitudes provided by a (10,0) CNTFET [152].

4.2.3 Discussion

In molecules with internal rotational or translational degrees of freedom, charging can cause conformational changes affecting the charge transfer [14,95,153]. However, like the molecules studied in Ref. [111], the pseudopeptide is relatively rigid and large conformational changes are not expected. Single electron charging effects are possible, but the full-width, half maximum of the main resonance is 50 meV, so single electron effects should not be important. Therefore, as described in [111], the predominant effect of non-equilibrium self consistency will be to modify the voltage axis in Fig. 4.3B shifting the peak out to higher voltages.

Given the electronic molecular-based functionality, a mixed RTD / FET circuit application can be implemented where the resonant level should be able to carry current magnitudes matched to the current magnitudes provided by the CNTFETs. The addition of CNT RTDs to the device menu gives flexibility to the possible circuit designs. One can draw on the substantial body of work on mixed FET-RTD circuit design [154,155]. The addition of RTDs to FET circuits increases functional density

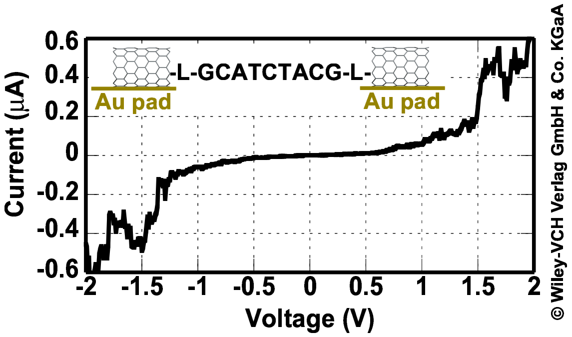

Figure 4.5: Measured current voltage response of a Au-CNT-ssDNA-CNT-Au structure [3]. Inset: Schematic of the structure.

allowing the same circuit functionality with fewer devices, less area, and faster speed [156].

4.3 Experimental CNT-DNA-CNT

4.3.1 Structure

The second system considered in this chapter is an experimentally built, characterized, and electrically measured CNT-L-R-L-CNT system [3]. In this system R consists of a single strand DNA (ss-DNA), and L is again the amide linker. The base sequence of the symmetric ss-DNA is (GCATCTACG).

The functionalization of the CNT followed the procedure described in Chapter 1 of oxidizing the CNTs with nitric acid and coupling the ss-DNA to the CNTs with an EDC reaction. Raman and FT-IR spectroscopy confirmed the presence of the DNA after synthesis. The measured current voltage response is shown in Fig. 4.5. There are two immediately noticable features in Fig. 4.5. (i) There is an approximately 2 V plateau region centered around 0 volts. (ii) After the turn-on of the current at approximately ±1V, NDR occurs.

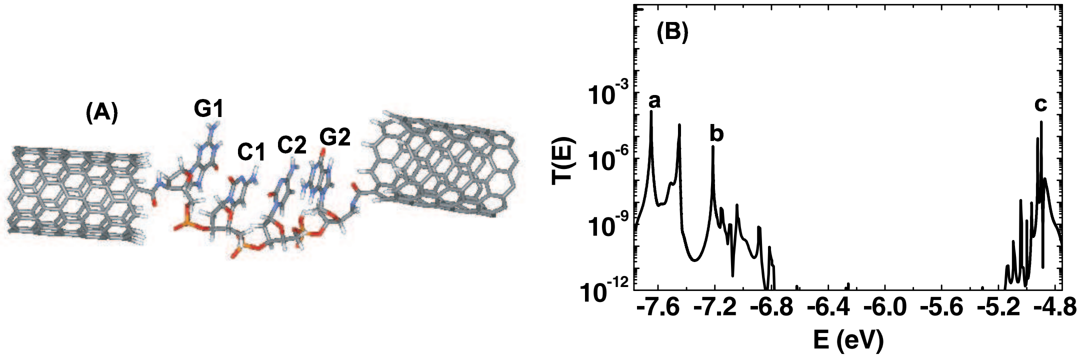

© Wiley-VCH Verlag GmbH & Co. KGaA

Figure 4.6: (A) Symmetric ss-DNA connected to two semi-infinite (10,0) CNT leads with amide linkers. Base sequence as shown. (B) Transmission of CNT-ssDNA-CNT (solid) superimposed on the transmission of an ideal (10,0) CNT (dashed).

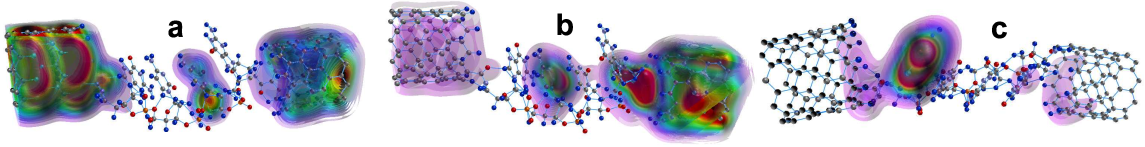

© American Scientific Publishers

Figure 4.7: Three dimensional spectral function countour plots at energies corresponding to the labeled transmission peaks in Fig. 4.6B. The resonant energies and positions are (a) E=-7.647eV localized on C2. (b) E=-7.212eV localized on C1 and right amide. (c) E=-4.897eV localized on G1.

For theoretical comparison, a smaller version of a symmetric CNT-L-ssDNA-L-CNT structure shown in Fig. 4.6 (A) is used. The phosphate groups on the backbone of the DNA are passivated with H [40] and the open ends of the CNTs at the interface are also passivated with H. Compoents of the non-periodic structure are optimized depending on the size, using the Hartree-Fock method or DFT methods such as BLYP [130] or B3LYP [157] implemented in the quantum chemistry code Gaussian03 [124]. Optimizations are done using the MMX force-field method in PCMODEL software [150] for the DNA segment of the structure.

4.3.2 Results

The calculated transmission versus energy of the structure is shown in Fig. 4.6 (B). There are 3 major resonances in the transmission in the valence band and a double peak in the conduction. The major peaks both lie about 0.5eV-1eV above and below the conduction and valence band edges. This spacing is consistent with the experimentally observed plateau around zero bias.

To understand the origin of the transmission resonances, three-dimensional contour plots of the covariant spectral function are plotted and shown in Fig. 4.7 (a-c) for the three labeled transmission peaks (a-c) in plot Fig. 4.6 (B). For transmission peak (a), the spectral function is peaked on the second cytosine (C2) shown in Fig. 4.7 (a). Transmission peak b results from a resonance on the first cytosine and the right amide shown in Fig. 4.7 (b). The transmission peak in between peaks (a) and (b) results from a resonance on both amide linkers. In the conduction band at point (c), the spectral function is peaked on the first guanine base (G1) as shown in Fig. 4.7 (c). The spectral plots of the major resonances suggest that the base pair types influence the tunneling behavior between the CNT contacts and dictate the amount of applied bias needed to pull the resonant levels into the bandgap of the source lead.

To understand what possible values of current could pass through this structure, we analyze the highest resonance, which is shown in detail in Fig. 4.8. Using the standard form for the transmission through a resonance, $T(E) = \frac{\Gamma^2/4}{(E-\epsilon_{HOMO})^2+\Gamma^2/4}$, the value for the full-width at half maximum, $FWHM = \Gamma_L + \Gamma_R = \Gamma$, and the maximum of the transmission, $T_m = \frac{4\Gamma_L\Gamma_R}{(\Gamma_L+\Gamma_R)^2}$, we determine the individual values of G_L and G_R for this resonance, Substituting $\Gamma_R = \Gamma - \Gamma_L$ into the expression for T_m gives

$$\Gamma_L = \frac{\Gamma}{2}[1 \pm \sqrt{1 - T_m}] \tag{4.1}$$

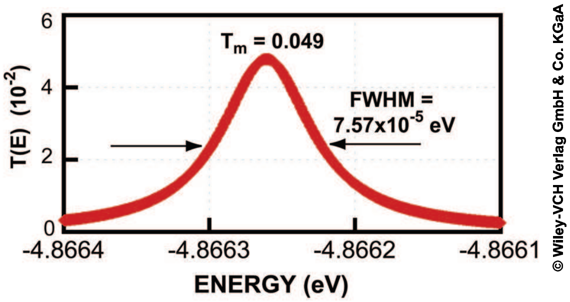

Figure 4.8: Detailed view of the highest resonance from Fig. 4.6B. All data points are plotted merging into a solid thick line indicating good resolution of the resonance.

Since $T_m << 1$,

$$\Gamma_L = \frac{\Gamma}{2}[1 \pm (1 - T_m/2)] \tag{4.2}$$

The resonant state for this resonance lies on the right guanine adjacent to the right SWNT. Therefore, we choose the minus sign in Eq. 4.2 giving $\Gamma_L = \Gamma\frac{T_m}{4}$ and $\Gamma_R = \Gamma(1 - \frac{T_m}{4})$. The maximum current that can be carried by this resonance is

$$I_m = \frac{2e}{\hbar}\int \frac{dE}{2\pi}T(E) = \frac{2e}{\hbar}\frac{\Gamma_L\Gamma_R}{\Gamma_L + \Gamma_R} = 2e\frac{T_m}{4}\frac{\Gamma}{\hbar} \tag{4.3}$$

Putting in the numbers from Fig. 4.8 in Eq. 4.3 results in the maximum current through the strongest resonance of 0.44 nA. This is coherent, resonant current tunneling through the 4-base ssDNA linker. For the level of current, we can estimate a maximum value assuming the current is limited by the tunneling from the right CNT onto the right guanine base. In this case, the maximum possible current through the resonant state shown in Fig. 4.8 is

$$I_m = \frac{2e}{\hbar}\Gamma = 36nA \tag{4.4}$$

4.3.3 Discussion

The experimental configuration is considerably more complex than the model system considered above. The ssDNA fragments make contact directly to metal on one side and a SWNT rope bundle that may contain between 10-100 SWNTs on the other. Each SWNT within the bundle is functionalized with $n > 1$ ss-DNA oligomers. These are acting in parallel giving a multiplication factor of (10-100)n over a system with one ss-DNA. Assuming n=2 and 20 CNTs in a bundle, we get a maximum possible current of 1.4 A. There is also a possible interaction between the ssDNA strands, which could further assist in the electron transfer process.

The two experimental sequences are considerably larger than the model system considered here. One sequence is symmetric consisting of 9 bases and the second sequence is random consisting of 24 bases. The plateau region around 0 volts in the experimental I-V curves is consistent with the distance between the resonant peaks and the band edges in the calculated transmission. If we take the on-current of the 9 base symmetric sequence as $0.4\mu A$ and divide by 20 (100), we get 20 (4) nA per SWNT. Taking n to be 2-4, we get 5-10 (1-2) nA per DNA strand. Intuitively, the current of a 24 base strand would be considerably less than the current through a 9 base strand and this is what we have observed with the I-V measurements.

4.4 Summary

In this chapter a proposed CNT-L-R-L-CNT molecular RTD is presented which is compatible with bio-assembly techniques and architectures to complement CNTFETs. Experimental and theoretical results using the CNT-L-R-L-CNT device structure demonstrate resonant tunneling behavior. The addition of RTDs to FET circuitry allows for greater functionality with fewer devices. The greatest advantages of this with respect to self-assembly are simplified circuit topology, lower power and higher speed.

Chapter 5

CNT-Molecular Geometry

A model carbon nanotube (CNT)-$(CH)_n$-CNT structure is studied to understand electron transport through an interface between two conjugated systems [6]. The conductance of the CNT-$(CH)_n$-CNT structures strongly depends on the bonding angle of the $(CH)_n$-CNT bond. The relationship of the conductance on the length of the $(CH)_n$ depends on the geometry of the $(CH)_n$ - CNT interface. In the coplanar geometry, the conductance decreases with the length of the $(CH)_n$. In the perpendicular geometry, the conductance increases with the length of the $(CH)_n$. In this chapter the modeling methology discussed in Chapter 2, section 2.3 is used, for calculating tranmission through several CNT-$(CH)_n$-CNT structures.

5.1 Introduction

One open question, discussed in Chapter 1, is how the chemistry and geometry of the CNT - molecule interface affects the electron transport and conductance. It is widely recognized that the interface plays a crucial role in metal - molecule junctions [21, 52, 101, 123]. Recent theoretical and experimental studies have shown that the

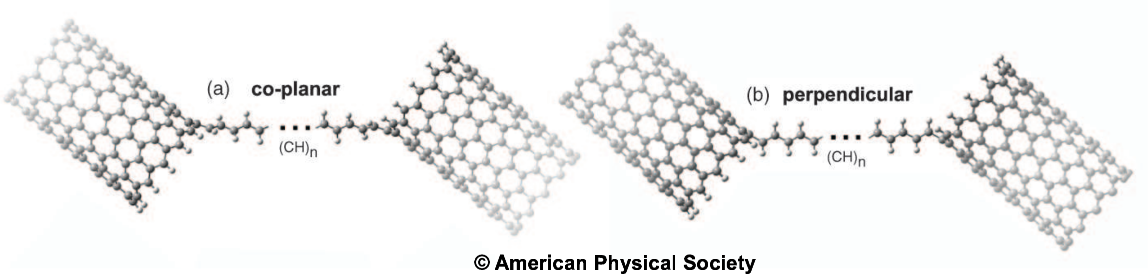

Figure 5.1: CNT-(CH)$_n$-CNT structures. (a) Perpendicular CNT-(CH)$_n$-CNT interface geometry. (b) Relaxed interface geometry which is relatively coplanar.

CNT-molecule interface chemistry and structure strongly affects molecular transport [103, 117, 158]. Here a model CNT - conjugated molecule - CNT system is used to analyze how the interface geometry affects the electron transmission and conductance for different molecule lengths [6].

The molecular contacts, in this case the CNTs, are a π-bond surface and, as such, they are both chemically and geometrically different from metal contacts or sp^3 semiconductor contacts. The linking chemistry between the CNTs and the molecule influences electron/hole transport between the CNT contacts and the molecule. The standard amide linking group [61, 62, 67, 77] is known to effect electron transport at the interface due to significant conjugation from the π-bond of the -C=O group with two lone pairs of electrons on the oxygen and a lone pair of electrons on the nitrogen [2, 5, 67, 117].

5.2 Structure

As a first step to understanding electron transport through an interface between a conjugated CNT lead and a conjugated molecule, we studied a model system consisting of metallic zigzag (12,0) CNT leads linked directly to a semi-conducting polymer, *trans*-polyacetylene (CH)$_n$, as seen in Fig. 5.1. The linking chemistry at the CNTpolyactylene interface is a C–C bond. This model system allows us to study electron transport through two pure π-bond systems without the added complexity of lone pairs at the interface.

To understand how the interface geometry affects transport, two variations of the CNT-$(CH)_n$-CNT system is considered. The first system, shown in Fig. 5.1(a), is relaxed. The $(CH)_n$ molecule is nearly co-planar with the tangential plane of the CNT at the point of contact. The relaxation of the CNT-$(CH)_n$-CNT system is performed with a quantum-mechanics/molecular-mechanics (QM/MM) method known as ONIOM [159–165] provided by Gaussian03 [124]. The CNT-$(CH)_n$-CNT structures are divided into sections where each section is treated differently by theory. All atoms on an optimally constructed CNT, except for the linking atom, are fixed and treated as a rigid fragment at the MM level for both the contacts using the UFF force field [166]. The $(CH)_n$ chain along with the linking C atom on each of the two CNTs is relaxed using the B3LYP method [130, 157] with the 6-311G** basis set [167, 168].

Relaxing the truncated CNT contacts, using QM techniques, not only limits the choice of basis set size, but also distorts the tubes by flaring the ends outward. The ONIOM method takes advantage of electronic embedding by incorporating partial charges in the MM regions into the QM Hamiltonian thereby providing a better description of the electrostatic interactions between the QM and MM regions. Thus, by using ONIOM, one can maintain the rigid structure of a nominal CNT, thereby allowing the semi-infinite CNT contacts to be modeled appropriately.

In the second system, the polyacetylene chain is forced into an orientation such that the planar $(CH)_n$ molecule aligns perpendicularly with the tangential plane of the CNT at the point of contact. The perpendicular interface configuration is shown in Fig. 5.1(b). The perpendicular CNT-$(CH)_n$-CNT systems are initially built by relaxing only the $(CH)_n$ chain terminated with H, then removing the H termination

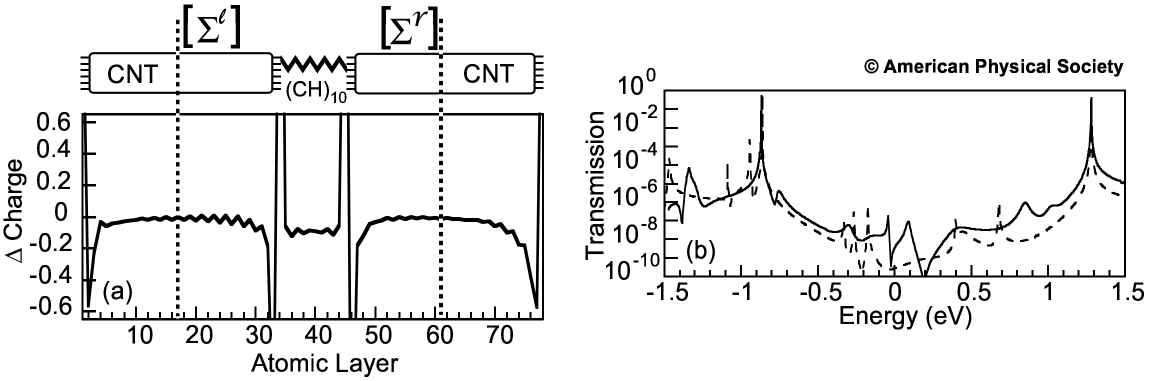

© American Physical Society

Figure 5.2: (a) Top: Illustration of the treatment of the CNT leads in the NEGF calculation. Bottom: Charge deviation across the relaxed CNT-$(CH)_{10}$-CNT structure. On the CNT, the charge is averaged over each atomic layer. On the $(CH)_{10}$ chain, the charge is just the charge on the C atoms. Each CNT contains 34 atomic layers of C with a H layers at each end. (b) Calculated transmission for the perpendicular CNT-$(CH)_{10}$-CNT system using extended 8 unit cell CNT contacts (solid) compared to extended 3 unit cell contacts (dashed).

and perpendicularly attaching the chain to nominal CNT contacts. The $(CH)_n$ chains are relaxed by Gaussian03 [124] using the B3LYP [130, 157] hybrid functional with a 3-21G basis set [169]. The CNT-$(CH)_n$-CNT system is studied using lengths of $n =$ 10, 20 and 40.

To satisfy the convergence criteria for the FIREBALL self-consistent calculation the cut CNT ends of both the co-planar and perpendicular systems are passivated with hydrogen. Without passivating the CNT ends do not reach a suitable self-consistent charge convergence threshold. DFT transport studies of CNT-Mol devices find localized states at the cut CNT sidewalls if left unpassivated which gives rise to additional transmission peaks resulting from surface states on the ends of the CNTs [1, 117, 158].

Hydrogen passivation also produces a charge dipole across the H - C bond at the passivated, cut ends of the CNTs as seen in Fig. 5.2(a). This causes a charge oscillation along the CNTs. The charge oscillation in a relaxed CNT-$(CH)_{10}$-CNT system is illustrated in Fig. 5.2(a) where atomic layers 1, 33, 45 and 78 are composed of hydrogen. The H layers are positively charged, and the adjacent C layers are negatively charged. The charge deviation between atomic layers is typically at a minimum near the center of each CNT. The eight unit cell CNT contact is an adequate length for truncating down to 4 or at a point where minimum oscillations occur on the CNTs.

The effect of finite CNT length on the calculated transmission is shown in Fig. 5.2(b). The solid line is the transmission calculated from a system with 4 unit-cell CNT leads truncated from 8 unit cells as shown schematically in Fig. 5.2(a). The dashed line is the transmission calculated from a system with 2 unit-cell CNT leads truncated from 3 unit cells. The two main resonant peaks are relatively unchanged. However, use of the longer leads tends to result in a smoother transmission curve with fewer spurious sharp resonances. Note that periodic boundary conditions cannot be used in the DFT calculation since the CNTs are not colinear.

5.3 Results

The interface alignments of the relaxed CNT-$(CH)_n$-CNT structures are relatively coplanar. The plane of the $(CH)_n$ is at no more than 31.1 degrees from parallel to the tangential plane of the CNT at the point of contact. The angles are defined in Fig. 5.3. Each relaxed and unrelaxed angle is listed in Table 5.1. The interface angles of each of these π-bond systems suggest that conjugated linking molecules will favor a relatively coplanar orientation with the CNT contacts. Every relaxed polyacetylene chain length from shortest to longest undergoes a 180 degree twist between the CNT

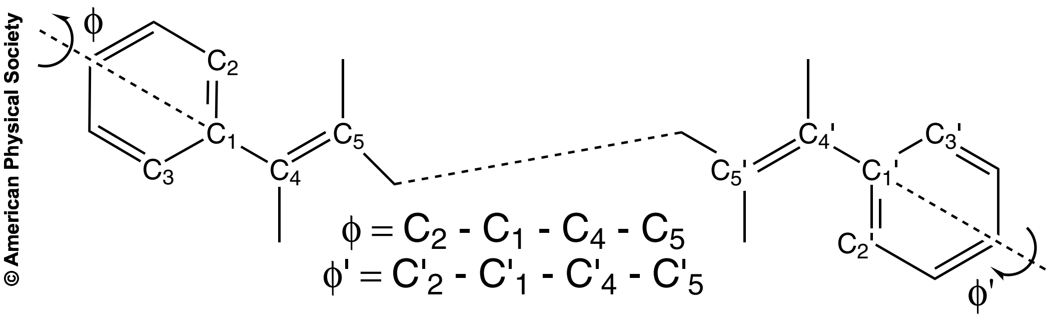

Figure 5.3: Definition of dihedral angles for the CNT-polyacetylene-CNT structures. The benzene rings represent the portion of the two CNTs to which *trans*-polyacetylene is attached.

Table 5.1: The dihedral angles (degrees) for the three CNT-polyacetylene-CNT structures investigated. The dihedral angles are defined in Fig. 5.3.

	ϕ	ϕ'	ϕ	ϕ'
CNT-$(CH)_{10}$-CNT	90.0	90.0	31.1	31.1
CNT-$(CH)_{20}$-CNT	90.0	90.0	24.4	24.5
CNT-$(CH)_{40}$-CNT	90.0	90.0	21.1	21.2

contacts with a decreasing co-planar interface angle for the longer $(CH)_n$ systems. The CNT sidewall chemistry affects the final orientation of the CNTs. The positively charged hydrogen atoms on the cut surface of the CNT and the closest hydrogen atom on the polyacetylene repel each other. This repulsion forces the axial angle of the CNT in a direction that reduces the repulsive force between H atoms. The CNT contacts in the perpendicularly oriented systems are rotated such that each hydrogen atom on the polyacetylene is directed away from the hydrogens passivating the CNT side walls.

Charge transfer occurs between the $(CH)_n$ chains and the CNT leads. Electrons transfer from the polyene to the CNT electrodes. A delta charge is calculated by summing the Löwdin charges [137] for each CH pair of the polyene and subtracting the neutral charge of $-5e$ where e is the magnitude of the electron charge. A delta

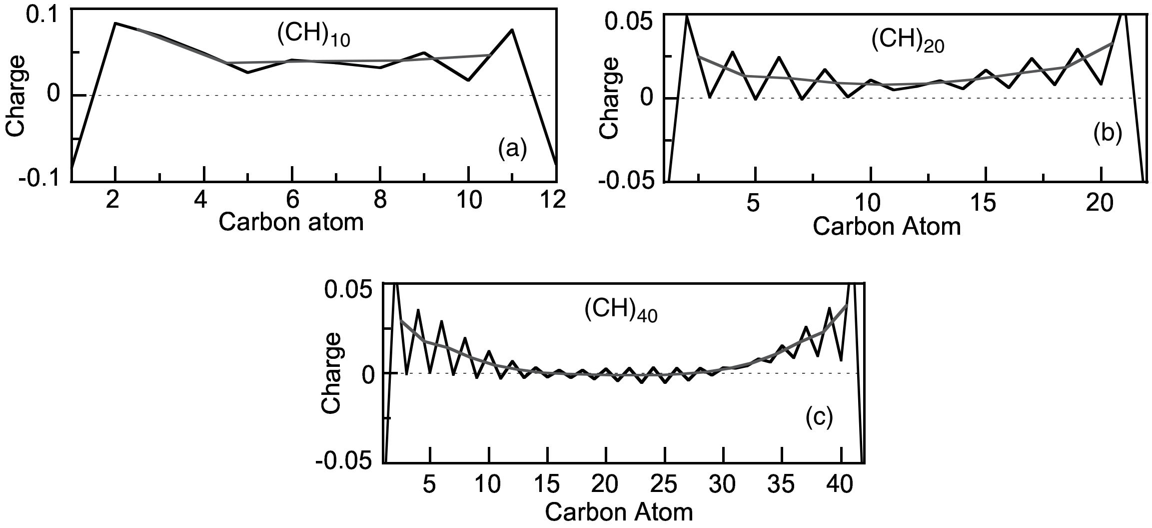

Figure 5.4: Delta charge in units of the magnitude of the electron charge for the three co-planar chains. The first and last atoms belong to the CNT leads. The points in between on the black curve represent the delta charge for each (CH) pair. The smooth gray curve is the average of the black curve over each $(CH)_2$ unit cell. The delta charge is calculated from the Löwdin charges as described in the text.

charge is also calculated for the connecting C atoms of the CNTs by subtracting $-4e$ from the Löwdin charge. Plots of the delta charge for the 3 co-planar structures are shown in Fig. 5.4. The first and last atoms are from the CNTs. The smooth gray line is the average over each $(CH)_2$ of the chain.

The shorter chains of $(CH)_n$ have, on average, a longer single C bond between each $(CH)_2$ unit cell in both the co-planar and perpendicular systems. Near the CNT contacts, the single C bonds change length between each unit cell. The single C bond lengths are shortest and relatively uniform over the 3 unit cells at the center of the chain. The CNT-$(CH)_{10}$-CNT system is the shortest polyacetylene length possible without non uniform single C bonds occurring over the entire molecule. The C double bond is more rigid and maintains an average length of $1.37 \mathring{A}$ for both the coplanar and perpendicular systems. Both the perpendicular and co-planar $(CH)_n$ single C bond lengths contract as n is increased thereby lowering the double/single C bond

Table 5.2: Single and double bond lengths ($\mathring{A}$) taken near the middle of the $(\mathrm{CH})_n$ and their difference for each system studied.

	Single C bond	Double C bond	Difference
$(\mathrm{CH})_{10}$	1.450	1.364	0.086
$(\mathrm{CH})_{20}$	1.437	1.367	0.070
$(\mathrm{CH})_{40}$	1.430	1.368	0.062

difference. Table 5.2 shows the double and single C bond lengths and their difference as n is increased. The bond lengths near the middle of the chain are identical for both the co-planar and perpendicular structures.

Plots of the calculated transmission for all 6 structures are shown in Fig. 5.5. The solid black line in each plot represents the transmission of the co-planar (relaxed) system, and the dashed line represents the transmission of the perpendicular system. The Fermi energy lies at 0eV for each co-planar and perpendicular CNT-$(\mathrm{CH})_n$-CNT system. The transmissions of the perpendicular systems are several orders of magnitude lower than those of the co-planar systems. The transmisison of the co-planar systems is large over broad ranges of energies, and, for all 3 systems, it is large near the Fermi level. The transmission spectra of the perpendicular systems have multiple sharp resonant peaks, and these peaks occur closer to the Fermi energy as the $(\mathrm{CH})_n$ is lengthened by increasing n.

The transmission in Fig. 5.5(a) is analyed first of the coplanar and perpendicular CNT-$(\mathrm{CH})_{10}$-CNT structures. The transmission of the perpendicular structure contains two fundamental resonances occurring at approximately -0.85 eV and 1.30 eV, respectively. The energy of the resonant peak at 1.30 eV is chosen for both the coplanar and perpendicular CNT-$(\mathrm{CH})_{10}$-CNT systems to inspect the spectral function across the $(\mathrm{CH})_{10}$ chain. The sharp transmission peaks of the perpendicular systems mark energies where the resonant wavefunction is localized on the polyacetylene chain.

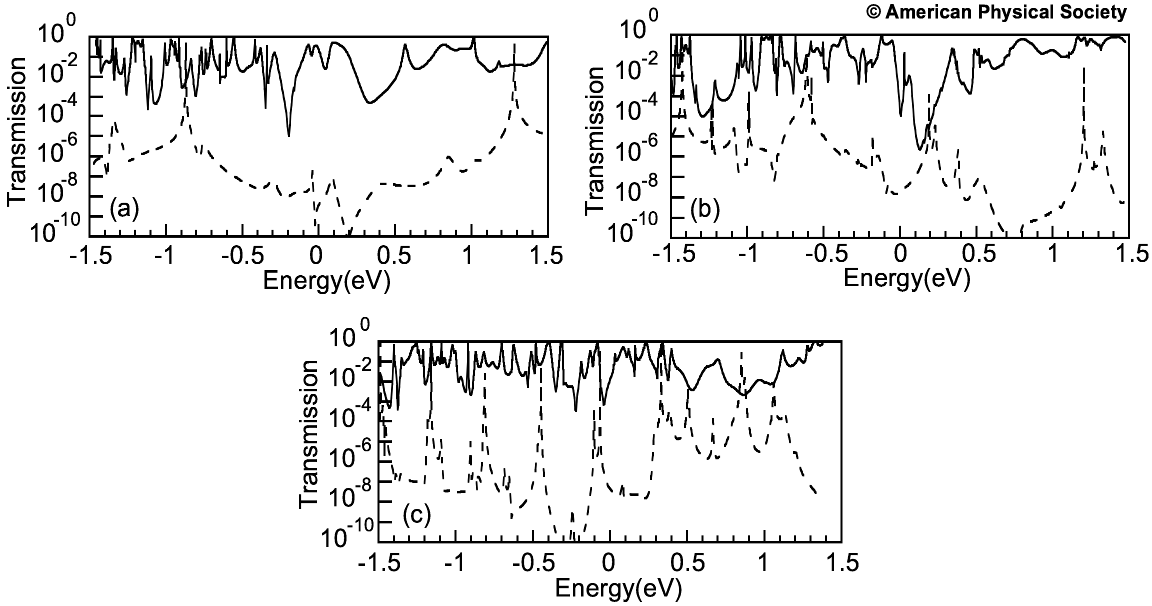

Figure 5.5: Calculated transmission of each CNT-$(CH)_n$-CNT structure for (a) $n = 10$, (b) $n = 20$, and (c) $n = 40$. The solid line is for the coplanar, relaxed structure, and the dashed line is for the perpendicular structure.

The spectral function plots at 1.30 eV for the coplanar CNT-$(CH)_{10}$-CNT system are shown in Figs. 5.6 (a) and (b). The 3D contour plot (a) shows that the spectral function is extended across the CNT contacts and the molecular chain. The black solid line in plot 5.6(b) is the spectral function on the C atoms of the molecular chain plus the connecting carbon atom on each of the CNT contacts. The CNT-$(CH)_{10}$-CNT inset shows the position of the C atoms. The atomically resolved spectral function rapidly varies. When it is averaged over a 2-atom unit cell to obtain an 'envelope' spectral function, it becomes smooth. The dashed line in Fig. 5.6(b) is the magnitude of the spectral function averaged over each unit cell of the polyacetylene.

The average spectral function in Fig. 5.6(b) has the shape of a fundamental resonance similar to the first quantized state of a quantum well. This confinement is increased by a factor of 1000 for the perpendicular CNT-$(CH)_{10}$-CNT spectral function illustrated in Figs. 5.6 (c) and (d). The spectral function in Fig. 5.6 (c) is

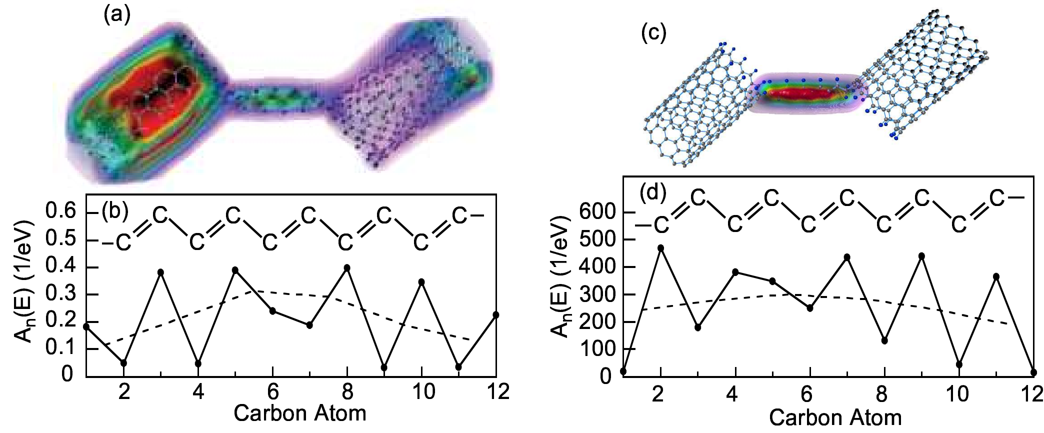

© American Physical Society

Figure 5.6: Plots of the covariant spectral function at energy E = 1.30 eV for $n = 10$. (a) and (c) are the 3D contour plots of the covariant spectral function of the coplanar and perpendicular structures, respectively. (b) and (d) plot the magnitude of the covariant spectral function on each C atom of the $(CH)_{10}$ chain plus the one attaching C atom on each CNT lead for the coplanar and perpendicular structures, respectively. The solid line is the spectral function traced over the basis states of the given atom, and the dashed line is obtained by averaging the solid line over 2 atoms that comprise the unit cell.

localized heavily on the $(CH)_{10}$ chain indicating strong confinement, weak coupling to the CNTs, and minimal transport between the CNTs. The weak coupling between the chain and CNTs results from the perpendicular orientation of the π orbitals at the interface.

The spectral function of the perpendicular structure is qualitatively similar to the wavefunction squared of the first excited state of a finite, conjugated 10-atom, C chain calculated in a π-bond model as shown in Fig. 5.7. Bond-length dependent Hamiltonian and overlap matrix elements, $H_{pp\pi}$ and $S_{pp\pi}$, were taken from Ref. [170, 171] for the actual bond lengths of the perpendicular $(CH)_{10}$ molecule. The key features of the wavefunction are relatively insensitive to the magnitude of the matrix elements. Atoms 2 - 11 of Fig. 5.6 correspond to the 10 atom C chain which is weakly coupled to the CNTs. In both Figs. 5.6 and 5.7, the magnitude is large on the end atoms, 2 and 11. For the coplanar structure, the shape of the spectral function in

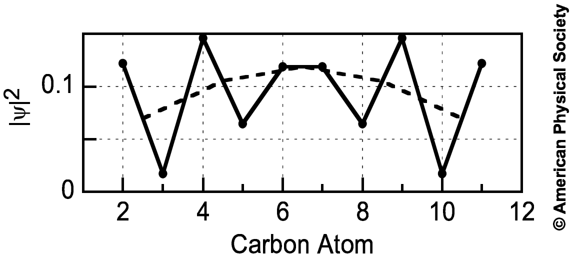

Figure 5.7: Magnitude squared of the first excited state of a conjugated 10 C atom chain in a π-bond model. The solid line is the magnitude squared of the coefficients of the π-orbital wavefunction on each C atom. The dashed line is obtained by averaging the solid line over each 2 atoms that comprise the 5 unit cells.

Fig. 5.6b is similar, but the spectral weight is on the opposite atoms so that the magnitude is at a minimum on atoms 2 and 11.

Extended states are observed for the coplanar geometry in the longer $(CH)_{20}$ and $(CH)_{40}$ systems, while strong confinement is observed for the perpendicular geometry in the $(CH)_{20}$ and $(CH)_{40}$ systems. The unit-cell averaged spectral function for both the coplanar and perpendicular geometries corresponding to transmission peaks occurring 0.5 eV or more from the Fermi level in the $(CH)_{20}$ and $(CH)_{40}$ systems exhibit multiple minimums and are similar to the excited states of a finite chain obtained from a π-bond model.

Near the Fermi energy, the spectral function along the chain for each *coplanar* CNT-$(CH)_n$-CNT system is examined to give insight into the transport near the Fermi energy which determines the conductance. Fig. 5.8 (a-f) shows the spectral functions for all three coplanar systems taken at energies corresponding to the transmission peak nearest to the Fermi energy. The 3D contour spectral function plots can been seen in Figs. 5.8 (a), (c) and (e). Again, the spectral function extends across the entire structure indicating strong coupling between the polacetylene chain and CNT contacts. The spectral function weights on the C atoms across the $(CH)_{10}$, $(CH)_{20}$ and $(CH)_{40}$ chains are plotted in Figs. 5.8 (b), (d) and (f) respectively. The polyacetylene

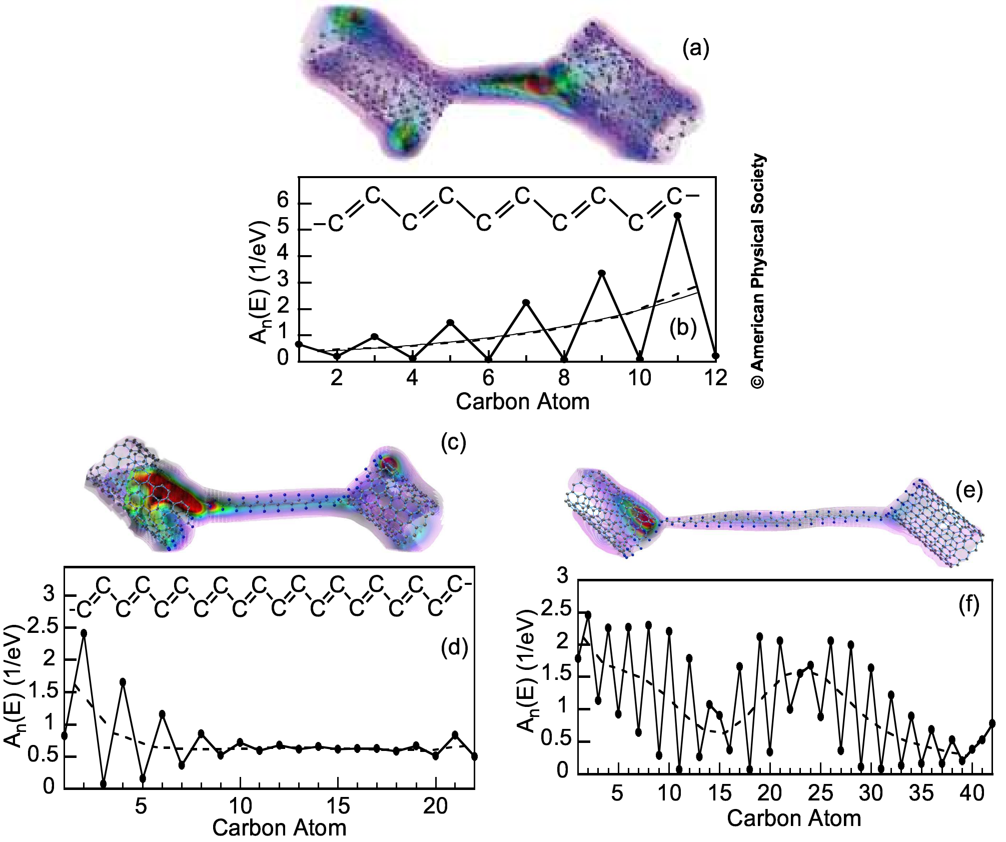

© American Physical Society

Figure 5.8: Covariant spectral functions of coplanar CNT-$(CH)_n$-CNT systems where (a,b) $n = 10$, (c,d) $n = 20$, and (e,f) $n = 40$ at an energy corresponding to a resonant transmission peak nearest to the Fermi level seen in Figs. 5.5 (a,b,c).

chain diagrams seen in Figs. 5.8 (b) and (d) again mark the first and last carbon atoms of the chain including the bonding C atoms of each CNT. The spectral functions again exhibit rapid atom to atom oscillation but with an average decay seen in Figs 5.8 (b) and (d). The average spectral function in Fig. 5.8 (f) has an oscillating component. The average spectral functions of the coplanar $(CH)_{40}$ system at other energies near the Fermi level all have oscillating components.

To obtain a value for an electronic decay constant in the $(CH)_n$ chain, the averaged spectral function is fit, shown in Fig. 5.8 (b), to an exponential function $e^{\pm\beta x}$. This definition of β is twice the imaginary decay constant of the wavefunction, and, for coherent transport, it corresponds to the definition of β determined experimentally from conductance versus length measurements in Refs. [172–174]. Of the 3 coplanar structures, only the $(CH)_{10}$ structure shown in Fig. 5.8 (b) has an average spectral function which is fit well by an exponential across the entire length of the chain. The exponential fit shown by the dashed line has a correlation coefficient of $R = 0.9946$ and a decay constant of $\beta_N = 0.386$ per double bond (2 C atoms) or, in terms of linear length along the molecular chain, $\beta = 0.154\ \mathring{A}^{-1}$. Since the total spectral function is the sum of the left and right connected spectral functions, Eqs. (2.13 - 2.14), one must examine the left and right connected spectral functions individually. The right connected spectral function is larger than the left connected spectral function by close to an order of magnitude. Its unit-cell averaged spectral function is a perfect fit to an exponential with a correlation coefficient of $R = 0.9998$ and a decay constant of $\beta = 0.198\ \mathring{A}^{-1}$.

The conductances for all CNT-$(CH)_n$-CNT systems are tabulated in Table 5.3. The conductances (G) for the coplanar relaxed systems start at $1.48e^{-5}$ (S) for the shortest $(CH)_{10}$ linker and then decrease to $6.77e^{-6}$ (S) for the $(CH)_{20}$ linker and $6.61e^{-6}$ (S) for the $(CH)_{40}$ linker. The conductances of the perpendicular structures

Table 5.3: Conductance (S) of the perpendicular and co-planar systems for each polyacetylene length listed.

orientation/length	$(CH)_{10}$	$(CH)_{20}$	$(CH)_{40}$
perpendicular	1.40×10^{-12}	6.14×10^{-12}	7.90×10^{-9}
co-planar	1.48×10^{-5}	6.77×10^{-6}	6.61×10^{-6}

have the reverse trend. The conduction increases from $1.40e^{-12}$ (S) in the for the $(CH)_{10}$ linker up to $7.90e^{-9}$ (S) for the $(CH)_{40}$ system.

5.4 Discussion

The opposite trends of conductance versus length for the the coplanar and perpendicular structures are striking. Both types of trends have been observed experimentally in conjugated molecules with metal contacts [172, 173, 175]. The carotenoid polyenes (Car) studied in Refs. [172, 173] exhibited a decreasing conductance with chain length. In Ref. [173], the conductance of 4 different length molecules were measured with polyene backbones consisting of $N = 5$, 7, 9, and 11 C=C double bonds. The length dependence of the conductance fit well to an exponential $G = G_0 e^{-\beta_N N}$ with $\beta_N = 0.556 \pm 0.09$ per double bond or $\beta = 0.22 \pm 0.04$ $\mathring{A}^{-1}$. A second set of conductance measurements on 3 different length Car molecules with polyene backbones consisting of $N = 7$, 9, and 11 C=C double bonds were performed within an electrochemical cell providing potential control [172]. Again, the length dependence of the conductance fit well to an exponential. The conductance of neutral Car gave a value for $\beta = 0.17 \pm 0.03$ $\mathring{A}^{-1}$ and the conductance of Car in an oxidized state resulted in a value for $\beta = 0.11 \pm 0.03$ $\mathring{A}^{-1}$.

Values for β have also been calculated theoretically from the complex band structure of periodic chain of $(CH)_2$ [176, 177]. Assuming a single C-C bond length of 1.45

$\AA$ and a double C=C bond length of 1.34 $\AA$, a maximum value for β of 0.394 per double bond or 0.159 $\AA^{-1}$ was obtained [177]. Assuming a single C-C bond length of 1.54 $\AA$ and a double C=C bond length of 1.34 $\AA$, a maximum value for β of 0.68 per double bond or 0.27 $\AA^{-1}$ was obtained [176].

For the coplanar polyene of this study, which showed a decrease in conductance with chain length, 3 lengths corresponding to $N = 5$, 10, and 20 C=C double bonds were studied. In the shortest system, the injected wavefunction squared into the polyene decayed exponentially with a decay constant ranging form 0.154 $\AA^{-1}$ to 0.198 $\AA^{-1}$ depending on whether the exponential was fit to the total spectral function or the right injected spectral function. These values lie within the range of those obtained experimentally for the Car and theoretically from the polyene. For the next longer system $(\mathrm{CH})_{20}$ corresponding to $N = 10$, neither the total nor left or right injected spectral functions fit well to exponentials. The total spectral function was determined primarily by the left injected spectral function and both reached a constant value 4 unit cells into the chain. The spectral function of the longest chain, $(\mathrm{CH})_{40}$ corresponding to $N = 20$, oscillated indicating constructive and destructive interference from states with either real or complex (but not purely imaginary) wavevectors.

The calculated conductance for the 3 coplanar chains did not decrease exponentially with chain length which is consistent with the wavefunctions near the Fermi energy in the chains. For the shortest chain, the wavefunction appears to be evanescently tunneling through the chain. For the longer $(\mathrm{CH})_{20}$ and $(\mathrm{CH})_{40}$ chains, the wavefunctions do not resemble evanescently tunneling wavefunctions, but, rather wavefunctions at or very near propogating energies. These energies would be at or near the valence band of the $(CH)_n$ chains. As shown in Fig. 5.4, electrons transfer from the polyene to the CNT electrodes. From a solid state point of view, this is p-type contact doping of the polyenes. From a chemistry point of view, this is contact oxidation of the polyenes.

For the perpendicular polyene structures, a trend of increasing conductance is found with increasing chain length which has been experimentally observed in conductance measurements of single oligothiophene molecules [175]. The authors in Ref. [175] reasoned that as the molecular bridge shortened, the lengths of the single C bonds increased while the lengths of the double C bonds remained relatively fixed. Within a simple π-bond model, the bandgap of a periodic chain of $(CH)_2$ is $E_G = 2(|t_d| - |t_s|)$ with $(|t_d| > |t_s|)$ where t_d is the C=C double bond Hamiltonian matrix element element and t_s is the C-C single bond Hamiltonian matrix element. Thus, the increased C-C bond lengths would result in a reduced coupling $|t_s|$ and an increased HOMO - LUMO gap for shorter chains. This, in turn, would result in a larger tunneling decay constant and reduced conductance for shorter chains. [52,175].

For the two different geometries studied here, coplanar and perpendicular, the effect of chain length on the single C-C and double C=C bond lengths is identical as shown in Table 5.2. However, the trend in conductance versus chain length is the opposite. The difference between the two structures is the geometry at the CNT - molecule interface. The coplanar geometry results in strong coupling of the molecule to the continuum of states in the metallic CNT leads. The perpendicular geometry results in weak coupling of the molecular states to the leads and sharp, widely spaced resonances in the transmission. As the chain length in the perpendicular geometry increases, the spacing of the resonances decreases, resulting in greater transmission near the Fermi energy and thus increased conductance. Thus, in this case, the effect of molecular chain length on the conductance is not an intrinsic property of the molecular chain; it is, rather, a property determined by the coupling of the molecule to the leads. With strong coupling, the conductance decreases with molecular chain length and with weak coupling, the conductance increases with molecular chain length.

5.5 Summary

The geometry of the CNT-$(CH)_n$ interface strongly effects the electron or hole transfer and conductance between CNTs. Transmission through the co-planar geometry is on average 3 or more orders of magnitude larger than that of the perpendicular geometry. The preferred minimum-energy configuration is a coplanar geometry with the plane of the $(CH)_n$ forming angles with the tangential plane of the CNTs of 31°, 24°, and 21° for n values of 10, 20, and 40, respectively. The CNTs provide p-type contact doping of the polyenes. For the shortest $(CH)_{10}$ polyene in the coplanar geometry, decay constants, β, ranging from 0.154 $\mathring{A}^{-1}$ to 0.198 $\mathring{A}^{-1}$ are obtained by fitting the spectral function to an exponential. These values match closely to decay constants extracted from experimental measurements of conductance versus chain length. The effect of molecular chain length on the conductance is a property of the coupling of the molecule to the leads. With strong coupling, the conductance decreases with molecular chain length, and with weak coupling, the conductance increases with molecular chain length.

Chapter 6

Conductance of a Conjugated Molecule with CNT Contacts

The conductance of an experimentally measured metallic carbon nanotube (CNT)-molecule-CNT structure is calculated [7]. The features in the predicted transmission correspond directly to the features of the isolated molecular orbitals. The highest occupied molecular orbital (HOMO) provides a weakly coupled conductive channel with transmission features that are qualitatively insensitive to the chemical end groups of the cut CNTs, the cut angle, the CNT chirality, and the number of molecular bridges. Quantitatively, however, these factors can modify the resonance width by an order of magnitude giving rise to corresponding changes in the resistance. Furthermore, the cut ends of a zigzag CNT can have surface states which hybridize with the molecular HOMO state giving a large transmission peak at the Fermi level. To understand the molecular energy level alignment with the CNT Fermi level, a quantum chemical calculation of the ionization potential and electron affinity and a density functional theory calculation of the CNT image potential are performed. A new twist on molecular conformation change switching is also suggested.

6.1 Introduction

Recently, carbon nanotubes (CNTs) have been used to contact single molecules [67, 114, 178, 179]. As yet however, there has been no attempt to model the conductance of these experimental systems. Prior studies examining model CNT-molecule-CNT structures find that molecular transport is influenced by the chirality of the CNT contacts [117, 180, 181]. Others report changes when examining the passivation chemistry at the cut ends of the CNTs [116] and the spatial gap between CNT contacts [182]. In this chapter a theoretical study is perform of an experimentally built CNT-molecule-CNT system described in [67].

Obtaining agreement between experimentally measured currents and density functional theory (DFT) transport calculations of metal-molecule-metal systems is difficult. DFT calculations do not give quantitatively accurate molecular HOMO and LUMO levels [21, 115, 183–188], and they do not include the potential on the molecule resulting from the surface polarization of the metal (i.e. the image potential) [183, 185, 189]. This results in an incorrect alignment of the molecular levels with the Fermi levels of the contacts [183, 190–192]. Several studies have addressed these limitations by correcting the DFT energy of the molecular states [185, 191]. Neaton et al. performed a quasi-particle GW correction to the DFT energies to take into account the polarization effect of the gold substrate upon physisorbing the molecule [185]. The study showed that the resulting energy shifts could be well approximated by considering separate calculations of the molecular ionization potential (IP), the electron affinity (EA), and the image potential and then treating these values as corrections or 'self-energies' to shift the DFT levels. This correction scheme was applied to the calculation of the conductance of benzene connected to gold through an amine linker, and it was shown to lower the traditionally too-large conductance value obtained from DFT to a value that agreed well with the experimental data [183]. For the CNT-molecule-CNT system, we proceed in the same fashion to understand the energy level alignment between the molecular orbitals and the Fermi levels of the CNT leads.

Agreement between theory and experiment is further complicated by the fact that the exact structure tested is not known. Unknowns are the chirality of the CNT, the angle of the cut ends that connect to the molecule, the passivation chemistry of the cut ends, the number of molecules connecting the CNTs, and the angle/site at which they connect. Therefore, to compare theoretical calculations with experimental measurements, one must simulate a number of probable structures to understand how different variations of the structure affect the conductance.

6.2 Method

Four different types of calculations are performed to model the system: (1) The entire CNT-molecule-CNT structure is relaxed using the DFT, tight-binding, molecular dynamics code Fireball as described in Chapter 2, sec. 2.2.1. (2) Once the structure is relaxed, the NEGF-Fireball approach is used to calculate transmission and conductance. This approach is discussed in Chap. 2, sec. 2.3 [6]. (3) The image potential is calculated by placing a positive charge between the two CNTs and performing a self-consistent Fireball / NEGF calculation described in Chap. 2, section 2.4 using a recursive Green function algorithm (RGF). (4) The molecular ionization potential (IP) and electron affinity (EA) are evaluated by computing the gas-phase energies of the neutral, cation, and anion molecule. Both vertical and adiabatic ionization potentials are determined.

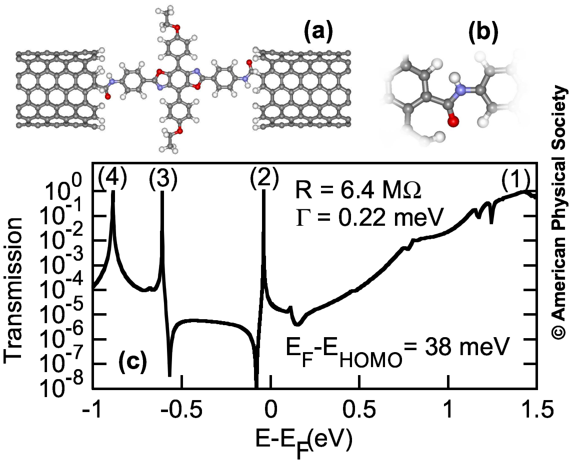

© American Physical Society

Figure 6.1: (a) Relaxed CNT-molecule-CNT structure with armchair (7,7) CNT contacts. (b) Closeup of CNT-amide bond relaxed configuration. (c) Calculated transmission of the armchair CNT-molecule-CNT structure.

6.2.1 Structure

The CNT leads of the CNT-molecule-CNT system are metallic and approximately 1 nm in diameter. Both (7,7) and (12,0) CNTs are used. The CNT leads are attached to the π-cruciform molecule labeled as molecule **1** of Ref. [67]. The molecule is covalently bonded to the CNTs via amide linkers. At the dodecyloxybenzene cross-arm ring ends, we attach a truncated C_2H_5 alkane chain instead of the $C_{12}H_{25}$ used in the experiment. Since the alkane chain has a wide HOMO-LUMO gap, this substitution should not affect the electronic states of the planar, conjugated molecule near the Fermi level. An example is shown in Fig. 6.1(a) using armchair (7,7) CNT contacts.

To construct this structure, we first construct the isolated planar molecule with amide groups attached at both ends. The amides are terminated by hydrogen. This isolated molecule is relaxed in gas-phase using FIREBALL.

To create the CNT leads, we begin with one DFT optimized CNT block-layer composed of 4 atomic-layers. We copy and repeat the CNT block layer in the axial direction. A length of the middle section of the CNT that most closely corresponds to the length of the molecule is removed. We assume that after the etching step, the CNT contacts are fixed in their position and the molecular window is governed by the one-dimensional atomic layer spacing of the CNTs [67, 178, 179]. We find that 18 atomic-layers (22.4 $\AA$) of a armchair or zigzag CNT is comparable in length to the relaxed molecule plus amide groups. The cut ends of the CNTs are passivated with either hydrogen atoms or carboxyl groups.

Eight CNT block-layers (32 atomic layers) for each contact are long enough to damp out charge oscillations at the outside end layers that result from the C-H charge dipoles at the cut interfaces [6]. The CNT contacts are at least 10 block layers (4 nm) in length from the molecule interface to each supercell edge. The relaxed molecule plus linkers is attached to the cut CNT ends. The entire supercell is relaxed using periodic boundary conditions. The Hamiltonian matrix elements of this structure are used for calculating the equilibrium transmission and conductance as described further in Chap. 2, Sec. 2.3.

6.2.2 Image Potential

For the calculation of the image potential, we extend the left and right CNT contact leads of the relaxed supercell by copying and repeating both left and right outside CNT block-layers. We lengthen both CNT contact ends to 10 nm giving a total length of approximately 22 nm for the entire structure. This ensures that the electric field from the point charge is well screened at the left and right boundaries. We remove the molecule and terminate the connection points on the CNTs with H. Then we add a point charge at the position r_0 corresponding to the center of the molecular HOMO level. The structure used for the calculation is shown in Fig. 6.2.

To calculate the image potential, first the molecule is removed with the connection

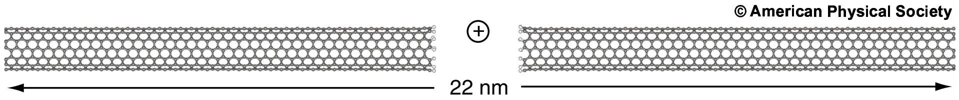

Figure 6.2: Structure used for the calculation of the image potential. The molecule is removed and the connecting C atoms of the CNTs are terminated with H. A positive point charge is placed at a point corresponding to the center of the molecule. The open boundaries at the left and right CNT ends are included via self-energies, and the charge is calculated with the recursive Green function algorithm.

points on the CNTs terminated with H. A point charge is next added at the position r_0 corresponding to the center of the molecular HOMO level. The potential resulting from the point charge is $-qV(\vec{r}) = \frac{-q^2}{4\pi\epsilon_0|\vec{r}-\vec{r_0}|}$, and the Hamiltonian matrix elements resulting from that potential are

$$\mathbf{V}_{i,j} = \frac{-q^2}{8\pi\epsilon_0}\left[\frac{1}{|\vec{r_i}-\vec{r_0}|}+\frac{1}{|\vec{r_j}-\vec{r_0}|}\right]\mathbf{S}_{i,j} \tag{6.1}$$

where i and j index the atoms at positions $\vec{r_i}$ and $\vec{r_j}$, q is the charge of an electron, and ϵ_0 is the permittivity of free space.

Once the charge occupation for the system converges with the added point charge, the electrostatic potential is evaluated across the junction in the plane of the molecule, along a series of points $\vec{r_k}$, using

$$\Phi_k = \sum_i \frac{(n_i - n_i^0)(-q)}{4\pi\epsilon_0|\vec{r_k}-\vec{r_i}|} \tag{6.2}$$

where $-qn_i$ is the valence charge associated with atom i, n_i^0 is the neutral atom charge, and $\vec{r_i}$ is the atomic position for every atom i of the 2 CNTs including the H atoms. Note that this sum does not include the point charge between the CNTs. The same self-consistent calculation is performed for the cut, H-passivated CNT in the absence of the extra point charge. The potential across the gap for this system

Φ^0 is also calculated using (6.2). The difference, $\Phi - \Phi^0$, gives the image potential.

For comparison and verification, we also model the image charge of a CNT-vacuum-CNT system by discretizing two grounded cylinders of sheet charge, assuming cylindrical symmetry, where each cylinder is 50 nm long and 1 nm in diameter. The cylinders are separated by 2 nm matching the molecular window used for the planar molecule between armchair CNTs. A point charge is placed between the 2 cylinders on the longitudinal axis. The induced charge on the cylinders is solved by the method of moments [193]. The potential between the cylinders is calculated from the equivalent of (6.2) where i indexes the discretized site, $n_0 = 0$, and $-qn_i$ is the charge on discretized site i.

6.2.3 Ionization Potential and Electron Affinity

Because experimental data for the energies of the highest occupied molecular orbital (HOMO) and lowest unoccupied molecular orbitals (LUMO) are unavailable for the molecules under study, we must obtain these properties theoretically. Typically, density functional theory is used to model large, complicated systems like these because of its general accuracy and low computational cost. However, both the DFT HOMO and LUMO levels frequently differ markedly from experimental results (see, for example, Refs. [186–188]).

We estimate the HOMO/LUMO levels and the quasiparticle gap relevant to electron and hole transport by calculating the gas-phase ionization potential (IP) and electron affinity (EA) of the molecule linking the CNTs [185]. Two possible definitions of IP and EA exist, vertical and adiabatic. If the electron transport occurs quickly relative to the timescale of molecular relaxation ($\sim 10^{-13}$–10^{-14} s), no nuclear relaxation occurs and the electron transport can be viewed as an electronic process (i.e. vertical excitation). On the other hand, if the transport occurs slower, the molecule can be expected to undergo both nuclear and electronic relaxation, in which case an adiabatic model is more appropriate, and zero-point energy (ZPE) effects may be important. The transport timescale τ can be estimated from the full width half maximum (FWHM) of the resonances in the transmission according to FWHM $= \hbar/\tau$.

Transmission resonances corresponding to different molecular levels can have transport timescales that reside in different regimes, so the most appropriate model depends strongly on the specific system and the molecular level primarily responsible for mediating the transport. The vertical IP and EA are evaluated by computing the energies of the neutral, cation, and anion molecules at the neutral-molecule geometry. The adiabatic quantities are computed from the anion and cation energies at their respective optimized gas-phase geometries. In all optimizations, the ends of the molecules are constrained to mimic attachment to fixed CNT leads.

Table 6.1: Computed gas-phase nitrobenzene quasiparticle energies

Type	IP (eV)	EA (eV)	Gap (eV)[a]
Experimental (adiabatic)	9.94 ± 0.08[b]	1.00 ± 0.01[c]	8.94
Koopman's Theorem[d,e]	6.83	3.56	3.26
Vertical[d]	9.69	0.84	8.86
Adiabatic w/out ZPE[d]	9.41	1.10	8.31
Adiabatic w/ ZPE[d]	9.35	1.19	8.16

[a] $\Delta E_{Gap} = IP - EA$

[b] Reference [194]

[c] Reference [195]

[d] Computed at the PBE/6-311+G(3df,2p) level

[e] $IP = -\epsilon_{HOMO}$, $EA = -\epsilon_{LUMO}$

In Table 6.1, we show calculated and experimental values of the IP and EA for the nitrobenzene molecule. This serves to illustrate the accuracy and discrepancies in the various calculations of the IP and EA from different theoretical models. It also serves to motivate a discussion of the issues unique to the use of localized orbital basis sets as opposed to plane wave basis sets in such calculations.

The table provides a good example of the type of differences one expects from the different models and the differences between theory and experiment. For the adiabatic quantities with ZPE corrections, the ZPE effects are estimated from harmonic vibrational frequency calculations. The values corresponding to the DFT HOMO and LUMO eigenvalues are in the row labeled 'Koopman's Theorem.' Clearly, DFT orbital eigenvalues can give HOMO/LUMO energy levels that are substantially in error, and obtaining these levels from a direct calculation of the IP and EA gives substantially better results.

The PBE density functional [196] (with the 6-311+G(3df,2p) basis set [197–199]) was chosen because it out-performed the BLYP functional in a benchmark study. In fact, its predictions were nearly as good statistically as the more expensive hybrid B3LYP functional. [200] That study of small-molecule ionization potentials and electron affinities found mean absolute (max) PBE errors of 0.16 eV (0.5 eV) and 0.11 eV (0.3 eV) relative to experiment. From these results, we estimate the error bars on our predictions to be roughly 0.5 eV and 0.3 eV for the IP and EA, respectively.

However, these statistical summaries belie significant complications associated with computing electron affinities. If the exact density functional were known, DFT could describe both the neutral and anionic species well, and the EA could be predicted readily. However, the incorrect asymptotic behavior of typical approximate exchange-correlation functionals leads to pronounced self-interaction error at long ranges. This self-interaction error causes a systematic under-binding of the excess electron in the anion, particularly in atoms and small molecules. On the other hand, the finite localized basis sets used to represent the density artificially constrains the excess electron to remain near the nuclei, causing an artificial stabilization. Cancellation of errors between these two effects in most cases produces the overall good predictions quoted above [201].

Nevertheless, problem cases can arise, particularly when describing weak or negative EAs and non-valence anion states [201–203]. Standard basis sets are woefully incomplete for describing such states [204], since the loosely bound electron occupies a very diffuse orbital. This tendency for the extra electron to reside far from the molecule also magnifies the impact of self-interaction error. One indicator for such difficulties is slow convergence of or large fluctuations in the EA with respect to increasing basis set size.

For example, in the case of benzene (without the nitro- group), the BLYP vertical EA ranges from -2.2 eV in the small 6-31G(d,p) [205, 206] basis, to -1.1 eV in the moderate 6-311+G(3df,2p) basis, to -0.3 eV in the 6-311++G(3df,2p) basis set augmented with two additional sets of extremely diffuse functions. In some other basis sets, benzene's EA is even positive. Clearly, the prediction of the EA for benzene is theoretically challenging. In contrast, adding the same additional diffuse basis functions to 6-311+G(3df,2p) for nitrobenzene has negligible effect on the EA, altering the predicted EA by only $\sim$10%.

Unfortunately, the large size of the linker molecule here makes it impractical to test large, extremely diffuse basis sets. These 6-311+G(3df,2p) calculations already involve 2142 basis functions, and very diffuse basis functions limit the effectiveness of sparsity-based fast DFT algorithms for large systems. However, predictions of a large, positive EA for a valence anion state are highly suggestive that the DFT results are meaningful and accurate. As demonstrated in Sec. 6.3.2 below, all of these indicators suggest that the EAs for this system can be predicted with reasonable accuracy. Furthermore, our primary interest in this work is the ionization potential (IP), since transport in our system is mediated by the HOMO.

For the large molecule of this study, all IP and EA energy calculations are performed using the DFT package Q-Chem 3.1 [10] using the BLYP density functional in the 6-311+G(3df,2p) basis set. The constrained geometry optimizations (described above) are performed in the 6-31+G(d,p) basis [198, 205, 206]. The ZPE is not included.

6.3 Results

First results will cover equilibrium transmissions for several physical implementations of the CNT-molecule-CNT system. These results will show the effect of CNT chirality, passivation chemistry, cut angle, and multiple molecules on the transmission spectrum. Next the energy level alignment between the molecular HOMO and LUMO levels and the Fermi level of the CNTs will be considered.

6.3.1 Transmission and Conductance

Armchair CNTs, H-passivation, single-molecule

We first examine the transport characteristics of an armchair CNT-molecule-CNT system shown in Fig. 6.1(a). The C sites along the edge of the armchair CNTs, shown in Fig. 6.1(b), have bonding angles that allow us to initially orient the plane of the molecule parallel to the tangential plane of the CNT at the point of contact. The system remains stable during the DFT relaxation, and the dihedral angle between the plane of the amide groups and the tangential plane of the CNTs at the point of contact changes by no more than 14.1 degrees from parallel after relaxation.

In Fig. 6.1(c), we show the calculated transmission spectrum of the armchair CNT-molecule-CNT system as a function of the difference $E - E_F$. The transmission

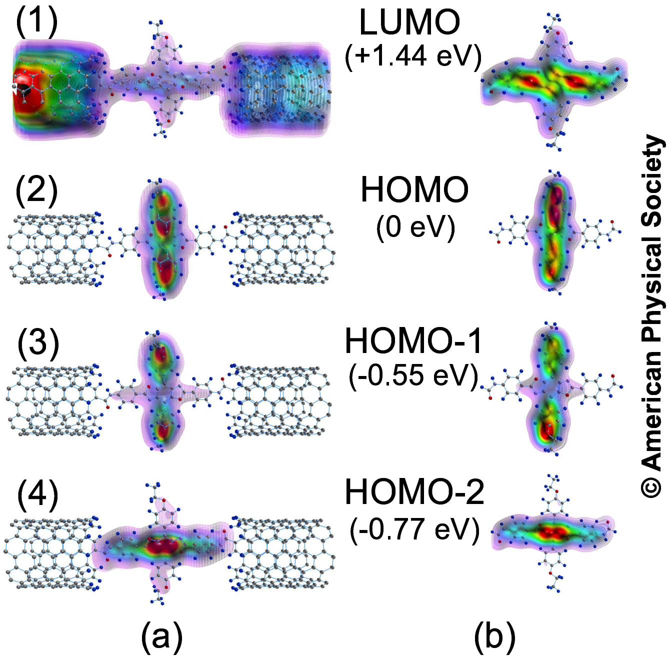

Figure 6.3: (a) 3D contour plots of the covariant spectral function corresponding to the resonant peaks marked in Fig. 6.1. (b) Corresponding molecular orbitals for the relaxed isolated molecule in the planar conformation. Amide groups are included at the left and right ends of each molecule.

of the molecule has a resonant peak 38 meV below the Fermi energy, $(E_F - E_{HOMO}))$ which results in a room temperature (300 K) resistance of 6.4 MΩ. The resonant peak has a FWHM (Γ) equal to 0.22 meV. The experimental measured resistance is 5 MΩ [67].

To understand the transmission curve we compare the covariant spectral functions [6], shown in Fig. 6.3 (a) to the molecular orbitals of the molecule in vacuum in Fig. 6.3(b). The spectral function labels (1-4) correspond to the labeled transmission peaks in Fig. 6.1(c). The energies listed in eV next to the molecular orbitals are the differences in energy of the molecular orbitals in vacuum with respect to the molecular HOMO in vacuum.

The broad transmission peak (1) corresponds to the molecular lowest unoccupied molecular orbital (LUMO), approximately 1.4 eV above the HOMO, where the spectral function is spread across both the CNTs and the molecule. The broad peak in transmission indicates that the coupling of the CNT states to the molecular LUMO is strong, which is consistent with the large spatial spread of the spectral function across both the molecule and the CNTs.

Peak (2) in the transmission curve results from the coupling of the CNT states to the highest occupied molecular orbital (HOMO). The HOMO is localized on the cross-arm of the molecule away from the CNTs and is weakly coupled to the contacts. The narrowness of the HOMO transmission peak is the result of two things. (i) The molecular orbital is spatially localized away from the CNTs, and (ii) the spectral weights near and on the C atom part of the amide linkers are low. We note that the effect of the amide linkers is consistent with previous studies which also found that amide linkers reduce the coupling of the CNT states to the molecular HOMO orbital [180, 181]. The Fano resonance at peak (2) results from the two parallel paths through the molecule. An electron can tunnel through the tail of the extended state (1) or it can tunnel through the localized state (2).

Transmission peak (3) corresponds to the HOMO-1 state, approximately -0.5 eV below the HOMO, peaked on oxygen atoms of the upper and lower portions of the cross arm. Transmission peak (3) is also a Fano resonance arising from the two parallel paths corresponding to the HOMO-1 state localized on the cross-arms and the HOMO-2 state extended across the molecule.

Although the LUMO and HOMO-2 levels extend across the molecule, the resonance due to HOMO-2 is sharp compared to that of the LUMO. The narrowing of HOMO-2 resonance compared to the LUMO is again consistent with other studies using amide linkers [180, 181].

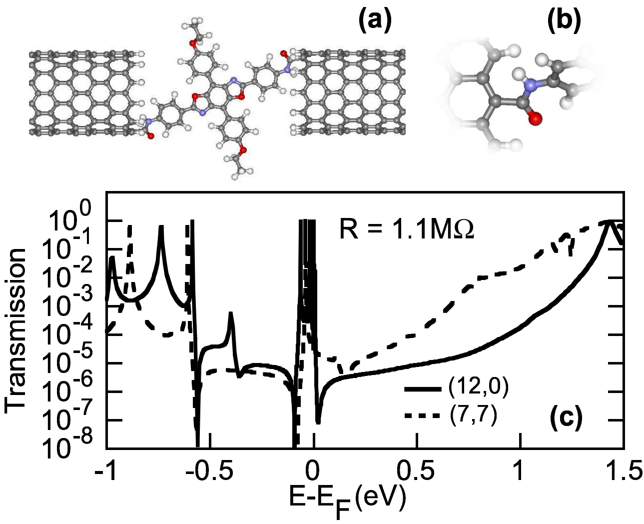

© American Physical Society

Figure 6.4: (a) Relaxed CNT-molecule-CNT structure with with zigzag (12,0) CNT contacts. (b) Closeup of CNT-amide bond configuration. (c) Calculated transmission of the zigzag CNT-molecule-CNT structure (solid) and the armchair CNT-molecule-CNT structure (dashed).

Zigzag CNTs, H-passivation, single-molecule

To investigate how the contact chirality affects transport, we attach (12,0) CNT contacts approximately 1 nm in diameter, to the molecule shown in Fig. 6.4(a). The axial direction of the C-H bonds at the cut ends of the CNTs prevents us from attaching the molecule directly across the junction, parallel to the CNT axis. Instead, the molecule is attached across the CNTs with attachment points $4\frac{1}{2}$ H atoms apart. The fraction $\frac{1}{2}$ comes about because the cut ends of the left and right CNT differ by one atomic layer. A close up of one attachment is shown in Fig. 6.4(b). This configuration forces some twisting of the amide linkers with respect to the molecule and the CNTs. The relaxed dihedral angle between the amide linker and tangential plane of the CNT at the point of contact is 43 degrees on the left and 32 degrees on the right. The relaxed dihedral angle between the amide linker and plane of the molecule is 19 degrees on the left and 26 degrees on the right.

Figure 6.4(c) shows the transmission spectrum of the CNT-molecule-CNT structure with (12,0) zigzag CNT contacts (solid line) overlaid on the transmission spectrum from Fig. 6.1(c) (dashed line). The important difference between the two curves is the splitting of the HOMO transmission peak into multiple split transmission peaks near the Fermi energy. The splitting results from the HOMO state interacting with H passivated surface states at the CNT interface. This results in a room temperature (300 K) resistance of 1.1 MΩ.

Fig. 6.5(a) provides a closer look at the transmission near the Fermi energy where the solid and dashed lines are re-plotted from Fig. 6.4(c) over a small range of energy near E_F. The inset figure shows the cluster of peaks marked by a dashed circle near E_F. Here we see two peaks below and above the Fermi energy. The covariant spectral functions corresponding to each of the transmission peaks, labeled (5) through (10) are shown in Fig. 6.5(b). The single peak observed using armchair contacts splits into 6 peaks when zigzag contacts are used. The peaks result from the interaction of the the molecular HOMO state, the surface states of the left CNT, and the surface states of the right CNT. This is clearly seen in the spectral function plots. Multiple, nearly-degenerate, surface states immediately above and below E_F on finite length, H-passivated, zigzag CNTs have been observed by others [151].

The states shown in Fig. 6.5(b) labeled (5) through (8) corresponds to a mixture of two surface states and the molecular HOMO. The middle state labeled (9) is a mixture of two surface states. The lowest state labeled (10) is primarily the molecular HOMO, and its transmission resonance has a FWHM of $\Gamma = 0.27$ meV very similar to the HOMO resonance with armchair leads. Thus, surface states of the zigzag CNTs occur at and near the Fermi level, and their interaction is mediated and enhanced by the proximity of the molecular HOMO energy level. This gives rise to large transmission at the Fermi level. This enhancement of transmission through different conjugated

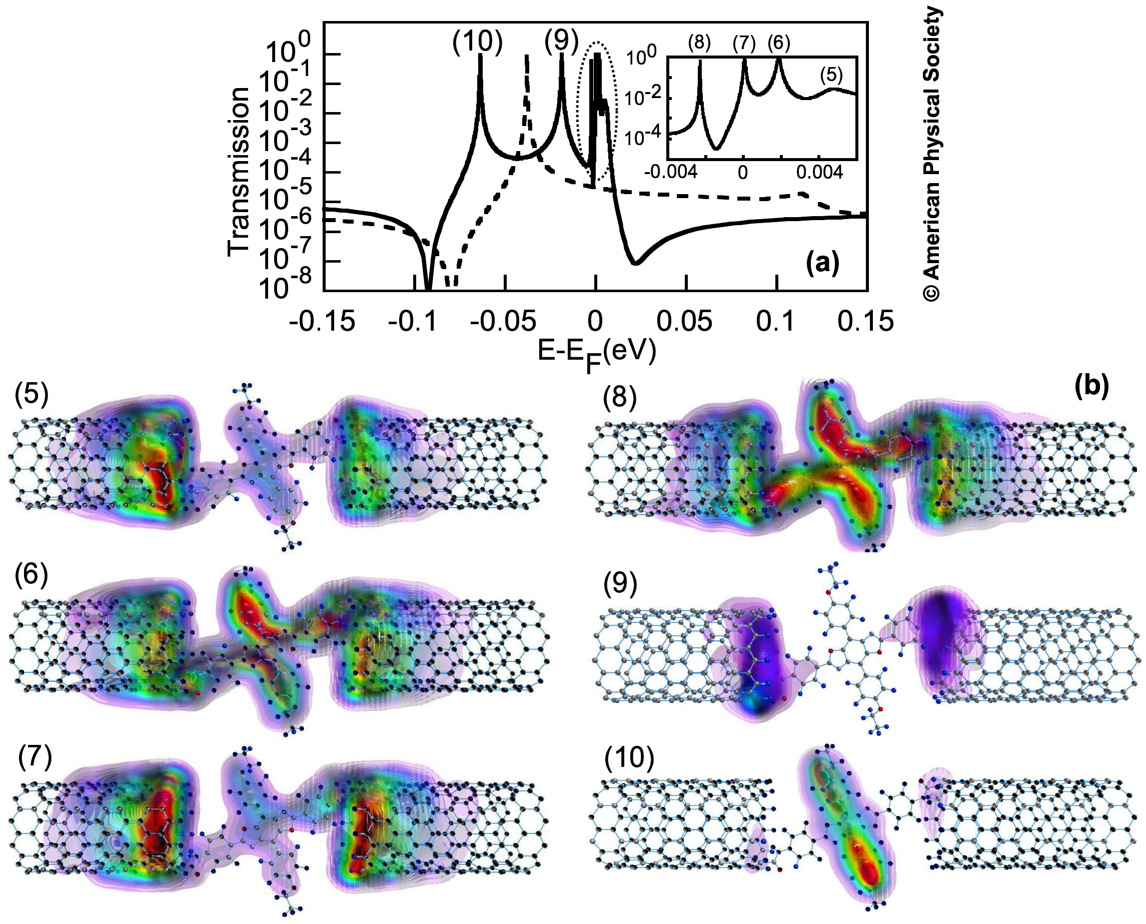

Figure 6.5: (a) Calculated transmission close to the Fermi energy where the solid line represents the zigzag system and the dashed line represents the armchair system. (b) The spectral functions corresponding to the resonant transmission peaks marked in (a) for the zigzag CNT-molecule-CNT structure. Inset shows peaks clustered above and below $E_F = 0eV$

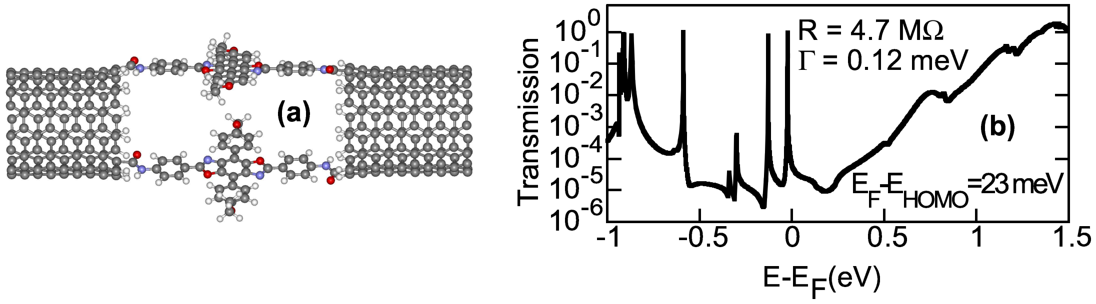

Figure 6.6: (a) Relaxed armchair CNT-molecule-CNT structure with two planar molecules attached. (b) Calculated transmission of CNT-molecule-CNT system shown in (a).

molecules at the Fermi level with both H-passivated and unpassivated zigzag CNT leads has also been observed by others [117, 180].

The results shown in Figs. 6.1 - 6.4 show that for both the metallic armchair and zigzag CNT-molecule-CNT structures, the transmission is directly mapped to the features of the isolated molecular orbitals and the surface states of the cut ends of the CNTs.

Two Molecules

Experimentally it has been suggested that up to two molecular bridges might be established across the gap during the dehydration reaction [67]. To model such a system, we attach one additional molecule to our initial optimized armchair CNT-molecule-CNT structure and perform a DFT relaxation. Fig. 6.6(a) shows the relaxed armchair CNT-molecule-CNT system where an additional planar molecule is attached parallel to the original molecule shown in Fig. 6.1(b). The maximally separated configuration of the two molecules shown here is known to be energetically favorable [116].

The two molecule transmission is shown in Fig. 6.6(b) where we observe a doubling of peaks near the Fermi level giving a calculated resistance of 4.7MΩ. As expected, the peaks are again associated with the same orbitals previously discussed and shown in Fig. 6.3. The addition of one molecular bridge reduces the resistance, but not by a factor of two. The resistance is sensitive to the position of the HOMO resonant transmission peaks with respect to the Fermi level. The two peaks from the two molecules split and shift compared to the single peak from a single molecule.

Passivation Chemistry and Cut Angle

While the molecular end groups on the cut ends of the CNTs are not known, it is reasonable to assume that the CNT ends remain functionalized with carboxyl groups (COOH), rather than H atoms after the dehydration reaction [67]. However, we note that passivating an armchair CNT cut edge completely with carboxyl groups is not possible due to steric hindrance. Other end groups are possible [207], however, in this work, we consider only COOH and H. We also note that attaching molecule **1** to a vertically cut armchair or zigzag CNT passivated with carboxyl groups results in a structure which is difficult to relax at the DFT level.

To mimic a complex CNT e-beam etch window, we cut a (7,7) armchair CNT non-vertically, along a zigzag edge leaving one armchair edge at the base of the cut. The structure is shown in Fig. 6.7(a). The thicker C and H atoms and bonds outlined in the top view mark the cut edge of the CNT side walls. The zigzag edges are passivated with carboxyl groups except for the last two at the top of the cut. These edges are passivated with hydrogen due to steric hindrance. The molecule is attached at the bottom armchair edges across the shortest portion of the gap. The relaxed plane of the amide linkers are no more than 24.2 degrees from parallel to the tangential plane of the CNTs at the point of contact.

The transmission is shown in Fig. 6.7(c) by a solid line. The calculated resis-

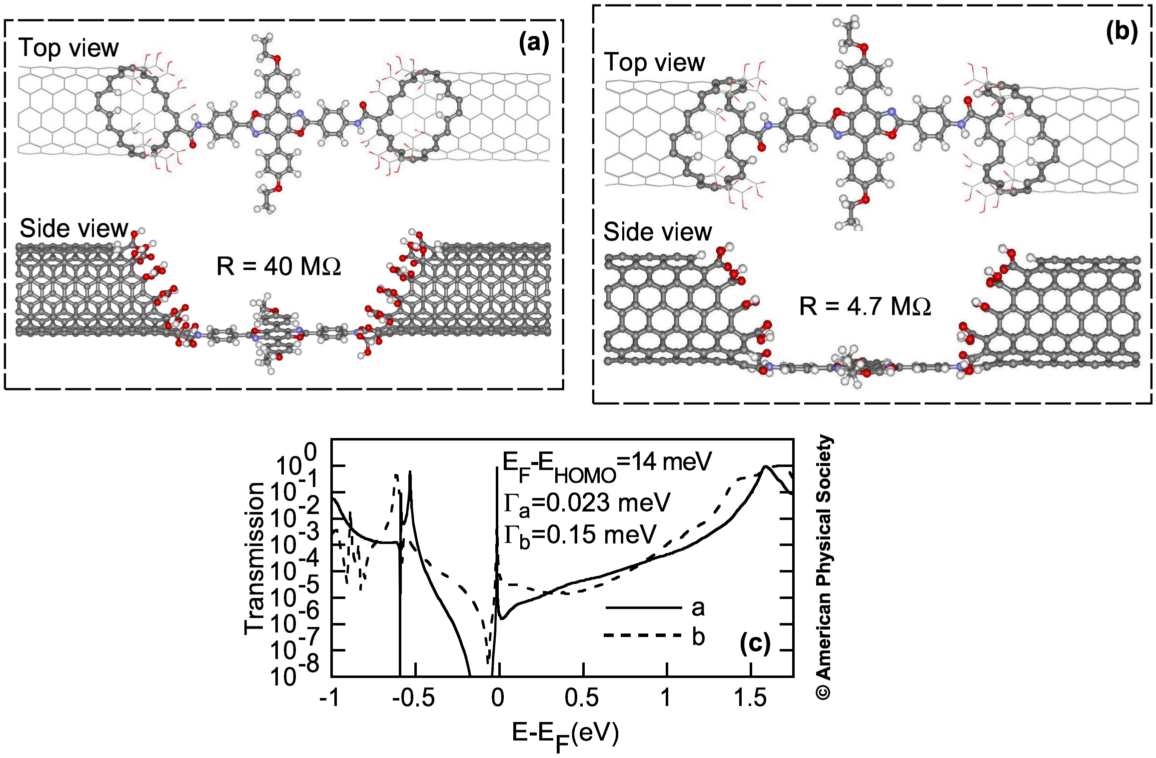

© American Physical Society

Figure 6.7: (a) Top and side views of a relaxed CNT-molecule-CNT structure with the CNT side walls passivated with carboxyl group molecules. Bolder atoms and bonds in top view represent the cut edge of the CNTs. (b) Top and side views of a relaxed CNT-molecule-CNT structure with the CNT side walls passivated with carboxyl/hydrogen molecules. Bolder atoms and bonds in top view represent the cut edge of the CNTs. (c) Calculated transmission of CNT-molecule-CNT systems shown in (a) (solid) and (b) (dashed).

tance is 40 MΩ. The features remain qualitatively comparable to the features of the transmission in Fig. 6.1(c) where the spectral function at each peak again matches the features of the isolated molecular orbitals shown in Fig. 6.3. The LUMO and HOMO-2 peaks shift deeper into the conduction and valence bands, respectively. The position of the HOMO resonant peak is 14 meV below the Fermi level. For comparison, the peak of the HOMO resonance in Fig. 6.1(c) is 38 meV below the Fermi level. Quantitatively, we find a narrowing of the resonant peaks where the full width at half maximum (Γ_a) of the HOMO resonance is 0.023 meV. The narrowing of the valence band resonances indicate less coupling of the molecular states to the continuum of states in the CNT contacts. Thus, the cause for the increased resistance of the structure compared to that of the structure in Fig. 6.1 is the result of the narrowing of the HOMO resonance by a factor of 9.

To determine if the passivation chemistry is affecting the resonant widths, we substitute H for each carboxyl group in the structure. We find that the hydrogen passivation narrows each resonance peak further which increases the resistance to 455 MΩ. This narrowing of the resonances due to H passivation is consistent with work done by Ren *et. al.* [116] where passivated carboxyl groups were compared to H passivation on semi-conducting (13,0) CNTs connected by a single diaminobenzene molecule. Ren *et. al.* found that the resonant peaks broaden in the valence and conduction band regions when the side-walls are passivated with carboxyl.

Next, the cut shown in Fig. 6.7(a), is slightly modified to leave two armchair edges intact on either side of the molecule at the bottom of the cut. The modified interface and structure are shown in Fig. 6.7(b) where the top view thick atoms/bonds mark the CNT edge. We passivate the zigzag edges using carboxyl groups and use a mix of carboxyl groups and H for the remaining armchair edges. The molecule is positioned and oriented exactly as it is in the configuration shown in (a). We also note that the

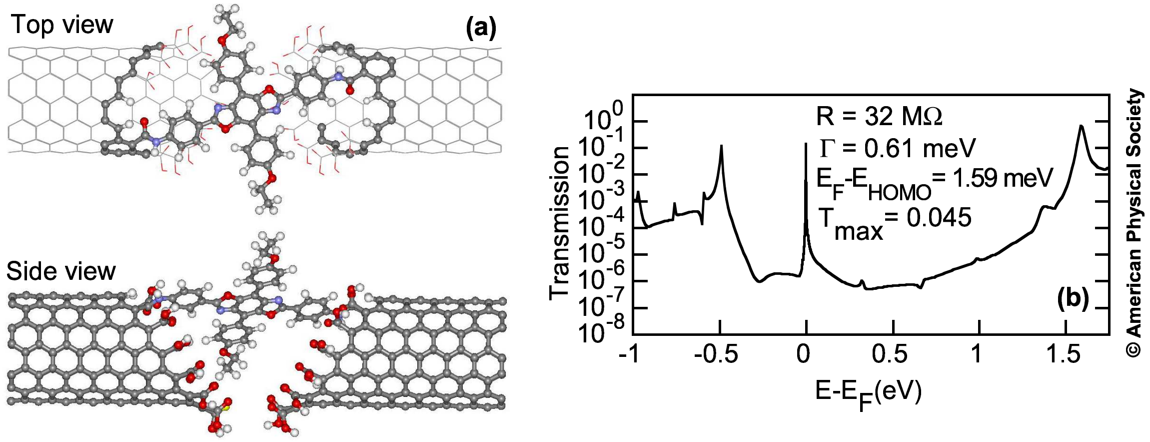

© American Physical Society

Figure 6.8: (a) Top and side views of a relaxed CNT-molecule-CNT structure with the CNT side walls passivated with carboxyl group molecules and the molecule attached on top. Bolder atoms and bonds in top view represent the cut edge of CNTs. (b) Calculated transmission of CNT-molecule-CNT systems shown in (a).

molecule to CNT interface connection is similar to the cut and chemistry configuration used in Fig. 6.1(b).

The transmission is shown in Fig. 6.7(c) by a dashed line. The energy of the transmission peak remains the same, however, the width of the HOMO resonance increases from 0.023 to 0.15 meV. The increase in coupling results in a decrease of resistance to 4.7 MΩ. A small change in the cut edge geometry results in nearly an order of magnitude change in the resistance. In this case, the change consisted of modifying the cut edge from zigzag to armchair in proximity to the molecule.

We consider a final cut and attachment geometry which results in asymmetric coupling of the HOMO level to the leads. We use the non-vertical cut geometry shown in Fig. 6.7(a) with the CNTs closer together so that the cut window is not wide enough to accommodate a molecule at the bottom of the cut, and the molecule attaches across the top of the gap. The structure is shown in Fig. 6.8(a). The relaxed molecule is attached via zigzag edges. All zigzag edges are passivated with carboxyl groups. Due to steric hindrance, we use H for the top zigzag edge and edges near the

NH groups of the amide linkers.

The calculated transmission is shown in Fig. 6.8(b). The resistance is 32 MΩ. The features remain qualitatively comparable to the features of the transmissions in Fig. 6.7(c), however the position of the HOMO resonant peak has shifted to 1.59 meV below the Fermi level. For the first time, the maximum transmission of the HOMO resonance does not reach unity ($T_{max} = 0.045$). The FWMH of the HOMO transmission resonance is 0.61 meV. This decreased peak height is due to asymmetrical coupling of the left and right CNT contacts. The left contact dihedral angle between the molecule and tangential plane of the CNT is 12 degrees and the right dihedral angle is 52 degrees. Assuming a Lorentzian form for the resonance, the peak height and width give two equations for two unknowns, the energy broadening due to the left, Γ_L, and right, Γ_R, contacts. The FWHM $\Gamma = \Gamma_L + \Gamma_R$. Solving, we obtain $\Gamma_L = 0.598$ meV and $\Gamma_R = 0.00681$ meV.

For all three non-vertically cut CNT-molecule-CNT structures with carboxyl passivation, the transport features are comparable to the transport results described in sections 6.3.1 and 6.3.1. We find a weakly coupled HOMO resonance appearing near the Fermi energy. However the resonant width, peak value, and position vary significantly as a result of the passivation chemistry, the geometry of the cut, and the geometry at the point of connection of the molecule to the CNTs. These dependencies confirm that structural and chemical unknowns can cause significant variation of the resistance of the CNT-molecule-CNT system.

Molecular Conformation

Lastly, we investigate how the molecular resonances are modified by changing the molecular conformation. We explore this by rotating the cross-arm ethoxybenzene rings in opposite directions. We find that only a planar and perpendicular gas-phase

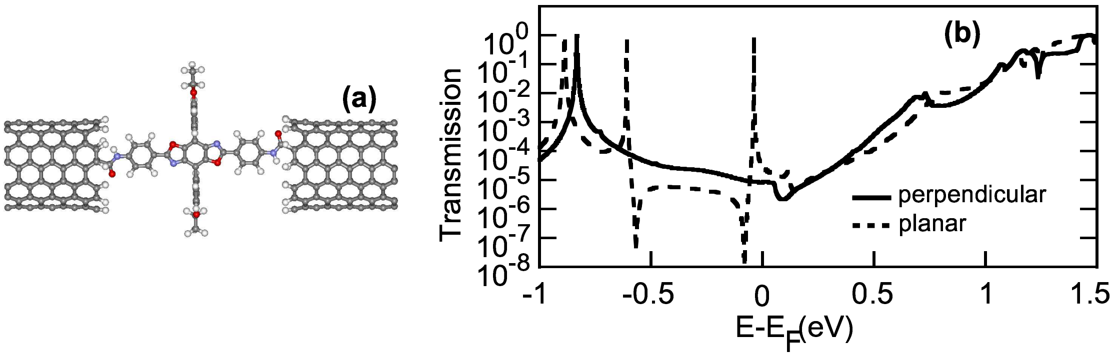

© American Physical Society

Figure 6.9: (a) Relaxed CNT-molecule-CNT structure with a perpendicular ethoxybenzene cross-arm conformation molecule attached. (b) Calculated transmisson comparison where the solid line is for the system shown in (a) and the dashed line is for the planar ethoxybenzene cross-arm conformation shown in Fig. 6.1(a).

conformation is stable during relaxation with the planar conformation energetically favorable by 1.4 eV. Using the H-passivated, armchair CNT contacts, we relax the entire supercell using the perpendicular molecular conformation, resulting in the structure shown in Fig. 6.9(a).

The planar and perpendicular transmissions are shown in Fig. 6.9(b). Here the LUMO and HOMO-2 resonance peaks in both systems remain qualitatively the same. The HOMO-1 and HOMO transmission resonances, however, near the Fermi energy in the perpendicular configuration are removed. The absence of the HOMO transmission resonances gives a resistance of 1.6 GΩ. From the molecular orbital plots we find the HOMO and HOMO-1 are still localized on the cross-arm ethoxybenzene groups, however they are split in the middle and decoupled from the molecular bridge. The perpendicular conformation gas-phase HOMO and HOMO-1 levels appear nearly degenerate (0.02 eV difference) at 0.96 eV below the Fermi energy. For comparison the planar conformation gas-phase HOMO and HOMO-1 levels are 0.72 eV and 1.27 eV below the Fermi energy.

By rotating the ethoxybenzene rings we break the π-conjugation with the rings on the horizontal axis of the molecule thereby suppressing the HOMO and HOMO-1 level from the transmission spectrum. The HOMO and HOMO-1 levels associated with the cross-arm are decoupled from the molecular bridge leaving no states near the Fermi energy to carry current. This results in an increase the resistance by over 2 orders of magnitude.

The use of conformation change for molecular switching is well known. Several examples are rotaxane [14, 208], 1,4-bis-phenylethynyl-benzene [24], and 2'-amino-4-ethylphenyl-4'-ethylphenyl-5'-nitro-1-benzenethiolate [95, 209], which we refer to as the nitro molecule. In all cases the conformation change of the molecules alters the molecular orbitals along the path of the electron transport. In the nitro molecule, the conjugation is broken directly in the transport path between each contact. In rotaxane, the orbital changes from extended to localized along the transmission path of the molecule. For the cruciform molecule configurations, shown in Figs. 6.1(a) and 6.9(a), the effect of conformation is different. The rotation of the vertical rings does not affect the conjugation along the horizontal axis of the molecule, and it does not localize a previously extended state along the axis of the molecule. Instead, it decouples the HOMO from the transport path which results in an exponentially decreased transmission near the Fermi energy. This is a new twist on the conformation-change paradigm of molecular switching from a three-terminal-device point of view [179].

6.3.2 Energy Level Alignment

In all the different CNT-molecule-CNT configurations presented, the HOMO resonance provides a weakly-coupled transport path through the planar molecule that is qualitatively insensitive to the interface orientation, CNT chirality, the number of molecular bridges, the molecule-CNT site connection or the termination chemistry.

Overall the resistances of the planar molecule listed in Table 6.2 range from 1.1MΩ to 40MΩ. Because of the narrow resonance resulting from the weak coupling of the HOMO level to the CNTs, a shift of the HOMO level results in a change in conductance. Therefore, the relative position of the HOMO level with respect to the contact Fermi level is important for quantitative conductance calculations. To determine the HOMO energy level, we proceed by calculating the IP and EA of molecule **1** and the image potential resulting from a hole on the molecule.

Table 6.2: Calculated resistance (R), full width at half max (Γ), and HOMO resonant position relative to the CNT Fermi level ($\Delta E = E_F - E_{HOMO}$) of the seven CNT-molecule-CNT systems studied where 'Planar' indicates the planar conformation of the molecule.

System	R (MΩ)	Γ (meV)	ΔE (meV)
Planar armchair, Fig. 6.1(a)	6.4	0.22	38
Planar zigzag, Fig. 6.4(a)	1.1	-	-
Planar 2 molecules, Fig. 6.6(a)	4.7	0.12	23
Planar carboxyl, Fig. 6.7(a)	40	0.023	14
Planar carboxyl, Fig. 6.7(b)	4.7	0.15	14
Planar carboxyl, Fig. 6.8(a)	32	0.61	1.59
Perpendicular, Fig. 6.9(a)	1590	-	-
Experimental (Ref. [67])	5	-	-

The transmission resonance widths of molecule **1** shown in Fig. 6.1(c), exhibit both time scales. The width of the HOMO resonance in Fig. 6.1(c) is 0.2 meV corresponding to a time $\tau = 3.2$ ps. The width of the LUMO resonance, on the other hand, is 0.25 eV corresponding to a time of 2.6 fs. Both the vertical and adiabatic IP and EA are calculated as described in Sec. 6.2.3 and the results are shown in Table 6.3.

As discussed in Sec. 6.2.3, DFT electron affinity predictions can be troublesome, but the evidence suggests that the EA results here are reasonable. First, starting from the more computationally affordable 6-31+G(d,p) basis set, we observe a negligible

0.001 eV shift in the EA upon adding a set of diffuse basis functions to the hydrogen atoms (6-31++G(d,p) basis). In addition, both basis sets give vertical EA values that lie within 0.08 eV of the larger 6-311+G(3df,2p) basis set results reported in Table 6.3. In problematic cases, much larger fluctuations in the EA are typically observed with increasing basis set size. Second, the EA value is fairly large and positive (1.60 eV for the vertical EA), indicating a tightly bound extra electron in the anion, and this electron resides in a valence anti-bonding π^* orbital that is delocalized primarily along the inter-CNT axis of the molecule. Therefore, we expect that the PBE EA values for this molecule are indeed reasonable.

Table 6.3: Calculated ionization potentials, electron affinities and HOMO-LUMO gaps of the planar molecule of Fig. 6.3 using PBE (GGA) and the 6-311+G(3df,2p) basis set [10]. Vacuum level resides at E=0 eV.

Type	IP (eV)	EA (eV)	Gap (eV))
Vertical	6.14	1.60	4.53
Adiabatic	6.03	1.40	4.63

Since, as we will show below, the conductance is mediated by the HOMO level, the adiabatic IP of 6.03 eV is the relevant one. For the LUMO resonance, the vertical EA of 1.60 eV listed in Table 6.3 is appropriate. The second vertical ionization potential for both same-spin and opposite-spin calculations is large at 15.02 and 15.17 eV, respectively.

We next calculate an image potential using the 22 nm armchair CNT-vacuum-CNT system, as described in Sec. 6.2.2. The DFT-RGF calculation gives an image potential of $\Phi_{CNT} = -0.7$ V. This is also the number obtained from the discretized charge cylinder calculation. There is also an image potential resulting from the discontinuity in the dielectric at the SiO_2 interface. The image potential due to a charge q in medium 1 a distance d above medium 2 is $\Phi_d = \frac{-q}{4\pi\epsilon_1(2d)}\frac{\epsilon_2-\epsilon_1}{\epsilon_2+\epsilon_1}$ where ϵ_1 and ϵ_2 are the dielectric constants in mediums 1 and 2, respectively. Letting medium 1 be air, medium 2 be SiO_2 with a relative dielectric constant of 3.9, and $d = 1$ nm, $\Phi_d = -0.43$ V. The two image potentials Φ_{CNT} and Φ_d should be calculated self-consistently, since the induced charge in the CNTs will affect the polarization of the dielectric and vice versa. As a zero order approximation we add the two values together and round down to estimate a total image potential of approximately -1 V. Converting to energy, this gives a +1 eV correction to the HOMO level obtained from the calculated IP. Adding this correction to the HOMO energy of -6.03 eV obtained from the adiabatic IP, we obtain a renormalized value for the HOMO energy of $E_{HOMO} = -5.0$ eV. To give a sense of the uncertainty in this estimate, recall that the absolute average (maximum) PBE errors in the calculation of the IP found in the study of small molecules was 0.16 eV (0.5 eV) [200].

Similarly, the CNT work function is not exactly known since experimentally measured values deviate by several hundred meV. The CNT work function is highly dependent on the type of CNTs, experimental conditions and the method of measurement used. Initial studies done using ultraviolet photoemission spectroscopy of single-walled CNT bundles yielded a work function of 4.8 eV [210]. Field emission microscopy techniques of single-wall CNT ropes give a work function at 5.1 eV [211]. Photoelectron spectroscopy measurements report work function values between 4.95 and 5.05 eV for CNT ropes [212]. Transmission electron microscope measurements of multi-walled CNTs report a work function between 4.6 and 4.8 eV [213]. Photoemission electron microscopy measurements of individual single-wall CNTs report 4.73 eV [214]. Recently, thermionic measurements of single-wall, double-wall and multiwall individual CNTs result in work functions of 4.7 - 4.9 eV [215]. All the experimental reports indicate that the CNT Fermi level most likely resides above the molecular HOMO energy, however exact work function measurments of individual single-wall CNTs deviate by as much 200 meV.

To determine which level, HOMO or LUMO, is mediating the transport, we consider the best and worst case alignments of the molecular levels with the CNT Fermi level, allowing the possible values of the CNT Fermi level to range from -5.0 to -4.7 eV. The calculated HOMO level is -5 ± 0.5 eV. Thus, the HOMO can lie in a range of energies from 0.8 eV below the CNT Fermi energy to 0.5 eV above the CNT Fermi energy. Starting with the EA of 1.6 eV and a -1 eV image potential, the renormalized LUMO is at -2.6 ± 0.3 eV using the maximum error from [200]. Therefore, the LUMO lies in a range of energies from 1.8 eV to 2.7 eV above the CNT Fermi energy. The best case alignment of the LUMO with the CNT Fermi energy is 1 eV further away than the worst case alignment of the HOMO with the CNT Fermi energy. Thus, it is overwhelmingly probable that the transport is mediated by the HOMO.

The calculations presented above indicate that the HOMO resonance is narrow both because it is spatially localized away from the leads and also because the amide linkers reduce coupling between the CNT π orbital and the HOMO of conjugated molecules. The HOMO resonance is also near the CNT Fermi level, but the exact position cannot be predicted accurately enough for quantitative transport calculations. Therefore, we now consider trends and show how the resonance position and width affect the resistance.

To do this, we imitate the experimental measurement conditions as closely as possible, and we consider an ideal Lorentzian transmission spectrum, $T(E) = \frac{\Gamma^2/4}{(E-E_{HOMO})^2+\Gamma^2/4}$. We vary the energetic position, E_{HOMO}, and the width, Γ, and plot out an equal-resistance contour in the Γ - E_{HOMO} plane corresponding to 5 MΩ. Experimentally, a 50 mV source-drain potential is applied while measuring the room temperature conductance [67]. The measured resistance of the pristine CNT is 1 MΩ, and the measured resistance of the CNT-molecule-CNT is 5 MΩ. Considering a simple voltage divider, and the weak, symmetric coupling of the molecule to the CNT leads, we

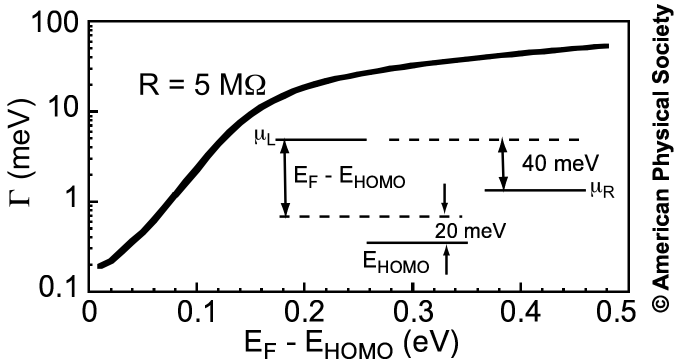

Figure 6.10: 5 MΩ equal resistance contour in the Γ - $(E_F - E_{HOMO})$ plane resulting from a Lorentzian transmission spectrum. (Inset) Position of the various energy levels used in the calculation.

assume that 40 mV is symmetrically dropped across the two molecule-CNT interfaces so that the energy of the HOMO level is dropped by 20 meV. Therefore, we reduce the equilibrium value of the HOMO level by 20 meV for the calculation of the current and resistance. The various energies are shown in the inset of Fig. 6.10. The $E_F - E_{HOMO}$ axis in Fig. 6.10 is the value before the bias is applied. The current is calculated using Eq. (2.11), and the resistance is then $R = 40\,\mathrm{mV}/I + 1\mathrm{M}\Omega$. Note that the resistances calculated in this manner will differ somewhat from those listed in Table 6.2 which were calculated by inverting the value obtained from Eq. (2.15). All resistances are calculated at $T = 300K$.

Fig. 6.10 shows the 5 MΩ equal-resistance contour in the Γ - $(E_F - E_{HOMO})$ plane. For a narrow resonance of 0.2 meV such as the ones that we obtain for many configurations, the resonance must be within 5 meV of the CNT Fermi energy. The width of a Lorentzian resonance lying 100 meV below the CNT Fermi level must be 2.2 meV to result in a 5 MΩ resistance. Such a width is at least a factor of 10 wider than that obtained for all of our structures with symmetric coupling.

Finally, we comment on the other type of resonance that we observed which was not Lorentzian. It was the quadruply split peak at the Fermi level resulting from the interaction of the zigzag surface states with the HOMO of the molecule shown in Fig. 6.5. For this system, the surface states are likely to be pinned at the Fermi level [151]. The molecular HOMO serves to mediate the coupling of the surface states. Thus, for this system, there will always be a transmission peak at the Fermi level, but the coupling will be reduced as the molecular HOMO level is moved further away in energy.

6.4 Summary

In summary, we have theoretically modeled transport of the first experimentally measured CNT-molecule-CNT system using DFT based approaches combined with NEGF to calculate the transmission spectrum, the ionization potential and the electron affinity of the molecule, and the image potential due to the proximity of the metallic CNT. CNT chirality, cut geometry, and end passivation were investigated. The features in the transmission correspond directly to the features of the isolated molecular orbitals and the surface states of the cut ends of zigzag CNTs. The HOMO resonance lying on the cross-arms of the planar molecule provides conductance at low bias that is qualitatively insensitive to the end groups of the cut CNTs, the CNT chirality, the cut angle, connection type or the number of molecular bridges. Quantitatively, however, these factors can modify the resonance width by an order of magnitude giving rise to corresponding changes in the resistance. Furthermore, the cut ends of a zigzag CNT can result in surface states which hybridize with the molecular HOMO state giving a large transmission peak at the Fermi level which results in a significant reduction in resistance (by a factor of 10 for the structures considered here). Calculations of the ionization potential and electron affinity strongly suggest that the conductance is mediated by the HOMO. However, there is a 0.5 eV uncertainty in the quantitative value of the calculated ionization potential. The uncertainty in the work function of the CNT is also larger than $7k_BT$ at room temperature. This uncertainty alone is large enough to prevent quantitative calculations of the current. Therefore, we treat the relative energy of the HOMO with respect to the CNT Fermi energy as a parameter. For all structures which exhibit no evidence of CNT surface states, there is a single resonant peak due to the molecular HOMO which mediates the hole transport. The calculated resonant width for all such structures with symmetric coupling between the leads is less than or equal to 0.22 meV. Approximating this resonance as a Lorentzian, the resonant peak must lie 5 meV below the CNT Fermi level to give a room temperature resistance of 5 MΩ. For the zigzag structure with CNT surface states pinned at the Fermi level, there will be a transmission peak at the Fermi level resulting from the surface states. Such a structure can have low resistance ($<$ 5 MΩ) even though the molecular HOMO level lies considerably further below the CNT Fermi energy.

Chapter 7

Recent Developments

7.1 Introduction

This chapter covers verification and testing of the Fireball/NEGF self-consistent field (SCF) implementation. Below lists the verification steps taken to achieve converged results. This chapter should be interpreted as a trial and error section to highlight the issues found when calculating the long-range Hartree component with non-equilibrium conditions. The below sections cover the approaches used, preliminary test cases and the current status of the model (June 2009).

7.2 Self-consistency

7.2.1 Long-range Hartree Potential - MUDPACK

As described in Chapter 2, the Fireball calculation incorporates a long-range Hartree potential due to the non-neutral components as described by Demkov et al. [37]. The charge density, (i.e. CHARGES) is mapped directly to the atom positions and summed over each valence core shell since there is no predefined real-space charge grid in FIREBALL. In this approach, the dipole expansion reduces the long-range calculation to a sum of two-center terms summable exactly by an Ewald summation using Von Neumann type boundary conditions. Since the potential floats at each boundary, I attempted to bypass this calculation in order to satisfy the non-equilibrium conditions required for transport modeling.

The long-range electrostatic calculation was first modified using a standard real-space (vacuum dielectric) mesh grid approach part of the GNU software package MUDPACK, version 5.0.1 [133]. MUDPACK is a collection of vectorized portable F77 subprograms which solve linear elliptic Partial Differential Equations (PDEs) using multigrid iterations. Multigrid iterations combines classical iterative techniques with subgrid refinement procedures [133]. The mudpack subroutines solve initially for the Laplacian solution, $\nabla^2\Phi = 0$, there Φ is the electrostatic potential calculated for a three-dimensional grid of ordered mesh points, spaced approximately 1 $\mathring{A}$ apart. The SCF process continues by computing a new potential from the Poisson solution, $\nabla^2\Phi = \frac{\rho}{\epsilon_0}$, given a new input charge density (ρ) from NEGF, at each grid point. This is done by computing a second order finite difference approximation for the 3D PDEs and specified boundary conditions.

Since the atom positions are not mapped directly to the grid points, a grid-to-atom and atom-to-grid approach was implemented using two approaches: 1) volumetric weighted sum of 3D boxes and 2) Gaussian type spheres. A weighted sum of volumes was used to map the potential defined on each grid point to the atoms. The volumes were setup using the cutoff distance from the atom to each grid point up to a maximum radius dictated by the wavefunction cutoff. Each volume incorporated a fraction of the potential by normalizing each point. The normalization was done by calculating the ratio of the inner volume to the total volume of circumscribing cube. This approach ensured the potential was mapped smoothly to each atom and the sum of all included weights did not exceed the potential contribution from all neighboring grid points. The potential value for each atom was then saved and ported into the NEGF subroutines self-consistently. Special care was taken to ensure that no buffer overruns and variable type conflicts existed between the F77 subroutines part of MUDPACK and the F90 routines of NEGF.

To map the non-neutral charge density calculated from NEGF back to the grid, a exponential function n_i mapped the density to each grid point i, at a distance r up to the predefined decay cutoff L_c: $n_i(r) = Ae^{-\frac{r}{L_c}}$. A is a normalization constant. This type of function mimicked the wavefuction response of a typical FIREBALL orbital where contributions are exponentially dependent on the radial distance. To calculate the normalization constant A for each grid point, the volume of the function was integrated. Each atomic contribution within the given cutoffs was summed onto each grid point throughout the entire mesh.

After five months of development and rigorous testing the charge density mapping approach was abandoned. The Laplacian calculation using MUDPACK, was retained for generating static non-equilibrium potential profiles for NEGF. CNT benchmark tests were unable to reproduce the equilibrium transmission spectra compared to a FIREBALL converged density, beginning with the neutral atom configuration. The transmissions all appeared erroneous and noisy after each converged calculation. The charge density never exactly matched the results from a standard FIREBALL self-consistent calculation. It was suspected that the mapping process of the charge density from the atoms to the grid did not capture the non-neutral component properly for input into the Poisson solution.

7.2.2 Boundary Conditions

After reverting back to the Demkov approach, it was determined that the floating potential at the boundaries prevented the equilibrium FIREBALL-NEGF SCF calculation from converging properly. The charge density and potential profile, returned from NEGF, would fluctuate rapidly across a CNT-molecule-CNT structure after each SCF step. Furthermore, the equilibrium NEGF calculated charge density at the first and last block layer of the contacts did not match a FIREBALL SCF converged result. The charge density discrepancy is due to a fundamental difference between FIREBALL's non-orthogonal basis set and the open-end treatment of the NEGF approach at the boundaries. All periodic structures defined in the FIREBALL space are setup such that the 'device' supercell region repeats infinitely using a non-orthogonal basis which create a Hamiltonian and overlap matrix that is block tri-diagonal. In NEGF, the left and right boundaries are assumed to have no overlap between the device region and the bulk contacts. The surface Green functions, used to model the semi-infinite leads, do not account for atomic interactions beyond the periodic boundaries. The charge density contributions from the blocks (off-diagonal blocks) neighboring the boundaries are not included in the NEGF implementation. This leaves the first and last unit cell block layers with an incorrect density and prevents a smooth converged solution.

In other well-known DFT-NEGF implementations [25,138,139] the charge density discrepancy at the boundaries is not covered, however techniques to resolve and treat the boundary conditions are discussed. I follow the same technique discussed in Ref. [139] where the charge density and potential, at atomic layers near the boundaries, are pinned to a bulk infinite/periodic solution. Using CNT leads, the first and last unit cells (4 atomic layers) charge densities are first pre-computed and saved from a FIREBALL-only run. The density is calculated from the atomic positions for each contact. After each FIREBALL-NEGF SCF step, the charge density at these regions is recalled and frozen using the bulk result. The corresponding diagonal matrix elements and coupling matrices from these pre-computed runs are also stored and recalled for the RGF algorithm. This effectively pins the potential at both semi-infinite leads to the bulk solution. To ensure the potential is fixed well into the device region, the first and last two block Hamiltonian matrices, $\mathbf{H}_{1,1}$, $\mathbf{H}_{2,2}$, $\mathbf{H}_{N-1,N-1}$, $\mathbf{H}_{N,N}$ are fixed. The corresponding coupling matrices (off-diagonal) which connect both sets of blocks $\mathbf{t}_{1,2}$, $\mathbf{t}_{2,1}$, $\mathbf{t}_{N-1,N}$ and $\mathbf{t}_{N,N-1}$ are also fixed and recalled during the RGF calculation. Corresponding overlap matrices $\mathbf{S}_{i,j}$, accompany each block matrix list above. The results section in this chapter will cover a test case using this approach.

7.2.3 Anderson Mixing

The Anderson mixing approach [216] in FIREBALL is used to exponentially converge the charge density during a self-consistent calculation. A normalization approach, part of FIREBALL, is used to correct round off errors after each mix. The normalization processes begins in the mixing subroutine where the total CHARGES are summed up and compared to the total number of neutral valence core electrons initialized (ztot) when FIREBALL starts. Once the difference is calculated, the remaining missing or excess charge is placed linearly on the newly mixed CHARGES array which is used in the next FIREBALL SCF step.

In order for non-equilibrium conditions to occur, the normalization process is bypassed and only implemented in the special case of an equilibrium (no bias) FIREBALL-NEGF SCF calculation. In an equilibrium FIREBALL-NEGF SCF run, the normalization process is only used in the first three steps. This dampens the over corrected

NEGF density during an initial run when starting from the neutral atom electron configuration. The normalization process cannot be used during the entire duration of a SCF FIREBALL-NEGF calculation since the NEGF calculation and resulting potential will artificially over correct for the excess/depleted charges added during each mixing process. This configuration best serves the NEGF density calculation and was verified after three months of trial and error.

7.2.4 Adaptive Energy Grid

To adequately integrate the energies between $\pm 10 k_B T$ from the Fermi energy, an adaptive energy grid algorithm is used to resolve any sharp transmission resonances/peaks. During testing, it was observed that a highly resolved energy grid was required when sweeping under the lowest Fermi pole for the complex contour integral. The resolved energy grid ensures the density is correctly calculated for a molecular system with states near the Fermi energy. To speed up the adaptive E grid process when calculating the transmission, each energy point is distributed for optimum load balancing over multiple processors (MPI-based). After each sweep of the energy window, a timer is reviewed for each slave process before starting a new sweep. Processes that are idle during the last energy sweep are balanced with extra energy points for the next sweep. This ensures that the master and slave processes have minimal idle times during the calculation.

7.3 Test Cases and Further Work

A test case is shown in this section to better illustrate the FIREBALL-NEGF SCF process and outlines other issues that needed to be addressed. Fig. 7.1 shows a truncated (periodic) section of a CNT-molecule-CNT structure composed of (5,5)

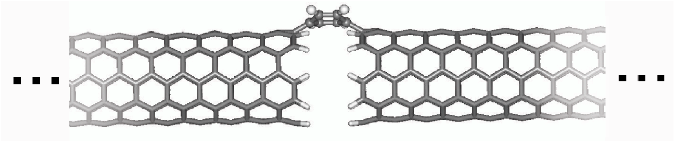

Figure 7.1: Relaxed CNT-benzene-CNT structure with armchair (5,5) CNT contacts.

armchair CNTs and a benzene ring attached covalently. The total structure is 23.7 nm in length and contains 1878 atoms. A truncated supercell about 5 nm in length is relaxed before the leads are extended.

An equilibrium FIREBALL-NEGF self-consistent calculation is done using a double numeric basis and compared to the results of Ref. [182]. To illustrate the convergence behavior, the potential profile for the system is shown in Fig. 7.2. Here SCF steps 5, 10, 15, 20 and 21 and 22 are shown, where the electrostatic profile is taken from a line oriented down the center of each CNT axis. The convergence criteria must be low for these large systems (at least 10^{-6}) to ensure the density is correct. At the boundaries the potential appears pinned and stable while the device region converges. I note here that the flow of charge is opposite compared to experimental observations. By flipping the potential profile upsidedown, ($V = -q(E_c - E_{ref})$ where E_c is the conduction band and E_{ref} is a reference energy) one can see that the CNT bands are positioned below the molecular level. This indicates the current is moving from the CNTs to the molecule which is incorrect. The FIREBALL HOMO and LUMO eigenvalues for a gas-phase molecule are also too shallow in reference to vaccum. This same trend is seen here using a CNT-molecule-CNT supercell. I find that changing from a single to a double numeric basis set with extended wavefuction cutoffs places the HOMO level lower however it does not correct the charge direction through the CNT-molecule-CNT supercell. Further tests and verification need to be done to rigidly shift the molecular levels down into the valence band such that the CNT

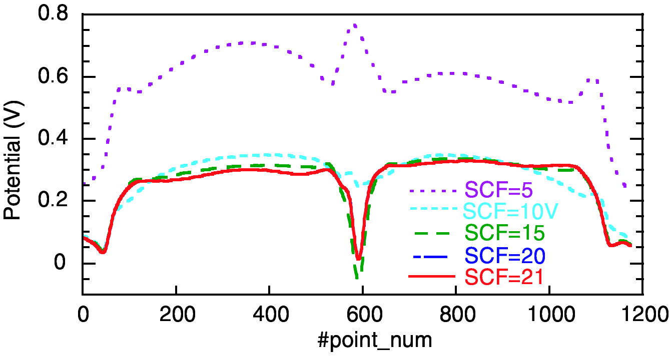

Figure 7.2: Potential profile for the system shown in Fig. 7.1 over a series of points down the axis of the CNT contacts.

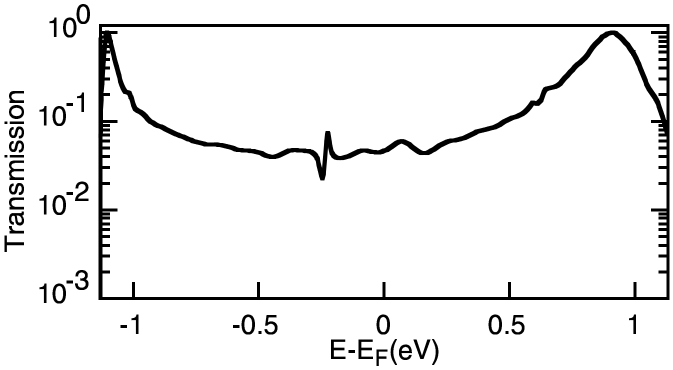

Figure 7.3: Calculated transmission of the armchair CNT-benzene-CNT structure.

Fermi level is positioned above the molecular HOMO state. This will ensure the current will flow correctly from the molecule to the CNTs.

Fig. 7.3 shows the self-consistent transmission spectra which matches closely to the SIESTA-NEGF self-consistent results published in Ref. [182]. This result is the first verification of a FIREBALL-NEGF SCF calculation. The HOMO and LUMO resonances can be seen spaced approximately 2 eV apart with the Fermi level near the center of the plot. The HOMO-LUMO level gap and alignment is much different compared to a FIREBALL gas-phase calculation which gives a HOMO-LUMO gap of 5 eV.

7.4 Summary

This chapter highlights the recent issues, solutions and tests used to develop the FIREBALL-NEGF approach. Initial results indicate the model is matching other DFT-NEGF studies, however much more rigorous testing is needed to verify results. Computational time on the clusters was limited and the non-equilibrium RGF algorithm could not be verified in time for this chapter. A new in-house Xeon cluster and cluster time on Nanohub should wrap up the final testing stages.

Chapter 8

Conclusion

A fast *ab-initio* modeling approach for calculating transport through inorganic/organic heterostructures has been implemented using non-equilibrium Green function (NEGF) within a density functional theory (DFT) application known as FIREBALL. The NEGF enhancements were divided into 4 stages. In the initial stage, the NEGF algorithm operated as a post-processor to FIREBALL. The second stage involved optimizing existing algorithms and adding parallel matrix inversion and multiplication processing for use on LATTE's Beowulf clusters. In the third stage, the NEGF package was added to the FIREBALL self-consistent loop. The fourth task was testing and verifying the calculations against semi-empirical/DFT-NEGF models and experimental data. Overarching all these stages was modeling support for CNT-molecule-CNT experimental efforts.

8.1 Summary

This dissertation has finished the first stage of a long term modeling effort aimed at studying the physics governing quantum transport through interfaces and heterostructures composed of CNTs, NWs, DNA/PNA and other inorganic/organic hybrid molecular systems. Despite the large amount of experimental activity in molecular electronics area, one finds little modeling activity in this area and little understanding of the charge and spin transport properties of the assembled bio/inorganic interfaces and heterostructures. This work begins to fill many theoretical and scientific needs. This highly efficient computational tool is capable of handling transport calculations of large organic/inorganic functionalized CNT and NW based devices and has allowed the LATTE group to provide theoretical support for several experimental studies.

The FIREBALL-NEGF project avoids many computational difficulties by using precomputed wavefunctions, a recursive Green function approach, a localized FIREBALL orbital basis and highly efficient parallel algorithms. The CNT-molecular device studies presented have predicted RTD type behavior for CNT-Mol-CNT systems, highlighted conductance trends dependent on the contact geometry and provided theoretical support and verification of an experimental CNT-molecule-CNT structure.

The FIREBALL-NEGF self-consistent approach has made much progress studying equilibrium transport, however additional testing is needed to accurately model non-equilibrium charge transport. To verify FIREBALL-NEGF calculations, experimental I-V responses of CNT based devices from collaborating labs will continue to be compared.

Bibliography

[1] N. Bruque, R. R. Pandey, R. Lake, H. Wang, and J. Lewis, "Electronic transport through a cnt-pseudopeptide-cnt hybrid material," *Molecular Simulation*, vol. 31, no. 12, pp. 859 – 864, 2005. [Online]. Available: dx.doi.org/10.1080/08927020500323879

[2] R. R. Pandey, N. Bruque, K. Alam, and R. Lake, "Carbon nanotube - molecular resonant tunneling diode," *Phys. Stat. Sol. (a)*, vol. 203, no. 2, pp. R5 – R7, 2006. [Online]. Available: http://dx.doi.org/10.1002/pssa.200521467

[3] X. Wang, F. Liu, G. T. S. Andavan, X. Jing, N. Bruque, R. R. Pandey, R. Lake, K. Singh, M. Ozkan, K. L. Wang, and C. S. Ozkan, "Carbon nanotube-dna nanoarchitectures and electronic functionality," *Small*, vol. 2, no. 11, pp. 1356 – 1365, 2006. [Online]. Available: dx.doi.org/10.1002/smll.200600056

[4] D. Shah, N. A. Bruque, K. Alam, R. K. Lake, and R. R. Pandey, "Electronic properties of carbon nanotubes calculated from density functional theory and the empirical π-bond model," *J. Computational Electronics*, vol. 6, no. 4, pp. 395 – 400, 2007. [Online]. Available: dx.doi.org/10.1007/s10825-007-0147-5

[5] N. A. Bruque, K. Alam, R. R. Pandey, R. K. Lake, J. P. Lewis, X. Wang, F. Liu, C. S. Ozkan, M. Ozkan, and K. L. Wang, "Self-assembled carbon nanotubes for electronic circuit and device applications," *J. Nanoelectronics Optoelectronics*, vol. 1, no. 1, pp. 74 – 81, 2006. [Online]. Available: http://dx.doi.org/10.1166/jno.2006.007

[6] N. A. Bruque, R. R. Pandey, and R. K. Lake, "Electron transport through a conjugated molecule with carbon nanotube leads," *Phys. Rev. B*, vol. 76, no. 20, p. 205322, 2007. [Online]. Available: http://dx.doi.org/10.1103/PhysRevB.76.205322

[7] N. A. Bruque, M. A. Ashraf, T. R. Helander, G. J. O. Beran, and R. K. Lake, "Conductance of a Conjugated Molecule with Carbon Nanotube Contacts," (resubmitted).

[8] From R. Lake, A. Balandin, M. Ozkan, C. Ozkan, R. Pandey, N. Bruque, and K. Alam, "Simulation of Self-Synthesized and Functionalized Devices,"

and from M. Ozkan, C. Ozkan, A. Balandin, and R. Lake, "Chemical and Biological Synthesis of Integrated Devices," presented at the MARCO FENA Center kickoff review, UCLA, March 8, 2004.

[9] T. B. Boykin, G. Klimeck, and F. Oyafuso, "Valence band effective-mass expressions in the $sp^3d^5s^*$ empirical tight-binding model applied to a si and ge parametrization," *Phys. Rev. B*, vol. 69, p. 115201, 2004.

[10] Y. Shao, L. F. Molnar, Y. Jung, J. Kussmann, C. Ochsenfeld, S. T. Brown, A. T. B. Gilbert, L. V. Slipchenko, S. V. Levchenko, D. P. O'Neill, R. A. DiStasio, Jr, R. C. Lochan, T. Wang, G. J. O. Beran, N. A. Besley, J. M. Herbert, C. Y. Lin, T. Van Voorhis, S. H. Chien, A. Sodt, R. P. Steele, V. A. Rassolov, P. E. Maslen, P. P. Korambath, R. D. Adamson, B. Austin, J. Baker, E. F. C. Byrd, H. Dachsel, R. J. Doerksen, A. Dreuw, B. D. Dunietz, A. D. Dutoi, T. R. Furlani, S. R. Gwaltney, A. Heyden, S. Hirata, C.-P. Hsu, G. Kedziora, R. Z. Khalliulin, P. Klunzinger, A. M. Lee, M. S. Lee, W. Z. Liang, I. Lotan, N. Nair, B. Peters, E. I. Proynov, P. A. Pieniazek, Y. M. Rhee, J. Ritchie, E. Rosta, C. D. Sherrill, A. C. Simmonett, J. E. Subotnik, H. L. Woodcock III, W. Zhang, A. T. Bell, A. K. Chakraborty, D. M. Chipman, F. J. Keil, A. Warshel, W. J. Hehre, H. F. Schaefer III, J. Kong, A. I. Krylov, P. M. W. Gill, and M. Head-Gordon, "Advances in methods and algorithms in a modern quantum chemistry program package," *Phys. Chem. Chem. Phys.*, vol. 8, pp. 3172–3191, 2006.

[11] E. Katz and I. Willner, "Integrated nanoparticle-biomolecule hybrid systems: Synthesis, properties, and applications," *Angew. Chem. Int. Ed.*, vol. 43, pp. 6042 – 6108, 2004.

[12] ——, "Biomolecule-functionalized carbon nanotubes: Applications in nanobioelectronics," *ChemPhysChem*, vol. 5, pp. 1085 – 1104, 2004.

[13] W. Fritzsche, Ed., *DNA-Based Molecular Electronics.* New York: AIP, 2004, vol. 725.

[14] S. S. Jang, Y. H. Jang, Y.-H. Kim, W. A. G. III, A. H. Flood, B. W. Laursen, H.-R. Tseng, J. F. Stoddart, J. O. Jeppesen, J. W. Choi, D. W. Steuerman, E. DeIonno, and J. R. Heath, "Structures and properties of self-assembled monolayers of bistable 2 rotaxanes on au (111) surfaces from molecular dynamics simulations validated with experiment," *J. Am. Chem. Soc.*, vol. 127, pp. 1563 – 1575, 2005.

[15] W.-Q. Deng, R. P. Muller, and W. A. Goddard, "Mechanism of the stoddart-heath bistable rotaxane molecular switch," *J. Am. Chem. Soc.*, vol. 126, pp. 13 562–13 563, 2004.

[16] Y. Xiao, F. Patolsky, E. Katz, J. F. Hainfeld, and I. Willner, “Plugging into enzymes: Nanowiring of redox enzymes by a gold nanoparticle,” *Science*, vol. 299, pp. 1877 – 1881, 2003.

[17] V. Pardo-Yissar, E. Katz, J. Wasserman, and I. Willner, “Acetylcholine esterase-labeled us nanoparticles on electrodes: Photoelectrochemical sensing of the enzyme inhibitors,” *J. Am. Chem. Soc.*, vol. 125, pp. 622 – 623, 2003.

[18] M. A. Reed, C. Zhou, C. J. Muller, T. P. Burgin, and J. M. Tour, “Conductance of a molecular junction,” *Science*, vol. 278, pp. 252 – 254, 1997.

[19] J. Taylor, M. Brandbyge, and K. Stokbro, “Theory of rectification in tour wires: the role of electrode coupling,” *Phys. Rev. Lett.*, vol. 89, no. 13, pp. 138 301/1–4, 2002.

[20] P. Damle, A. Ghosh, and S. Datta, “First-principles analysis of molecular conduction using quantum chemistry software,” *Chem. Phys.*, vol. 281, no. 2-3, pp. 171–188, 2002.

[21] H. Basch, R. Cohen, and M. A. Ratner, “Interface geometry and molecular junction conductance: Geometric fluctuation and stochastic switching,” *Nano Letters*, vol. 5, no. 9, pp. 1668–1675, 2005. [Online]. Available: http://dx.doi.org/10.1021/nl050702s

[22] P. Hohenberg and W. Kohn, “Inhomogeneous electron gas,” *Phys. Rev.*, vol. 136, pp. B864 – 871, 1964.

[23] O. F. Sankey and D. J. Niklewski, “Ab initio multicenter tight-binding model for molecular-dynamics simulations and other applications in covalent systems,” *Phys. Rev. B*, vol. 40, no. 6, pp. 3979 – 3995, 1989.

[24] J. Tomfohr and O. F. Sankey, “Theoretical analysis of electron transport through organic molecules,” *J. Chem. Phys.*, vol. 120, no. 3, pp. 1542 – 1554, 2004.

[25] M. Brandbyge, J.-L. Mozos, P. Ordejón, J. Taylor, and K. Stokbro, “Density functional method for nonequilibrium electron transport,” *Phys. Rev. B*, vol. 65, no. 16, p. 165401, 2002.

[26] J. Taylor, H. Guo, and J. Wang, “*Ab initio* modeling of quantum transport properties of molecular electronic devices,” *Phys. Rev. B*, vol. 63, no. 24, pp. 245 407/1–13, 2001.

[27] K. Stokbro, J. Taylor, M. Brandbyge, and P. Ordejon, “Transiesta - a spice for molecular electronics,” *Molecular Electronics III Ann. of the New York Acad. of Sci.*, vol. 1006, pp. 212–226, 2003.

[28] P. A. Derosa and J. M. Seminario, "Electron transport through single molecules: scattering treatment using density functional green function theories," *J. Phys. Chem. B*, vol. 105, no. 2, pp. 471–481, 2001.

[29] Y. Xue, S. Datta, and M. A. Ratner, "Charge transfer and "band lineup" in molecular electronic devices: A chemical and numerical interpretation," *J. Chem. Phys.*, vol. 115, no. 9, pp. 4292–4299, 2001.

[30] P. Damle, A. W. Ghosh, and S. Datta, "Unified description of molecular conduction: From molecules to metallic wires," *Phys. Rev. B*, vol. 64, no. 20, p. 201403, 2001.

[31] Y. Xue, S. Datta, and M. A. Ratner, "First-principles based matrix green's function approach to molecular electronic devices: general formalism," *Chemical Physics*, vol. 281, pp. 151–170, 2002.

[32] P. Damle, A. W. Ghosh, and S. Datta, "Unified description of molecular conduction: From molecules to metallic wires," *Phys. Rev. B*, vol. 64, p. 201403, 2001.

[33] T. Rakshit, G. Liang, A. Ghosh, and S. Datta, "Silicon-based molecular electronics," *Nano Lett.*, vol. 4, p. 1083, 2004. [Online]. Available: dx.doi.org/10.1021/nl049436t

[34] Y. Xue, S. Datta, and M. A. Ratner, "First-principles based matrix green's function approach to molecular electronic devices: general formalism," *Chem. Phys.*, vol. 281, no. 2-3, pp. 151–170, 2002.

[35] ——, "Charge transfer and band lineup in molecular electronic devices: A chemical and numerical interpretation," *J. Chem. Phys.*, vol. 115, no. 9, pp. 4292–4299, 2001.

[36] S. N. Yaliraki and M. A. Ratner, "Molecule-interface coupling effects on electronic transport in molecular wires," *J. Chem. Phys.*, vol. 109, no. 12, pp. 5036–5043, 1998.

[37] A. A. Demkov, J. Ortega, O. F. Sankey, and M. P. Grumbach, "Electronic structure approach for complex silicas," *Phys. Rev. B*, vol. 52, no. 3, pp. 1618 – 1630, 1995.

[38] O. F. Sankey, A. A. Demkov, W. Windl, J. H. Fritsch, J. P. Lewis, and M. Fuentes-Cabrera, "The application of approximate density functionals to complex systems," *Int. J. Quantum Chem.*, vol. 69, pp. 327 – 340, 1998.

[39] J. P. Lewis, K. R. Glaesemann, G. A. Voth, J. Fritsch, A. A. Demkov, J. Ortega, and O. F. Sankey, "Further developments in the local-orbital density-functional-theory tight-binding method," *Phys. Rev. B*, vol. 64, no. 19, p. 195103, 2001.

[40] H. Wang, J. P. Lewis, and O. F. Sankey, “Band-gap tunneling states in dna,” *Phys. Rev. Lett.*, vol. 93, no. 1, p. 016401, 2004.

[41] S. D. Shellman, J. P. Lewis, K. R. Glaesemann, K. Sikorski, and G. A. Voth, “Massively parallel linear-scaling algorithm in an ab initio local-orbital total-energy method,” *J. Comp. Phys.*, vol. 188, pp. 1 – 15, 2003.

[42] P. Jelinek, H. Wang, J. P. Lewis, O. F. Sankey, and J. Ortega, “Multicenter approach to the exchange-correlation interactions in ab initio tight-binding methods,” *Phys. Rev. B*, vol. 71, no. 23, p. 235101, 2005.

[43] ITRS 2007 Edition, Process Integration, Devices, and Structures.

[44] Y. Zheng and R. Lake, “Self-consistent transit-time model for a resonant tunnel diode,” *IEEE Trans. Elect. Dev.*, vol. 51, pp. 535–41, 2004.

[45] Y. Cui, X. Duan, J. Hu, and C. M. Lieber, “Doping and electrical transport in silicon nanowires,” *J. Phys. Chem. B*, vol. 104, no. 22, pp. 5213–6, 2000.

[46] J. Guo, S. Datta, M. Lundstrom, M. Brink, P. McEuen, A. Javey, H. Dai, H. Kim, and P. McIntyre, “Assessment of silicon mos and carbon nanotube fet performance limits using a general theory of ballistic transistors,” in *2002 IEDM Technical Digest.* New York: IEEE, Dec. 2002, pp. 711–714.

[47] J. Guo, S. Datta, and M. Lundstrom, “A numerical study of scaling issues for schottky-barrier carbon nanotube transistors,” *IEEE Trans. Elect. Dev.*, vol. 51, no. 2, pp. 172–177, 2004.

[48] C. A. Mirkin, R. L. Letsinger, R. C. Mucic, and J. J. Storhoff, “A dna-based method for rationally assembling nanoparticles into macroscopic materials,” *Nature*, vol. 382, pp. 607 – 609, 1996.

[49] A. P. Alivisatos, K. P. Johnsson, X. G. Peng, T. E. Wilson, C. J. Loweth, M. P. Bruchez, and P. G. Schultz, “Organization of nanocrystal molecules using dna,” *Nature*, vol. 382, pp. 609 – 611, 1996.

[50] K. Keren, R. S. Berman, E. Buchstab, U. Sivan, and E. Braun, “Dna-templated carbon nanotube field-effect transistor,” *Science*, vol. 302, pp. 1380 – 1382, 2003.

[51] C. Joachim and M. A. Ratner, “Molecular electronics: Some views on transport junctions and beyond,” *PNAS*, vol. 102, no. 25, pp. 8801–8808, 2005.

[52] N. J. Tao, “Electron transport in molecular junctions,” *Nature Nanotechnology*, vol. 1, pp. 173–181, 2006.

[53] R. Elghanian, J. J. Storhoff, R. C. Mucic, R. L. Letsinger, and C. A. Mirkin, "Selective colorimetric detection of polynucleotides based on the distance-dependent optical properties of gold nanoparticles," *Science*, vol. 277, pp. 1078 – 1081, 1997.

[54] I. Willner, F. Patolsky, and J. Wasserman, "Photoelectrochemistry with controlled dna-cross-linked cds nanoparticle arrays," *Angewandte Chemie-International Edition*, vol. 40, pp. 1861 – 1864, 2001.

[55] F. Patolsky, R. Gill, Y. Weizmann, T. Mokari, U. Banin, and I. Willner, "Lighting-up the dynamics of telomerization and dna replication by cdse-zns quantum dots," *J. Am. Chem. Soc.*, vol. 125, pp. 13 918–13 919, 2003.

[56] E. R. Goldman, E. D. Balighian, H. Mattoussi, M. K. Kuno, J. M. Mauro, P. T. Tran, and G. P. Anderson, "Avidin: A natural bridge for quantum dot-antibody conjugates," *J. Am. Chem. Soc.*, vol. 124, pp. 6378 – 6382, 2002.

[57] S. R. Whaley, D. S. English, E. L. Hu, P. F. Barbara, and A. M. Belcher, "Selection of peptides with semiconductor binding specificity for directed nanocrystal assembly," *Nature*, vol. 405, pp. 665 – 668, 2000.

[58] E. Braun and K. Keren, "From dna to transistors," *Adv. Phys.*, vol. 53, no. 4, pp. 441 – 496, 2004.

[59] C. Dwyer, V. Johri, M. Cheung, J. Patwardhan, A. Lebeck, and D. Sorin, "Design tools for a dna-guided self-assembling carbon nanotube technology," *Nanotechnology*, vol. 15, pp. 1240 – 1245, 2004.

[60] U. Sivan, K. Keren, E. Braun, R. Berman, and E. Buchstab, "Transistor in a test tube - harnessing molecular biology to the self-assembly of molecular scale electronics," in *Proceedings of the IEDM*. New York: IEEE, 2004, pp. 8.2.1 – 8.2.4.

[61] K. A. Williams, P. T. M. Veenhuizen, B. G. de la Torre, R. Eritja, and C. Dekker, "Carbon nanotubes with dna recognition," *Nature*, vol. 420, p. 761, 2002.

[62] R. den Dulk, K. A. Williams, P. T. M. Veenhuizen, M. C. de Konig, M. Overhand, and C. Dekker, "Self-assembly experiments with pna-derivatized carbon nanotubes," in *DNA-Based Molecular Electronics*, W. Fritzsche, Ed., vol. 725. New York: AIP, 2004, pp. 25 – 31.

[63] K. V. Singh, X. Wang, R. R. Pandey, R. Lake, C. Ozkan, and M. Ozkan, "Functionally engineered carbon nanotube - peptide nucleic acid bio conjugates for molecular electronics in micro and nanosystems-materials and devices," *Mater. Res. Soc. Symp. Proc.*, vol. 872, p. J13.7.1, 2005.

[64] X. Wang, K. Singh, C. Tsai, R. K. Lake, A. A. Balandin, M. Ozkan, and C. Ozkan, “Oligonucleotide metallization for conductive bio-inorganic interfaces in self assembled nanoelectronics and nanosystems,” *Mater. Res. Soc. Symp. Proc.*, vol. 872, p. J10.2.1, 2005.

[65] X. Wang, R. R. Pandey, K. V. Singh, G. T. S. Andavan, C. Tsai, R. Lake, M. Ozkan, and C. S. Ozkan, “Synthesis and characterization of peptide nucleic acid - platinum complexes,” *Nanotechnology*, vol. 17, pp. 1177 – 1183, 2006.

[66] K. V. Singh, R. R. Pandey, X. Wang, R. Lake, C. S. Ozkan, and M. Ozkan, “Covalent functionalization of single walled carbon nanotubes with peptide nucleic acid: Nanocomponents for molecular level electronics,” *Carbon*, vol. 44, no. 9, pp. 1730 – 1739, 2006. [Online]. Available: http://dx.doi.org/10.1016/j.carbon.2005.12.048

[67] X. Guo, J. P. Small, J. E. Klare, Y. Wang, M. S. Purewal, I. W. Tam, B. H. Hong, R. Caldwell, L. Huang, S. O’Brien, J. Yan, R. Breslow, S. J. Wind, J. Hone, P. Kim, and C. Nuckolls, “Covalently bridging gaps in single-walled carbon nanotubes with conducting molecules,” *Science*, vol. 311, no. 5759, pp. 356 – 359, 2006. [Online]. Available: http://www.sciencemag.org/cgi/content/abstract/311/5759/356

[68] B. Messer, J. H. Song, and P. Yang, “Microchannel networks for nanowire patterning,” *J. Am. Chem. Soc.*, vol. 122, pp. 10 232–33, 2000.

[69] Y. Cui and C. M. Lieber, “Functional nanoscale electronic devices assembled using silicon nanowire building blocks,” *Science*, vol. 291, pp. 851–3, 2002.

[70] E. Joselevich and M. Lieber, “Vectorial growth of metallic and semiconducting single-wall carbon nanotubes,” *Nano Lett.*, vol. 2, pp. 1137–1141, 2002.

[71] L. A. Nagahara, I. Amlani, J. Lewenstein, and R. K. Tsui, “Directed placement of suspended carbon nanotubes for nanometer-scale assembly,” *Appl. Phys. Lett.*, vol. 80, pp. 3826–3828, 2002.

[72] N. Melosh, A. Boukai, B. G. F. Diana, A. Badolato, P. M. Petroff, and J. Heath, “Ultrahigh-density nanowire lattices and circuits,” *Science*, vol. 300, pp. 112–115, 2003.

[73] M. Artemyev, B. Moller, and U. Woggon, “Unidirectional alighment of cdse nanorods,” *Nano Lett.*, vol. 3, pp. 509–512, 2003.

[74] Y.-C. Tseng, P. Xuan, A. Javey, R. Malloy, Q. Wang, J. Bokor, and H. Dai, “Monolithic integration of carbon nanotube devices with silicon mos technology,” *Nano Lett.*, vol. 4, no. 1, pp. 123–127, 2004.

[75] S. Han, X. Liu, and C. Zhou, “Template-free directional growth of single-walled carbon nanotubes on a- and r-plane sapphire,” *J. Am. Chem. Soc. Comm.*, vol. 127, pp. 5294–5, 2005.

[76] X. Liu, S. Han, and C. Zhou, “Novel nanotube-on-insulator (noi) approach toward single-walled carbon nanotube devices,” *Nano Lett.*, vol. 6, no. 1, pp. 34–39, 2006.

[77] S. Ravindran, S. Chaudhary, B. Colburn, M. Ozkan, and C. Ozkan, “Covalent coupling of quantum dots to multiwalled carbon nanotubes for electronic device applications,” *Nano Lett.*, vol. 3, no. 4, pp. 447 – 454, 2003.

[78] R. M. Stoltenberg and A. T. Woolley, “Dna-templated nanowire fabrication,” *Biomedical Microdevices*, vol. 6, no. 2, pp. 105 – 111, 2004.

[79] K. Keren, R. S. Berman, and E. Braun, “Patterned dna metallization by sequence-specific localization of a reducing agent,” *Nano Lett.*, vol. 4, no. 2, pp. 323 – 326, 2004.

[80] A. Javey, J. Guo, Q. Wang, M. Lundstrom, and H. Dai, “Ballistic carbon nanotube field-effect transistors,” *Nature*, vol. 424, pp. 654–657, 2003.

[81] A. Javey, J. Guo, M. Paulsson, Q. Wang, D. Mann, M. Lundstrom, and H. Dai, “High-field quasiballistic transport in short carbon nanotubes,” *Phys. Rev. Lett.*, vol. 92, no. 10, p. 106804, 2004.

[82] A. Javey, J. Guo, D. B. Farmer, Q. Wang, D. Wang, R. G. Gordon, M. Lundstrom, and H. Dai, “Carbon nanotube field-effect transistors with integrated ohmic contacts and high-κ gate dielectrics,” *Nano Lett.*, vol. 4, no. 3, pp. 447–450, 2004.

[83] A. Javey, J. Guo, D. B. Farmer, Q. Wang, E. Yenilmez, R. G. Gordon, M. Lundstrom, and H. Dai, “Self-aligned ballistic molecular transistors and electrically parallel nanotube arrays,” *Nano Lett.*, vol. 4, no. 7, pp. 1319–1322, 2004.

[84] Z. Chen, J. Appenzeller, J. Knoch, Y.-M. Lin, and P. Avouris, “The role of metal-nanotube contact in the performance of carbon nanotube field-effect transistors,” *Nano Lett.*, vol. 5, no. 7, pp. 1497 – 1502, 2005.

[85] W. Kim, A. Javey, R. Tu, J. Cao, Q. Wang, and H. Dai, “Electrical contacts to carbon nanotubes down to 1 nm in diameter,” *Appl. Phys. Lett.*, vol. 87, p. 173101, 2005.

[86] N. C. Seeman, “Dna in a material world,” *Nature*, vol. 421, pp. 427 – 431, 2003.

[87] H. Yan, S. H. Park, G. Finkelstein, J. H. Reif, and T. H. LaBean, “Dna-templated self-assembly of protein arrays and highly conductive nanowires,” *Science*, vol. 301, no. 5641, pp. 1882 – 1884, 2003.

[88] S. H. Park, C. Pistol, S. J. Anh, J. H. Reif, A. R. Lebeck, C. Dwyer, and T. H. LaBean, *Angewandte Chemie-Int. Ed.*, vol. 45, no. 5, pp. 735 – 739, 2006.

[89] A. Dehon, “Array-based architecture for fet-based, nanoscale electronics,” *IEEE Trans. Nanotechnology*, vol. 2, no. 1, pp. 23 – 32, 2003.

[90] G. Snider, P. Kuekes, and R. S. Williams, “Cmos-like logic in defective, nanoscale crossbars,” *Nanotechnology*, vol. 15, pp. 881 – 891, 2004.

[91] R. Beckman, E. Johnston-Halperin, Y. Luo, J. E. Green, and J. R. Heath, “Bridging dimensions: demultiplexing ultrahigh-density nanowire circuits,” *Science*, vol. 310, pp. 465 – 468, 2005.

[92] X. Zhang, L. Fonseca, and A. A. Demkov, “The application of density functional, local orbitals, and scattering theory to quantum transport,” *phys. stat. sol. (b)*, vol. 233, no. 1, pp. 70–82, 2002.

[93] J. M. Seminario, L. E. Cordova, and P. A. Derosa, “An *ab initio* approach to the calculation of current-voltage characteristics of programmable molecular devices,” *Proc. IEEE*, vol. 91, no. 11, pp. 1958–1975, 2003.

[94] Y. Xue and M. A. Ratner, “Microscopic study of electrical transport through individual molecules with metallic contacts. i. band lineup, voltage drop, and high-field transport,” *Phys. Rev. B*, vol. 68, no. 11, p. 115406, 2003.

[95] M. A. Reed, J. Chen, A. M. Rawlett, D. W. Price, and J. M. Tour, “Molecular random access memory cell,” *Appl. Phys. Lett.*, vol. 78, no. 23, pp. 3735–3737, 2001.

[96] R. F. Service, “Next-generation technology hits an early midlife crisis,” *Science*, vol. 302, pp. 556 – 558, 2003.

[97] Y. Xue and M. A. Ratner, “End group effect on electrical transport through individual molecules: A microscopic study,” *Phys. Rev. B*, vol. 69, p. 085403, 2004.

[98] F. Evers, F. Weigend, and M. Koentopp, “Conductance of molecular wires and transport calculations based on density-functional theory,” *Phys. Rev. B*, vol. 69, no. 23, pp. 235 411/1–9, 2004.

[99] R. A. Kiehl, J. D. Le, P. Candra, R. C. Hoye, and T. R. Hoye, “Charge storage model for hysteretic negative-differential resistance in metal-molecule-metal junctions,” *Appl. Phys. Lett.*, vol. 88, no. 17, p. 172102, 2006. [Online]. Available: http://dx.doi.org/10.1063/1.2195696

[100] R. Liu, S.-H. Ke, H. U. Baranger, and W. Yang, “Negative differential resistance and hysteresis through an organometallic negative differential resistance and hysteresis through an organometallic,” *J. Am. Chem. Soc.*, vol. 128, pp. 6274 – 6275, 2006. [Online]. Available: 10.1021/ja057054z

[101] S. M. Lindsay and M. A. Ratner, “Molecular transport junctions: Clearning mists,” *Adv. Mater.*, vol. 19, pp. 23–31, 2007.

[102] J. Tomfohr, G. K. Ramachandran, O. F. Sankey, and S. M. Lindsay, *Making Contacts to Single Molecules: Are We There Yet?* in *Introducing Molecular Electronics, Lecture Notes in Physics.* New York: Springer, 2005, vol. 680, pp. 301 – 312.

[103] L. Venkataraman, J. E. Klare, C. Nuckolls, M. S. Hybertsen, and M. L. Steigerwald, “Dependence of single-molecule junction conductance on molecular conformation,” *Nature*, vol. 442, pp. 904 – 907, 2006. [Online]. Available: dx.doi.org/10.1038/nature05037

[104] L. Venkataraman, J. E. Klare, I. W. Tam, C. Nuckolls, M. S. Hybertsen, and M. L. Steigerwald, “Single-molecule circuits with well-defined molecular conductance,” *Nano Lett.*, vol. 6, no. 3, pp. 458–462, 2006. [Online]. Available: dx.doi.org/10.1021/nl052373+

[105] Z. Li and D. S. Kosov, “Nature of well-defined conductance of amine-anchored molecular junctions: Density functional calculations,” *Phys. Rev. B*, vol. 76, p. 035415, 2007. [Online]. Available: dx.doi.org/10.1103/PhysRevB.76.035415

[106] L. Venkataraman, Y. S. Park, A. C. Whalley, C. Nuckolls, M. S. Hybertsen, and M. L. Steigerwald, “Electronics and chemistry: Varying single-molecule junction conductance using chemical substituents,” *Nano Lett.*, vol. 7, pp. 502 – 506, 2007.

[107] M. S. Hybertsen, L. Venkataraman, J. E. Klare, A. C. Whalley, M. L. Steigerwald, and C. Nuckolls, “Amine-linked single-molecule circuits: systematic trends across molecular families,” *J. Phys.: Condens. Matter*, vol. 20, p. 374115, 2008.

[108] N. P. Guisinger, R. Basu, A. S. Baluch, and M. C. Hersam, “Molecular electronics on silicon: An ultrahigh vacuum scanning tunneling microscopy study,” *Annals of the New York Academy of Sciences*, vol. 1006, pp. 227 – 234, 2003. [Online]. Available: doi:10.1196/annals.1292.015

[109] W. Wang, T. Lee, M. Kamdar, M. A. Reed, M. P. Stewart, J. J. Hwang, and J. Tour, “Electrical characterization of metalmoleculesilicon junctions,” *Superlatt. Microstruc.*, vol. 33, pp. 217–226, 2003.

[110] N. P. Guisinger, M. E. Greene, R. Basu, A. S. Baluch, and M. C. Hersam, “Room temperature negative differential resistance through individual organic molecules on silicon surfaces,” *Nano Lett.*, vol. 4, no. 1, pp. 55 – 59, 2004.

[111] T. Rakshit, C.-G. Liang, A. W. Ghosh, M. C. Hersam, and S. Datta, “Molecules on silicon: Self-consistent first-principles theory and calibration to experiments,” *Phys. Rev. B*, vol. 72, no. 12, p. 125305, 2005.

[112] W. Lu, V. Meunier, and J. Bernholc, “Nonequilibrium quantum transport properties of organic molecules on silicon,” *Phys. Rev. Lett.*, vol. 95, no. 20, p. 206805, 2005. [Online]. Available: dx.doi.org/10.1103/PhysRevLett.95.206805

[113] S. Lenfant, D. Guerin, F. T. Van, C. Chevrot, S. Palacin, J. P. Bourgoin, O. Bouloussa, F. Rondelez, and D. Vuillaume, “Electron transport through rectifying self-assembled monolayer diodes on silicon: Fermi-level pinning at the molecule-metal interface,” *J. Phys. Chem. B*, vol. 110, no. 28, pp. 13 947 – 13 958, 2006.

[114] J. He, B. Chen, A. K. Flatt, J. J. Stephenson, C. D. Doyle, and J. M. Tour, “Metal-free silicon-molecule-nanotube testbed and memory device,” *Nature. Mater.*, vol. 5, pp. 63–68, 2006.

[115] S. Y. Quek, J. B. Neaton, M. S. Hybertson, E. Kaxiras, and S. G. Louie, “Negative differential resistance in transport through organic molecules on silicon,” *Phys. Rev. Lett.*, vol. 98, no. 6, p. 066807, 2007.

[116] W. Ren, J. R. Reimers, N. S. Hush, Y. Zhu, J. Wang, and H. Guo, “Models for the structure and electronic transmission of carbon nanotubes covalently linked by a molecular bridge via amide couplings,” *J. Phys. Chem. C*, vol. 111, pp. 3700 – 3704, 2007.

[117] M. Valle, R. Gutierrez, C. Tejedor, and G. Cuniberti, “Tuning the conductance of a molecule switch,” *Nature Nanotech.*, vol. 2, pp. 176–79, 2007.

[118] P. Damle, T. Rakshit, M. Paulsson, and S. Datta, “Current-voltage characteristics of molecular conductors: two versus three terminal,” *IEEE Trans. Nanotech.*, vol. 1, no. 3, pp. 145 – 153, 2002.

[119] G. C. Liang, A. W. Ghosh, M. Paulsson, and S. Datta, “Electrostatic potential profiles of molecular conductors,” *Phys. Rev. B*, vol. 69, p. 115302, 2004. [Online]. Available: dx.doi.org/10.1103/PhysRevB.69.115302

[120] P. Qi, A. Javey, M. Rolandi, Q. Wang, E. Yenilmez, and H. Dai, "Miniature organic transistors with carbon nanotubes as quasi-one-dimensional electrodes," *J. Am. Chem. Soc.*, vol. 126, pp. 11 774 – 11 775, 2004.

[121] A. Dehon, "Nanowire-based programmable architectures," *J. Emerg. Technol. Comput. Syst.*, vol. 1, no. 2, pp. 109–162, 2005.

[122] G. Cuniberti, G. Fagas, and K. Richter, Eds., *Introducing Molecular Electronics*, ser. Lecture Notes in Physics. Berlin Heidelberg: Springer, 2005, vol. 680. [Online]. Available: DOI 10.1007/b101525

[123] V. V. Zhirnov and R. K. Calvin, "Chemistry of molecules or physics," *Nature. Mater.*, vol. 5, pp. 11–12, 2006.

[124] M. J. Frisch, G. W. Trucks, H. B. Schlegel, G. E. Scuseria, M. A. Robb, J. R. Cheeseman, J. A. Montgomery, Jr., T. Vreven, K. N. Kudin, J. C. Burant, J. M. Millam, S. S. Iyengar, J. Tomasi, V. Barone, B. Mennucci, M. Cossi, G. Scalmani, N. Rega, G. A. Petersson, H. Nakatsuji, M. Hada, M. Ehara, K. Toyota, R. Fukuda, J. Hasegawa, M. Ishida, T. Nakajima, Y. Honda, O. Kitao, H. Nakai, M. Klene, X. Li, J. E. Knox, H. P. Hratchian, J. B. Cross, V. Bakken, C. Adamo, J. Jaramillo, R. Gomperts, R. E. Stratmann, O. Yazyev, A. J. Austin, R. Cammi, C. Pomelli, J. W. Ochterski, P. Y. Ayala, K. Morokuma, G. A. Voth, P. Salvador, J. J. Dannenberg, V. G. Zakrzewski, S. Dapprich, A. D. Daniels, M. C. Strain, O. Farkas, D. K. Malick, A. D. Rabuck, K. Raghavachari, J. B. Foresman, J. V. Ortiz, Q. Cui, A. G. Baboul, S. Clifford, J. Cioslowski, B. B. Stefanov, G. Liu, A. Liashenko, P. Piskorz, I. Komaromi, R. L. Martin, D. J. Fox, T. Keith, M. A. Al-Laham, C. Y. Peng, A. Nanayakkara, M. Challacombe, P. M. W. Gill, B. Johnson, W. Chen, M. W. Wong, C. Gonzalez, and J. A. Pople, *Gaussian 03, Revision C.02*, 2003, Gaussian, Inc., Wallingford, CT, 2004.

[125] J. Harris, "Simplified method for calculating the energy levels of weakly interacting fragments," *Phys. Rev. B*, vol. 31, pp. 1770–1779, 1985.

[126] W. M. C. Foulkes and R. Haydock, "Tight-binding models and density-functional theory," *Phys. Rev. B*, vol. 39, pp. 12 520–2536, 1989.

[127] D. R. Hamann, "Generalized norm-conserving pseudopotentials," *Phys. Rev. B*, vol. 40, no. 5, pp. 2980 – 2987, 1989.

[128] J. L. Martins, N. Troullier, and S. H. Wei, "Pseudopotential plane-wave calculations for zns," *Phys. Rev. B*, vol. 43, no. 3, pp. 2213 – 2217, 1991.

[129] A. P. Horsfield, "Efficient ab initio tight binding," *Phys. Rev. B*, vol. 56, no. 11, pp. 6594–602, 1997.

[130] C. Lee, W. Yang, and R. G. Parr, "Development of the colle-salvetti correlation energy formula into a functional of the electron density," *Phys. Rev. B*, vol. 37, no. 2, pp. 785 – 789, 1988.

[131] M. Galperin, S. Toledo, and A. Nitzan, "Numerical computation of tunneling fluxes," *J. Chem. Phys.*, vol. 117, pp. 10 817–10 826, 2002.

[132] M. P. L. Sancho, J. M. L. Sancho, and J. Rubio, "Highly convergent schemes for the calculation of bulk and surface green functions," *J. Phys. F*, vol. 15, pp. 851–858, 1985.

[133] http://www.cisl.ucar.edu/css/software/mudpack/.

[134] R. Lake, G. Klimeck, R. C. Bowen, and D. Jovanovic, "Single and multiband modeling of quantum electron transport through layered semiconductor devices," *J. Appl. Phys.*, vol. 81, no. 12, pp. 7845–7869, 1997.

[135] D. Lohez and M. Lannoo, "Generalization of the green's-functions formalism to nonorthogonal orbitals: Application to amorphous sio_2," *Phys. Rev. B*, vol. 27, no. 8, pp. 5007–5011, 1983.

[136] R. S. Mulliken, "Electronic population analysis on lcao-mo molecular wave functions. i," *J. Chem. Phys.*, vol. 23, no. 10, pp. 1833 – 1840, 1955.

[137] P. O. Löwdin, "On the non-orthogonality problem connected with the use of atomic wave functions in the theory of molecules and crystals," *J. Chem. Phys.*, vol. 18, no. 3, pp. 365–375, 1950.

[138] A. D. Carlo, A. Pecchia, L. Latessa, T. Frauenheim, and G. Seifert, *Tight-Binding DFT for Molecular Electronics (gDFTB)* in *Introducing Molecular Electronics, Lecture Notes in Physics.* New York: Springer, 2005, vol. 680, pp. 153 – 184.

[139] A. R. Rocha, V. M. Garcia-Suarez, S. Bailey, C. Lambert, F. Ferrer, and S. Sanvito, "Spin and molecular electronics in atomically generated orbital landscapes," *Phys. Rev. B*, vol. 73, p. 085414, 2006.

[140] R. M. Martin, *Electronic Structure Basic Theory and Practical Methods.* Cambridge: Cambridge University Press, 2004.

[141] J. W. Mintmire, D. H. Robertson, and C. T. White, "Properties of fullerene nanotubules," *J. Phys. Chem. Solids*, vol. 54, no. 12, pp. 1835–1840, 1993.

[142] C. Adessi, S. Roche, and X. Blase, "Reduced backscattering in potassium-doped nanotubes: Ab initio and semiempirical simulations," *Phys. Rev. B*, vol. 73, p. 125414, 2006. [Online]. Available: dx.doi.org/10.1103/PhysRevB.73.125414

[143] N. D. Lang, "Negative differential resistance at atomic contacts," *Phys. Rev. B*, vol. 55, no. 15, pp. 9364–9366, 1997.

[144] W. Tian, S. Datta, S. Hong, R. Reifenberger, J. I. Henderson, and C. P. Kubiak, "Conductance spectra of molecular wires," *J. Chem. Phys.*, vol. 109, no. 7, pp. 2874–2882, 1998.

[145] G. Fagas, G. Cuniberti, and K. Richter, "Electron transport in nanotube-molecular-wire hybrids," *Phys. Rev. B*, vol. 63, no. 4, p. 045416, 2001.

[146] F. Remacle, J. R. Heath, and R. D. Levine, "Electrical addressing of confined quantum systems for quasiclassical computation and finite state logic machines," *Proc. Nat. Acad. Sci.*, vol. 102, no. 16, pp. 5653 – 5658, 2005.

[147] Y. Chen, G.-Y. Jung, D. A. A. Ohlberg, X. Li, D. R. Stewart, J. O. Jeppesen, K. A. Nielsen, J. F. Stoddart, and R. S. Williams, "Nanoscale molecular-switch crossbar circuits," *Nanotechnology*, vol. 14, pp. 462–468, 2003.

[148] M. T. Bjork, B. J. Ohlsson, C. Thelander, A. I. Persson, K. Deppert, L. R. Wallenberg, and L. Samuelson, "Nanowire resonant tunneling diodes," *Appl. Phys. Lett.*, vol. 81, no. 23, pp. 4458 – 4460, 2002.

[149] L. J. Lauhon, M. S. Gudiksen, and C. M. Lieber, "Semiconductor nanowire heterostructures," *Phil. Trans. R. Soc. Lond. A*, vol. 362, pp. 1247 – 1260, 2004.

[150] *PCMODEL Version 9.00.0*, serena Software, 2004.

[151] F. Buonocore, F. Trani, D. Ninno, A. D. Matteo, G. Cantele, and G. Iadonisi, "Ab initio calculations of electron affinity and ionization potential of carbon nanotubes," *Nanotechnology*, vol. 19, p. 025711, 2008.

[152] K. Alam and R. K. Lake, "Performance of 2 nm gate length carbon nanotube field-effect transistors with source/drain underlaps," *Appl. Phys. Lett.*, vol. 87, no. 7, p. 073104, 2005.

[153] P. A. Derosa, S. Guda, and J. M. Seminario, "A programmable molecular diode driven by charge-induced conformational changes," *J. Am. Chem. Soc.*, vol. 125, no. 47, pp. 14 240–1, 2003.

[154] T. P. E. Broekaert, B. Brar, J. P. A. van der Wagt, A. C. Seabaugh, F. J. Morris, T. S. Moise, E. A. B. III, and G. A. Frazier, "A monolithic 4-bit 2gsps resonant tunneling analog-to-digital converter," *IEEE J. Solid State Circuits*, vol. 33, no. 9, pp. 1342 – 1349, 1998.

[155] A. Seabaugh, X. Deng, T. Blake, B. Brar, T. Broekaert, R. Lake, F. Morris, and G. Frazier, "Transistors and tunnel diodes for analog/mixed-signal circuits and embedded memory," in *1998 IEDM Technical Digest.* New York: IEEE, 1998, pp. 429–432.

[156] L. Ding and P. Mazumder, "Noise tolerant quantum mos circuits using resonant tunneling diodes," *IEEE Trans. Nanotech.*, vol. 3, no. 1, pp. 134 – 146, 2004.

[157] A. D. Becke, "Density-functional thermochemistry - iii. the role of exact exchange," *J. Chem. Phys.*, vol. 98, no. 7, p. 5648, 1993.

[158] G. Cuniberti, F. Grobmann, and R. Gutierrez, "The role of contacts in molecular electronics," *Adv. Solid State Phys.*, vol. 42, pp. 133–149, 2002.

[159] F. Maseras and K. Morokuma, "Imomm: A new integrated ab initio + molecular mechanics geometry optimization scheme of equilibrium structures and transition states," *J. Comp. Chem.*, vol. 16, pp. 1170–1179, 1995.

[160] S. Humbel, S. Sieber, and K. Morokuma, "The imomo method: Integration of different levels of molecular orbital approximations for geometry optimization of large systems: Test for n-butane conformation and sn^2 reaction: Rcl + cl^-," *J. Chem. Phys.*, vol. 105, pp. 1959–1967, 1996.

[161] T. Matsubara, S. Sieber, , and K. Morokuma, "A test of the new integrated mo + mm (imomm) method for the conformational energy of ethane and n-butane," *Int. J. Quant. Chem.*, vol. 60, pp. 1101–1109, 1996.

[162] M. Svensson, S. Humbel, R. Froese, T. Matsubara, S. Sieber, and K. Morokuma, "Oniom: A multilayered integrated mo + mm method for geometry optimizations and single point energy predictions. a test for diels-alder reactions and $\mathrm{pt(p(}t\mathrm{\text{-}bu)_3)_2 + h_2}$ oxidative addition," *J. Phys. Chem.*, vol. 100, pp. 19 357–19 363, 1996.

[163] M. Svensson, S. Humbel, and K. Morokuma, "Energetics using the single point imomo (integrated molecular orbital + molecular orbital) calculations: Choices of computational levels and model system," *J. Chem. Phys.*, vol. 105, pp. 3654–3661, 1996.

[164] S. Dapprich, I. Komaromi, K. S. Byun, K. Morokuma, and M. J. Frisch, "A new implementation in gaussian98. part1. the calculation of energies, gradients, vibrational frequencies, and electric field derivatives," *J. Mol. Struct. (Theochem)*, vol. 462, pp. 1–21, 1999.

[165] T. Vreven and K. Morokuma, "On the application of the imomo (integrated molecular orbital + molecular orbital) method," *J. Comp. Chem.*, vol. 21, pp. 1419–1432, 2000.

[166] A. K. Rappe, C. J. Casewit, K. S. Colwell, W. A. Goddard, and W. M. Skiff, "Uff, a full periodic table force field for molecular mechanics and molecular dynamics simulations," *Journal of the American Chemical Society*, vol. 114, no. 25, pp. 10 024–10 035, 1992. [Online]. Available: dx.doi.org/10.1021/ja00051a040

[167] R. Krishnan, J. S. Binkley, R. Seeger, and J. A. Pople, "Self-consistent molecular orbital methods. xx. a basis set for correlated wave functions," *J. Chem. Phys.*, vol. 72, pp. 650–654, 1980.

[168] M. J. Frisch, J. A. Pople, and J. S. Binkley, "Self-consistent molecular orbital methods 25. supplementary functions for gaussian basis sets," *Journal of Chemical Physics*, vol. 80, no. 7, pp. 3265–3269, 1984.

[169] J. S. Binkley, J. A. Pople, and W. J. Hehre, "Self-consistent molecular orbital methods. 21. small split-valence basis sets for first-row elements," *J. Am. Chem. Soc.*, vol. 102, pp. 939–947, 1980.

[170] D. Porezag, T. Frauenheim, T. Köhler, G. Seifert, and R. Kaschner, "Construction of tight-binding-like potentials on the basis of density-functional theory: Application to carbon," *Phys. Rev. B*, vol. 51, no. 19, pp. 12 947–12 957, 1995.

[171] The overlap matrix elements $S^{CC}_{pp\sigma}$ and $S^{CC}_{pp\pi}$ are interchanged in both Fig. 1 and Table 1 of Ref. [72].

[172] I. V. Fisher, K. Daie, Y. Terazono, C. Herrero, F. Fungo, L. Otero, E. Durantini, J. J. Silber, L. Sereno, D. Gust, T. A. Moore, A. L. Moore, and S. M. Lindsay, "Conductance of a biomolecular wire," *PNAS*, vol. 103, no. 23, pp. 8686–8690, 2006.

[173] J. He, F. Chen, J. Li, O. F. Sankey, Y. Terazono, C. Herrero, D. Gust, T. A. Moore, A. L. Moore, and S. M. Lindsay, "Electronic decay constant of carotenoid polyenes from single-molecule measurements," *J. Am. Chem. Soc.*, vol. 127, pp. 1384–85, 2005.

[174] Conductance is proportional to transmission which is proportional to the magnitude of the wavefunction squared, i.e. $e^{-2\kappa x}$ for an evanescant wavefunction with imaginary wavevector κ.

[175] B. Q. Xu, X. L. Li, X. Y. Xiao, H. Sakaguchi, and N. J. Tao, "Electromechanical and conductance switching properties of single oligothiophene molecules," *Nano Lett.*, vol. 5, no. 7, pp. 1419–1495, 2005.

[176] J. K. Tomfohr and O. F. Sankey, "Complex band structure, decay lengths, and fermi level alignment in simple molecular electronic systems," *Phys. Rev. B*, vol. 65, no. 24, p. 245105, 2002.

[177] J. Li, J. K. Tomfohr, and O. F. Sankey, "Theoretical study of carotene as a molecular wire," *Physica E*, vol. 19, pp. 133 – 138, 2003.

[178] A. C. Whalley, M. L. Steigerwald, X. Guo, and C. Nuckolls, "Reversible switching in molecular elctronic devices," *J. Am. Chem. Soc. Communications*, vol. 129, pp. 12 590–12 591, 2007.

[179] X. Guo, A. C. Whalley, J. E. Klare, L. Huang, S. O'Brien, M. L. Steigerwald, , and C. Nuckolls, "Single-molecule devices as scaffolding for multicomponent nanostructure assembly," *Nano Lett.*, vol. 7, pp. 1119–1122, 2007.

[180] Z. Qian, S. Hou, J. Ning, R. Li, Z. Shen, X. Zhao, and Z. Xu, "First-principles calculation on the conductance of a single 1,4-diisocyanatobenzene molecule with single-walled carbon nanotubes as the electrodes," *J. Chem. Phys.*, vol. 126, p. 084705, 2007. [Online]. Available: dx.doi.org/10.1063/1.2483760

[181] S. H. Ke, H. U. Baranger, and W. Yang, "Contact transparency of nanotube-molecule-nanotube junctions," *Phys. Rev. Lett.*, vol. 99, p. 146802, 2007.

[182] T. B. Martins, A. Fazzio, and A. J. R. da Silva, "Organic molecule assembled between carbon nanotubes: A highly efficient switch device," *Phys. Rev. B*, vol. 79, p. 115413, 2009.

[183] S. Y. Quek, L. Venkataraman, H. J. Choi, S. G. Louie, M. S. Hybertsen, and J. B. Neaton, "Amine-gold linked single-molecule circuits: Experiment and theory," *Nano Lett.*, vol. 7, pp. 3477–3482, 2007.

[184] H. J. Choi, M. L. Cohen, and S. G. Louie, "First-principles scattering-state approach for nonlinear electrical transport in nanostructures," *Phys. Rev. B*, vol. 76, p. 155420, 2007.

[185] J. B. Neaton, M. S. Hybertsen, and S. G. Louie, "Renormalization of molecular electronic levels at metal-molecule interfaces," *Phys. Rev. Lett.*, vol. 97, p. 216405, 2006.

[186] U. Salzner, J. B. Lagowski, P. G. Pickup, and R. A. Poirier, "Design of low band gap polymers employing density functional theory: Hybrid functionals ameliorate band gap problem," *J. Comp. Chem.*, vol. 18, pp. 1943–1953, 1997.

[187] C. G. Zhan, J. A. Nichols, and D. A. Dixon, "Ionization potential, electron affinity, electronegativity, hardness, and electron excitation energy: Molecular properties from density functional theory orbital energies," *J. Phys. Chem. A*, vol. 107, pp. 4184–4195, 2003.

[188] G. Zhang and C. B. Musgrave, "Comparison of DFT methods for molecular orbital eigenvalue calculations," *J. Phys. Chem. A*, vol. 111, pp. 1554–1561, 2007.

[189] J. Li, G. Speyer, and O. F. Sankey, “Conduction switching of photochromic molecules,” *Phys. Rev. Lett.*, vol. 93, p. 248302, 2004.

[190] M. Koentopp, C. Chang, K. Burke, and R. Car, “Density functional calculations of nanoscale conductance,” *J. Phys. Condens. Matter*, vol. 20, p. 083203, 2008.

[191] C. Toher and S. Sanvito, “Efficient atomic self-interaction correction scheme for nonequilibrium quantum transport,” *Phys. Rev. Lett.*, vol. 99, p. 056801, 2007.

[192] J. Olrich, D. Esrail, W. Pontius, L. Venkataraman, D. Millar, and L. H. Doerrer, “Variability of conductance in molecular junction,” *J. Phys. Chem. B*, vol. 110, pp. 2462–2466, 2006.

[193] S. Ramo, J. R. Whinnery, and T. V. Duzer, *Fields and Waves in Communication Electronics*, 3rd ed. New York: John Wiley and Sons, Inc., 1993.

[194] S.G. Lias, ”Ionization Energy Evaluation” in NIST Chemistry WebBook, NIST Standard Reference Database Number 69, Eds. P.J. Linstrom and W.G. Mallard, National Institute of Standards and Technology, Gaithersburg MD, 20899, http://webbook.nist.gov (retrieved February 25, 2009).

[195] C. Desfrançois, V. Périquet, S. A. Lyapustina, T. P. Lippa, D. W. Robinson, K. H. Bowen, H. Nonaka, and R. N. Compton, “Electron binding to valence and multipole states of molecules: Nitrobenzene, para- and meta-dinitrobenzenes,” *J. Phys. Chem.*, vol. 111, pp. 4569–4576, 1999.

[196] J. P. Perdew, K. Burke, and M. Ernzerhof, “Generalized Gradient Approximation Made Simple,” *Phys. Rev. Lett.*, vol. 77, pp. 3865–3868, 1996.

[197] K. Raghavachari, J. S. Binkley, R. Seeger, and J. A. Pople, “Self-consistent molecular orbital methods. XX. A basis set for correlated wave functions,” *J. Chem. Phys.*, vol. 72, pp. 650–654, 1980.

[198] T. Clark, J. Chandrasekhar, G. Spitznagel, and P. von R. Schleyer, “Efficient diffuse function-augmented basis sets for anion calculations. III. The 3-21+G basis set for first-row elements, Li–F,” *J. Comp. Chem.*, vol. 4, pp. 294–301, 1983.

[199] M. J. Frisch, J. A. Pople, and J. S. Binkley, “Self-consistent molecular orbital methods 25. Supplementary functions for Gaussian basis sets,” *J. Chem. Phys.*, vol. 80, pp. 3265–3269, 1984.

[200] M. Ernzerhof and G. E. Scuseria, “Assessment of the Perdew-Burke-Ernzerhof exchange-correlation functional,” *J. Chem. Phys.*, vol. 110, pp. 5029–5036, 1999.

[201] J. C. Rienstra-Kiracofe, G. S. Tschumper, H. F. Scaefer, S. Nandi, and G. B. Ellison, “Atomic and molecular electron affinities: Photoelectron experiments and theoretical computations,” *Chem. Rev.*, vol. 102, pp. 231–282, 2002.

[202] F. Jensen, “Polarization consistent basis sets. III. The importance of diffuse functions,” *J. Chem. Phys.*, vol. 117, pp. 9234–9240, 2002.

[203] D. M. A. Vera and A. B. Peirini, “Species with negative electron affinity and standard DFT methods,” *Phys. Chem. Chem. Phys.*, vol. 6, pp. 2899–2903, 2004.

[204] A. A. Jarecki and E. R. Davidson, “Density functional theory calculations for F^-,” *Chem. Phys. Lett.*, vol. 300, pp. 44–52, 1999.

[205] W. J. Hehre, R. Ditchfield, and J. A. Pople, “Self-consistent molecular orbital methods. XII. Further extensions of Gaussian-type basis sets for use in molecular orbital studies of organic molecules,” *J. Chem. Phys.*, vol. 56, pp. 2257–2261, 1972.

[206] P. C. Hariharan and J. A. Pople, “The influence of polarization functions on molecular orbital hydrogenation energies,” *Theor. Chim. Acta*, vol. 28, pp. 213–222, 1973.

[207] A. Hirsch, “Functionalization of single-walled carbon nanotubes,” *Angew. Chem. Int. Ed.*, vol. 41, no. 11, pp. 1853 – 1859, 2002.

[208] A. H. Flood, J. F. Stoddart, D. W. Steuerman, and J. R. Heath, “Whence molecular electronics?” *Science*, vol. 306, pp. 2055–2056, 2004.

[209] J. Chen and M. A. Reed, “Electronic transport of molecular systems,” *Chem. Phys.*, vol. 281, no. 2-3, pp. 127–145, 2002.

[210] S. Suzuki, C. Bower, Y. Watanabe, and O. Zhou, “Work functions and valence band states of pristine and cs-intercalated single-walled carbon nanotube bundles,” *App. Phys. Lett.*, vol. 76, no. 26, pp. 4007–9, 2000.

[211] D. Lovall, M. Buss, E. Graugnard, R. P. Andres, and R. Reifenberger, “Electron emission and structural characterization of a rope of single-walled carbon nanotubes,” *Phys. Rev. B*, vol. 61, no. 8, pp. 5683–91, 2000.

[212] M. Shiraishi and M. Ata, “Work function of carbon nanotubes,” *Carbon*, vol. 39, pp. 1913–17, 2001.

[213] R. Gao, Z. Pan, and Z. L. Wang, “Work function at the tips of multiwalled carbon nanotubes,” *Appl. Phys. Lett.*, vol. 78, no. 12, pp. 1757–59, 2001.

[214] S. Suzuki, Y. Watanabe, Y. Homma, S. Fukuba, A. Locatelli, and S. Heun, "Photoemission electron microscopy of individual single-walled carbon nanotubes," *J. Electron Spectroscopy*, vol. 144-147, pp. 357–60, 2005.

[215] P. Liu, Q. Sun, F. Zhu, K. Liu, K. Jiang, Q. Li, and S. Fan, "Measuring the work function of carbon nanotubes with thermionic methods," *Nano Letters*, vol. 8, no. 2, pp. 647–51, 2008.

[216] V. Eyert, "A comparative study on methods for convergence acceleration of iterative vector sequences," *J. Comp. Phys.*, vol. 124, no. 0059, pp. 271–285, 1996.

Appendix A

NEGF

A.1 Overview

The NEGF subroutines added to Fireball (FB) are consolidated in the */progs/NEGF* subdirectory. These routines are initiated within the main *fireball.f90* program. New input and options files are required in the FB working directory to use NEGF features. To calculate transport, follow the steps described in Chapter 2: (1. relaxation, 2. generate contact matrix elements, 3. generate device matrices, 4. run eq. transport or NEGF-FB SCF calculation). Most NEGF options follow the same convention as FB where 0 means "off" and 1 means "on.". Guidelines for using NEGF input files are discussed in the following sections.

A.2 Input files

A.3 Basis file

Before calculating transmission, the matrix elements for the contacts and device must be referenced correctly using the parameter options part of *contact.optional* and *device.optional*. The number of atomic layers and atoms per layer for each contact is specified in the *contact.optional* file. The source and drain bulk poritions must each have **TWO** contact block layers (i.e. unit cells) listed in sequential order by each atomic layer along the direction of transport. The numbering order is set by the atom sequence listed in the *XXX.bas* file. The same ordering setup for the contacts must match the contact regions part of the device structure (contact-device-contact). The supercell device section does not need to be sequenced since it can be treated as one block layer. For example a zigzag (10,0) CNT has 4 layers and 10 atoms per layer. In the basis file, the atoms must be arranged such that the first 10 atoms are in the first layer, the second 10 atoms are in the second layer and so forth. Since one unit cell is 4 atomic layers, at least 8 atomic layers must be sequenced for both the source and drain. To verify that the atoms are sequenced this way use an atom visualizer program such as VMD or Webviewer. This ordering process must be set for extending the contacts in a RGF calculation.

A.4 Working Directories

Include the following directories in your FB work directory:

NEGFdata: This folder contains the matrix elements for the NEGF calculation. Depending on the amount of memory available, the calculation uses this storage space as the default saving location for all matrix element data. The folder contains the device, contact block layers, source and drain matrices for all NEGF calculations.

NEGF_MATS: This folder contains the Hamiltonian and Overlap matrix elements for a optimized supercell block. This data can be generated post-process given a fixed (ifixcharge = 1) and a converged charge density (CHARGES).

NEGF_OUTPUT: This folder contains all the output files that are created during a NEGF calculation. Subfolders are created for each current-voltage (I-V) step specified. These files include the transmission spectra, charge density at each self-consistent field (SCF) step, Qin/Qout potential profiles, spectral wavefunction data, basis file for rainbow blob, conductance data, and I-V data.

A.5 negf.optional

The *negf.optional* input file contains several options regarding the energy window, contour and other parameters for the transport calculation. Below lists in order each parameter and a description.

A.5.1 Example of file negf.optional

jobname *string to label job (less than 20 characters)*

1 *inegf*

3 *ipost (0=FB-SCF,1=NEGF-nonSCF,2=Restart NEGF-nonSCF, 3=FB/NEGF-SCF)*

0 *iwrtnegf*

1 *te_flag*

1 *spec_flag*

3000 *matrix size cutoff*

300 *initial # energy pts.*

-7.5 *starting energy (eV)*

0.01 ΔE *(eV)*

0.01 *max. percentage diff. cutoff, (adaptive E)*

1e-12 *min. T(E) cutoff, (adaptive E)*

1e-9 *min.* ΔE *(eV), (adaptive E)*

25 *# semicircle points (SCF)*

0 *# of poles at* E_F*, (SCF)*

15 *#KT from* E_F*, (SCF)*

1.0 *max* η *of semicircle (eV), (SCF)*

10 *# energy pts. between* $E_F \pm KT$ *(SCF)*

-30 *lowest eigen energy for contour (eV) (SCF)*

15.0 *highest eigen energy of contour (eV)*

0 *retain RGF block matrix data in memory*

jobname

Specifies the job name for NEGF. String is used for labeling output files in your work directory.

inegf

Toggles the NEGF calculation on/off in FB.

ipost

- 0 = FB SCF only, no NEGF

- 1 = NEGF (nonSCF), post-processor
- 2 = NEGF (nonSCF), restart post-processor from saved NEGF_DATA
- 3 = NEGF-FB SCF

iwrtnegf

The numbering order is set by the atom sequence listed in the *XXX.bas* file

- 0 = no matrix writeout
- 1 = matrix writeout using convereged CHARGES
- 2 = extend first/last block layer contacts.

(iwrtnegf =1): Set ifixcharges = 1 *options.input* and ipost = 0 to generate matrix elements for device for post-process NEGF calculations (i.e. ipost = 1, ipost = 2)). Must use converged charge density.
(iwrtnegf = 2): To extend contacts set inegf = 1, specify number of block layers to add in *contact.optional*

te_flag

Toggles write out the transmission after each SCF step.

spec_flag

Toggles write out the spectral function.

matrix size cutoff

Specifies maximum matrix dimension (M) required to use parallel matrix multiplication and inversion.

initial # energy pts.

Specifies initial number of energy points for a SCF calculation ($E_F \pm KT$) or transmission calculation after convergence.

starting energy

Specifies starting energy for a transmission calculation (after converged SCF calc.)

ΔE **(eV)**

Specifies initial energy grid spacing.

max. percentage diff. cutoff, (adaptive E)

Specifies cutoff criteria for the adaptive energy grid (typical value = 0.02 or 2%)

min. T(E) cutoff, (adaptive E)

Specifies transmission cutoff criteria. Any transmission below value is ignored during the adaptive grid search.

min. ΔE (eV), (adaptive E)

Specifies minimum energy spaced used in the adaptive energy grid search.

 # semicircle points (SCF)

Specifies number of semicircle points used in the complex contour integration when performing a NEGF-FB SCF calculation.

# of poles at E_F, (SCF)

Specifies number of E_F poles to include in the complex contour calculation (NOTE: this feature is NOT implemented)

 # KT from E_F, (SCF)

Specifies number of KT $\pm E_F$ in the tail portion of the complex contour.

max η of semicircle (eV), (SCF)

Specifies maximum imaginary potential (top of semicircle) of the complex contour.

 # E pts between $E_F \pm KT$

Specifies number of points taken in the tail region of the complex contour.

lowest eigen energy for contour (eV)

Specifies tail end, lowest energy to include in the complex contour.

highest eigen energy of contour (eV)

Specifies highest eigen energy of the system.

retain RGF block matrix data in memory

Toggle turns on subroutines which retain RGF matrix data in main memory (if available). Default configuration writes data to disk under *NEGFdata*.

A.6 contact.optional

The *contact.optional* input file contains several options including the atoms which serve as contacts, parameters for the surface green function calculation and the boundaries for the potential profile. Below lists in order each parameter and a description.

A.6.1 Example of file contact.optional

1 *first atom of source contact*

1120 *last atom of source contact*

1121 *source to device interface atom*

4 *# of atomic layers, source contact*

14 *# of atoms/layer, source contact*

1481 *first atom of drain contact*

2720 *last atom of drain contact*

1480 *drain to device interface atom*

4 *# of atomic layers, drain contact*

14 *# of atoms/layer, drain contact*

5.0368 *lattice constant for one contact block (Å)*

21 *number of contact blocks on source (drain)*

1e-10 *surface green function cutoff criteria*

1e-2 η*, used in* g_s *calc. over band gap (eV)*

1e-2 η*, used in* g_s *calc. over valence(conduction) regions (eV)*

1 *file format for contacts*

-5.533 E_F *(eV) of source contact*

-5.533 E_F *(eV) of drain contact*

1000 *HOMO level for source contact (eV) (for metal contact use > 100 eV)*

1000 *LUMO level for source contact (eV) (for metal contact use > 100 eV)*

1000 *HOMO level for drain contact (eV) (for metal contact use > 100 eV)*

1000 *LUMO level for drain contact (eV) (for metal contact use > 100 eV)*

CNT_77_GGA_SZ_L_LC *source contact index name*

CNT_77_GGA_SZ_R_RC *drain contact index name*

CNT_77_GGA_SZ_LC *source contact type*

CNT_77_GGA_SZ_RC *drain contact type*

1st atom source contact

Specifies first atom of the source contact (normally one).

last atom of source contact

Specifies last atom of the source contact.

source to device interface atom

Specifies atom which bridges the source contact to the device region. Defines source boundary condition for gate bias.

# of atomic layers, source contact

Specifies number of atomic layers in the source contact.

# of atoms/layer, source contact

Specifies number of atoms per atomic layer in the source contact.

first atom of drain contact

Specifies first atom in the drain contact.

last atom of drain contact

Specifies last atom in the drain contact.

drain to device interface atom

Specifies atom which bridges the drain contact to the device region. Defines drain boundary condition for gate bias.

# of atomic layers, drain contact

Specifies number of atomic layers in the drain contact.

# of atoms/layer, drain contact

Specifies number of atoms per layer in the drain contact.

lattice constant for one contact block ($\mathring{A}$)

Specifies lattice vector constant (direction of transport) for both contacts.

number of contact blocks on source (drain)

Specifies number of repeating block layers in the source (drain) contact regions that extend from a given supercell block.

surface green function cutoff criteria

Specifies cutoff criteria for decimation approach when calculating surface green function g_s

η g_s **calc. in band gap (eV)**

Specifies imaginary potential used in surface green function calculation within bandgap energies of contacts.

η g_s **calc. in valence(conduction) regions (eV)**

Specifies imaginary potential used in surface green function calculation within valence and conduction band energies of contacts.

file format

Specifies file format for contact matrix data (0=ASCII and 1=Binary)

E_F **(eV) of source contact**

Specifies E_F for source contact.

E_F **(eV) of drain contact**

Specifies E_F for drain contact.

HOMO for source contact (eV) (for metal contact use $>$ 100 eV)

Specifies valence band edge (HOMO) for source contact. If contact is metallic use a value above 100 eV.

LUMO for source contact (eV) (for metal contact use $>$ 100 eV)

Specifies conduction band edge (LUMO) for source contact. If contact is metallic use value above 100 eV.

HOMO for drain contact (eV) (for metal contact use $>$ 100 eV)

Specifies valence band edge (HOMO) for drain contact. If contact is metallic use value above 100 eV.

LUMO for drain contact (eV) (for metal contact use $>$ 100 eV)

Specifies conduction band edge (LUMO) for drain contact. If contact is metallic use value above 100 eV.

source contact index name

String which specifies source contact index name.

drain contact index name

String which specifies drain contact index name.

source contact type

String which specifies source contact type.

drain contact type

String which specifies drain contact type.

A.7 device.optional

The *device.optional* input file contains several parameters for the device and the atoms which define the device supercell.

A.7.1 Example of file device.optional

5 *device type*

1 *# of layers*

368 *# of atoms per layer*

-6.37 E_F *of device (eV)*

1177 *first atom of device supercell*

1544 *last atom of device supercell*

1 *file format*

1 *direction of transport 1=x, 2=y, 3=z*

cnt77_col1 *device label*

device type

This value specifies the type of device:

- 1 = linear chain (not implemented, used only for testing)
- 2 = periodic atomic layered relaxed system (usually bulk contact: CNT, NW, Gold)
- 3 = non-periodic (clustered) relaxed system (i.e. contact-device-contact))
- 4 = periodic system (i.e. contact-device-contact) relaxed supercell

- 5 = periodic extended contacts + supercell block (i.e. nm length contact-device-contact)

# of layers

Specifies number of layers in device. Normally 1 for supercells. Use > 1 for contact bulk material (device type = 2).

# of atoms per layer

Specifies the number of atoms per atom layer. Normally total # of atoms in supercell (device type = 3-5). Less than total for contact bulk material (device type = 2).

E_F of device (eV)

Fermi energy of system. Obtain value from converged FB SCF calculation for post NEGF process. Fix value to bulk contact E_F for NEGF-FB SCF calculations (device type = 4 or 5).

first atom of device supercell

Specifies first atom of the device region.

last atom of device supercell

Specifies last atom of the device region.

file format

Specifies file format for the device matrix data (0=ASCII and 1=Binary).

direction of transport 1=x, 2=y, 3=z

Specifies transport direction through device.

device label

Specifies device label (less than 20 characters).

A.8 iv.optional

The *iv.optional* input file contains several options for the current-voltage calculation of a device.

A.8.1 Example of file iv.optional

1 *iv toggle*

0.1 *initial* V_{ds} *voltage potential (eV)*

1.5 *final* V_{ds} *voltage potential (eV)*

15 *#* *of* V_{ds} *pts.*

2.0 *rigid shift of eigen energies device region (eV)*

0.0 *initial* V_g *voltage potential (eV)*

1.0 *final* V_g *voltage potential (eV)*

10 *#* *of* V_g *pts.*

0.5 *% offset of source potential*

0.5 *% offset of drain potential*

1 *potential type*

0 *image potential*

iv toggle

Toggles current-voltage calculation (0 = off, 1 = on)

initial V_{ds} voltage potential (eV)

Specifies initial drain-source voltage potential drop.

final V_{ds} voltage potential (eV)

Specifies last drain-source voltage potential drop.

# of V_{ds} pts.

Specifies number of drain-source voltage potential points.

rigid shift of eigen energies device region (eV)

Specifies rigid shift of molecular device levels (used to correct molecular positions) (eV).

initial V_g voltage potential (eV)

Specifies initial gate voltage potential drop.

final V_g voltage potential (eV)

Specifies final gate voltage potential drop.

# of V_g pts.

Specifies number of gate voltage potential points.

% offset of source potential

Specifies percentage offset from E_F of source contact.

% offset of drain potential

Specifies percentage offset from E_F of drain contact.

potential type

Specifies potential type (0 = rigid shift, 1=linear drop)(This feature is not implemented).

image potential

Specifies an image potential calculation between contacts. (special use)

Appendix B

Rainbow Blob

Rainbow blob, otherwise known as alfalfa, uses orbital Mulliken charges or spectral weights of every atom to plot the HOMO and LUMO orbitals from FIREBALL or the covariant spectral function from NEGF. The input file for alfalfa, *populations.dat*, is written out from FIREBALL and NEGF.

B.1 Preparing

Before running the visualizer, the HOMO and LUMO energy state must be determined. Within the output FIREBALL log file, the *ztot* value divided by two gives the HOMO energy level. The *ztot* value is typically listed toward the bottom of the log file after a FB SCF loop is complete. If the material has an indirect band structure, run the appropriate k-points. Copy the *populations.dat* file to the visualizer working directory.

B.2 Basis File

The *XXX.bas* file must first be converted before running the visualizer script *cej-alfa.com*. Copy the *XXX.bas* file used in FIREBALL or NEGF, to the visualizer directory and open *convertbas.com*. Edit *convertbas.com* by changing the *XXX.bas* file name listed above *3dpix.bas* using the name of the basis file used in FIREBALL. Execute the script and copy, NOT rename, the *3dpix.bas* file as *EXAMPLE.bas*. The *3dpix.bas* file and *EXAMPLE.bas* file must be identical.

B.3 cej-alfa.com

HOMO-LUMO plot

Edit the *cej-alfa.com* bash script as follows:
cat.... (Do not edit this command)
174 (Change this value to the total number of atoms in the *XXX.bas* file.)
500 (Edit this value to the total number of energy bands, found in populations.dat)
350 (Edit this value to correspond to the energy band of interest (HOMO/LUMO)
XXX.bas (Change this filename to the one used in *convertbas.com*
.... (Leave the remaining lines the same)
....
After editing, execute the script. A visualizer window will appear and use the 10 number key pad for rotating the structure. Don't use number 5, it will place your current view in the middle of the structure.

DOS plot

Copy the *populations_NEGF.dat* and *energy.dat* files to visualizer working directory. Rename the *populations_NEGF.dat* file as *populations.dat* before running the script. Edit the *cej-alfa.com* bash script as follows:

cat... (Do not edit this command)

174 (Change this value to the total number of atoms in the *XXX.bas* file.)

500 (Edit this value to the total number of energies used, found in energy.dat)

350 (Edit this value to a specific energy reference number. This number must correspond to the reference numbers listed in *energy.dat*, not the actual energy value.

XXX.bas (Change this filename to the one used in *convertbas.com*

.... (Leave remaining lines the same)

....

After editing, execute the script. A visualizer window will appear and use the 10 number key pad for rotating the structure. Don't use number 5, it will place your current view in the middle of the structure.

B.4 Capturing Plot

To save the plot *xv* must be used. Simply use the *xv* program to capture the images.

Appendix C

Beowulf Clusters

Supremo and Mocha, the LAboratory for Terascale and Terahertz Electronics (LATTE) Linux Beowulf clusters served as the primary computing facilities for this dissertation project (see Fig. C.1). The master and slave nodes for both systems were assembled and configured by Nicolas Bruque using parts from the following vendors: PC Club of Riverside-CA, KomUSA of Walnut-CA and ServersDirect of Industry-CA. Thomas Helander took over primary administrative duties during the summer of 2007.

A digital temperature PCB board was designed and built during the spring of 2006 which monitors climate conditions in the cluster room. The system is set to shutdown in the event the temperature reaches 95 degree F. The temperature script also notifies the EE system administrator, Nick Bruque, Thomas Helander, and Roger Lake via email and cell phone text messaging when the room temperature reaches 85 degrees.

supremo.engr.ucr.edu

mocha.engr.ucr.edu

Figure C.1: LATTE's Beowulf Clusters (June 2009).

C.1 Supremo

Supremo was assembled and configured during the summer of 2004. This cluster served primarily as LATTE's core computing facility for all computational tasks up to 2007. Initially the system comprised of the master node and eight slave nodes but by May 2005 the system had expanded to 32 nodes. The master node is equipped with a 32-bit Intel entry server motherboard S875WP1-E, a 3Ghz Intel Pentium 4 (Prescott - 90nm), 4GB ECC PC3200/DDR RAM, two 80GB UltraATA hard drives (RAID1), four 73GB Ultra320 SCSI hard drives (RAID0), an Adpatec 29320A-R SCSI U320 RAID PCI-adapter and one ATI9800 video graphics card. Each slave node is essentially a high end 32-bit performance workstation comprised of an Intel D875PBZ motherboard (i875 chipset), a 3GHz Intel Pentium 4 (Prescott - 90nm) processor, 2GB of ECC PC3200/DDR RAM (unbuffered), one 80GB SATA hard drive, and an ATI9200 video graphics card. The cluster is networked together via gigabit switches.

C.2 Mocha - AMD 64-bit Cluster

Mocha, the second Beowulf cluster, was built using the AMD 64-bit Athlon architecture during the winter quarter of 2007. The master node features two 2GHz Opteron processors with 16GB of ECC RAM. Sixteen slave nodes are equipped with 4GB of RAM, each with a 2GHz dual core AMD Athlon processor. The Mocha cluster also included a 2TB data storage server known as lattelocker, which serves as LATTE users shared home storage. The fileserver is configured via RAID5 (one hot swappable drive) with a triple redundant data backup (RAID 10) and an APC backup battery for power failures.